Title

Estimating Post-Fire Flood Hazards: Model Formulation, Parameterization, and Applications

Permalink

https://escholarship.org/uc/item/5dp5g2bx

Author

Jong-Levinger, Ariane

Publication Date

2023

UNIVERSITY OF CALIFORNIA,
IRVINE

Estimating Post-Fire Flood Hazards: Model Formulation, Parameterization, and Applications

DISSERTATION

submitted in partial satisfaction of the requirements
for the degree of

DOCTOR OF PHILOSOPHY

in Civil and Environmental Engineering

by

Ariane Jong-Levinger

Dissertation Committee:
Professor Brett F. Sanders, Chair
Associate Professor Tirtha Banerjee
Professor Douglas Houston

2023

TABLE OF CONTENTS

LIST OF FIGURES

Page

LIST OF TABLES

ACKNOWLEDGMENTS

I would like to thank my advisor, Professor Brett Sanders, for his mentorship and encouragement since the day I started my graduate program at UCI in 2018. He has taught me so many important lessons and through his mentorship throughout my Ph.D. program, he has helped me realize the amazing things I am capable of; for that I will always be grateful. I would also like to thank my committee members, Professor Doug Houston and Professor Tirtha Banerjee, for taking the time to provide thoughtful feedback on my work. Thank you for serving on my committees for my Preliminary and Qualifying Exams and for your continuous support throughout my graduate program.

Thank you to Riverside County Flood Control and Water Conservation District for being a wonderful partner on this research; your feedback, flood management expertise, and willingness to share data has been integral to the development of the modeling framework. I want to express my gratitude to Jason Uhley, who supported this research by attending multiple meetings with our research team and providing us with the District's support. I would like to give special thanks to Joshua Tremba, who has personally provided me with much of the data provided from Riverside County that was included in this work, and has cheerfully and proactively helped this research move forward in any way that he can.

Thank you to Jo Schubert, Daniel Kahl, and Matthew Brand for being great teammates and making our work as part of the Flood Lab at UCI so enjoyable. Thank you to my colleagues and friends in the CEE Department and at ISEB who have laughed, commiserated, and had long conversations about the future directions of our world with me. Special thanks to the members of CEEGA, CEER, and the Planteaters who have been my found family and community while at UCI.

Thank you to Professor Jason Keller for being my first research mentor. It can't be overstated what a profound impact your mentorship had on my decision to become a scientist, to earn my Ph.D., and to become teacher and mentor for future generations of scientists and engineers. Thank you to my high school biology teacher Valarie Sebastiano, who ignited the spark that started me down the path of pursuing a career that addressed climate change.

And finally, thank you to the family and friends who have always supported me on this journey and were there when I needed them most. Thank you to my mother, sister, and in-laws who have been a constant source of love, support, and encouragement. And thank you to my husband, who has been there for me no matter what and has been especially supportive during the final stretch of the Ph.D. I love you all so much and simply wouldn't have gotten this far without you.

This dissertation is based upon work supported by the National Science Foundation under Grant HDBE-2031535, the National Oceanic and Atmospheric Administration Effects of Sea Level Rise Program under Grant NA16NOS4780206, and the Ridge to Reef NSF Research Traineeship, award DGE-1735040. Many thanks to the Rose Hills Foundation for their three years of support of this work through the Science & Engineering Fellowship.

VITA

Ariane Jong-Levinger

EDUCATION

Doctor of Philosophy in Civil and Environmental Engineering **2023**
University of California, Irvine *Irvine, CA*

Master of Science in Civil and Environmental Engineering **2020**
University of California, Irvine *Irvine, CA*

Bachelor of Science in Environmental Science and Policy **2016**
Chapman University *Orange, CA*

RESEARCH EXPERIENCE

Graduate Student Researcher **2018–2023**
University of California, Irvine *Irvine, CA*

Staff Scientist **2016–2018**
Council for Watershed Health *Los Angeles, CA*

Data Analyst **2015–2016**
Southern CA Coastal Water Research Project *Costa Mesa, CA*

Undergraduate Student Researcher **2013-2014**
Chapman University *Orange, CA*

TEACHING EXPERIENCE

Teaching Assistant, ENGRCEE 170 **2019–2022**
University of California, Irvine *Irvine, CA*

Teaching Assistant, ENGRCEE 171 **2019–2020**
University of California, Irvine *Irvine, CA*

JOURNAL PUBLICATIONS

Jong-Levinger, A., Banerjee, T., Houston, D., & Sanders, B. F. (2022). Compound Post-Fire Flood Hazards Considering Infrastructure Sedimentation. *Earth's Future*, *10*(8), e2022EF002670. `https://doi.org/10.1029/2022EF002670`

Kahl, D. T., Schubert, J. E., **Jong-Levinger, A.**, & Sanders, B. F. (2022). Grid edge classification method to enhance levee resolution in dual-grid flood inundation models. *Advances in Water Resources*, 168, 104287.

El-Askary, H., Li, J., Li, W., Piechota, T., Ta, T., **Jong, A.**, Zhang, X., & Yang, T. (2018). Impacts of aerosols on the retreat of the Sierra Nevada Glaciers in California. *Aerosol and Air Quality Research*, 18(5), 1317-1330.

CONFERENCE PRESENTATIONS

Jong-Levinger, A., Sanders, B. F. (2022, December 12-16). Estimating compound post-fire flood hazards using a stochastic simulation framework [Poster Presentation]. AGU Fall Meeting 2022, Chicago, IL, United States.

Jong, A., Banerjee, T., Sanders, B. F. (2021, December 13-17). Modeling the under-protection of human development from post-fire floods and debris flows [Poster Presentation]. AGU Fall Meeting 2021, New Orleans, LA, United States.

Jong, A., Banerjee, T., Sanders, B. F. (2021, April 10). Modeling dynamic flood and debris flow risk at the intersection of the natural and built environment [Oral Presentation]. So Cal Fluids XIV, online.

Jong, A., Schubert J. E., Banerjee, T., Sanders, B. F. (2020, December 1-17). Integration of in-situ and remotely sensed data for post-fire flood risk modeling [Poster Presentation]. AGU Fall Meeting 2020, online.

HONORS AND AWARDS

Rose Hills Foundation Science & Engineering Fellowship **2020-2022**

University of California, Irvine

Ridge 2 Reef NSF Research Traineeship Fellowship **2021**

University of California, Irvine

Honorable Mention **2020**

National Science Foundation Graduate Research Fellowship

ABSTRACT OF THE DISSERTATION

Estimating Post-Fire Flood Hazards: Model Formulation, Parameterization, and Applications

By

Ariane Jong-Levinger

Doctor of Philosophy in Civil and Environmental Engineering

University of California, Irvine, 2023

Professor Brett F. Sanders, Chair

Human development situated at the foot of mountains faces sediment-laden flood hazards characterized by high-velocity, erosive flows carrying mud and debris. In the western United States, sediment-laden flood hazards are increasing due to more frequent and severe wildfires, more intense precipitation, and the expansion of development towards mountain wildlands. Considerable work has focused on developing models of post-fire peak flows and sediment yields at the outlet of mountain canyons, but the risk to communities downstream of protective flood infrastructure common throughout the southwestern U.S. is largely unknown. We present an original modeling framework that captures the interactions between wildfires, storms, and flood infrastructure to estimate sediment-laden flood hazards. Stochastic modeling with a continuous simulation approach is used to quantify uncertainty and explicitly consider antecedent conditions. This work shows that compound post-fire flood hazards may be up to 6 times larger than suggested by the marginal hazard posed by extreme precipitation, and that future increases in wildfire severity and intensity could increase flood hazards by up to a factor of 11. Furthermore, modeling of compound post-fire flood hazards across the Santa Ana Mountains in Riverside County, California reveals hot spots of risk below catchments that last burned over 45 years ago. As urban expansion into mountainous regions continues to increase around the world, an improved understanding of the hazards facing communities “protected” by infrastructure is important to better characterize the spatial distribution of risks across populations, increase risk awareness, and inform sustainable adaptation and resilient land development practices.

Chapter 1

Introduction

Around the world, a concentration of human development can be found at the foot of mountains, where communities contend with several types of natural hazards including wildfires, landslides, debris flows, mudflows, and flooding. In the western U.S., the combination of three trends–increasing wildfire frequency and severity (168; 28; 103), increasing precipitation volatility (144; 41; 147), and the expansion of development into mountain wildlands (15; 112)–is leading to the increased occurrence of deadly floods and mudslides (19). With steep channel and floodplain slopes and even steeper mountain hillslopes, rainfall generates fast-moving flows that readily entrain available sediment and build the capacity to transport large debris such as boulders and trees. These destructive flows can also carve new channels in unexpected ways, and as high velocity, sediment-laden flows encounter flatter topography, heavier solids settle out which reduces the capacity of flood channels (98; 127; 62). A recent example is given by the Pakistan floods of August 2022, which involved flows of rock and debris within near-mountain environments and extreme fluvial flooding across flatter togography (89).

The expression *ultrahazardous flooding* was introduced to describe the elevated danger of near-mountain alluvial fans (98), a specific type of geography found in near-mountain environments, but this term is equally relevant to a wide range of near-mountain geographies with steep slopes and fast-moving, sediment-laden flood hazards prone to unpredictable flow paths (127; 66). The expression *sediment-laden floods* has also been used in the context of near-mountain environments where flood hazards involve the entrainment of sediment and debris (39). Recently burned mountain canyons are especially prone to produce sediment-laden floods during post-fire storms, as runoff and erosion on burnt terrain have been observed to be 1-4 orders of magnitude greater than that on unburnt terrain in the European Mediterranean and more than 100 times greater on large-plot to hillslope scales in the southwestern United States (134; 174). These hydrogeomorphic changes result from the removal of vegetation cover by wildfire, which exposes soil to erosion via raindrop impact, and, in some cases, from the creation of a hydrophobic layer caused by heat-induced soil water repellency and/or the clogging of soil pores with ash (96; 57).

The geographical distribution of near-mountain, sediment-laden flood hazards is poorly understood compared to fluvial and coastal risks. The combined pluvial, fluvial, and coastal flood risks facing the U.S. have only recently been systematically estimated at regional (130) and national scales (6), supporting improved understanding of the exposed populations and inequities (145). Yet the unique and severe threat posed by ultrahazardous, sediment-laden floods has not been considered in these studies. Moreover, there is a growing recognition that a primary driver of increasing flood risks is the expansion of human development into high-hazard areas (3), which further motivates improved characterization of sediment-laden floods. Mountainside communities may or may not have formal flood infrastructure to defend against sediment-laden floods. In low- and middle-income countries, the periphery of urban areas often intersects mountainous topography and is characterized by informal development (2; 46). On the other hand, in more affluent countries such as the U.S., elevated topography often attracts formal development for highly affluent communities (37). Communities with the resources to build protective flood infrastructure tend to heavily rely on it, over time becoming less aware of their long-term flood risk due to the capacity of the infrastructure to prevent lower magnitude, more frequent floods. This so-called "levee effect" creates a false sense of safety that leaves communities relatively unaware of and underprepared for flood hazards and especially ultrahazardardous flooding, with its rapid onset and unique ability to clog infrastructure (169; 95).

Near-mountain, sediment-laden flood hazards are produced from the interaction of both natural and anthropogenic hazard drivers. Climate, hydrologic condition, and topography are the key natural drivers, while flood infrastructure design, maintenance, and location are important human factors that control the development, severity, and spatial distribution of the hazard. While considerable research has focused on predictive models of post-fire streamflow and erosion to improve the understanding of risks and the processes that generate them, only recently has attention been given to the role of infrastructure in shaping downstream hazards to development. Debris basins are designed to collect sediment, mud, and debris shed from mountain catchments and allow water and fine sediment to pass downstream into flood channels (127; 65; 64; 166; 110; 173); thus downstream communities are impacted by sediment-laden flooding when: (1) mud and debris overtop the debris basin and/or (2) downstream channels clog with sediment, lose capacity, and trigger overtopping of clear-water flows. For example, a storm that occurs early in the wet season may result in the filling of a debris basin, enabling flooding later in the storm season from even small storms. Consideration of event sequences is thus crucial to understanding ultrahazardous sediment-laden flooding as a compound hazard, or a natural hazard produced by the interaction of multiple hazard drivers (126). Moreover, the importance of event sequences motivates hazard estimation by continuous simulation, i.e., where physical processes are simulated over time (e.g., hourly, daily) with a hydrologic model, events are resolved by explicitly considering antecedent conditions, and the statistics of extremes (e.g., number of exceedances per century) are deduced from long records of model outputs (9; 104; 175).

The objective of this dissertation is to: (1) present a new stochastic continuous simulation model suited to the estimation of near-mountain, sediment-laden flood hazards where communities are served by debris basins and/or flood channels, (2) present a robust field application and validation of the model including a parameter estimation framework considering commonly available data (e.g., gage data and data products from remote sensing and other models) as well as model sensitivities and error propagation properties, and (3) examine the spatial distribution of near-mountain, sediment-laden flood hazards across watersheds with differing hydrological, flood infrastructure, and socio-economic characteristics. With expanding urbanization around the world into mountainous geographies, improved understanding of the hazards facing communities "protected" by infrastructure is important to improve understanding of the distribution of risks across populations, to increase risk awareness, and to inform needs for infrastructure adaptation and resilient land development practices.

1.1 Sediment-Laden Flood Hazard Modeling

A number of models have been developed to estimate plot- to catchment-scale runoff and erosion rates, the natural hazard drivers which contribute to sediment-laden floods. Catchment-scale post-fire runoff models typically estimate peak discharge at the catchment outlet; model types include empirical (e.g., 125; 52; 150), semi-empirical/semi-distributed such as HEC-HMS (148; 167), and physically based models (33; 156). Studies comparing empirical, semi-distributed, and process-based models of post-fire peak discharge have not provided clear evidence for a single approach that consistently performs well across multiple study sites (73; 23).

Post-fire erosion models often estimate sediment yields (sediment volume per contributing area), which are largely calculated using empirical methods derived from regression analysis (e.g., 176; 132; 119; 102; 39; 105; 164), though a smaller number of process-based models exist (33; 42; 74). Comparison studies of empirical and process-based post-fire erosion models have found that watershed-scale model estimates span three orders of magnitude and that current models tend to consistently identify areas of low and high potential, but need better calibration for improved accuracy (69; 120). Further, these studies present cases in which estimates from empirical models were better than those from processed-based models when compared to data from the region to which they were calibrated; this supports the conclusion that currently, no single modeling framework estimates post-fire erosion well across multiple regions.

Urban areas at risk of exposure to post-fire flood and debris hazards have been estimated in a number of ways for emergency preparedness measures such as risk communication to exposed populations, the placement of protective walls and barriers, and evacuation plans. Two-dimensional (2D) models for mud and debris flow hazards emerged in the 1980s with a water volume balance equation and momentum equations that account for the complex rheological behavior of non-Newtonian, hyperconcentrated flows including cohesive yield stresses, Mohr-Coulomb shear stress, viscous shear stress, turbulent shear stress, and dispersive shear stress (100). Application of 2D models requires a digital elevation model (DEM), Manning coefficient distribution, estimates of parameters for viscous and yield stresses, and a configuration of hazard drivers such as rainfall rates and/or streamflow rates from a mountain catchment. Furthermore, 2D models output spatio-temporal distributions of flood hazards (e.g., depth, velocity) needed for exposure assessment. The entrainment of sediment into flood flows increases volumetric flow rate, a process known as bulking (93; 92; 62), and acts to further magnify hazards. In practice, 2D hazard models have been applied under the assumption of a bulked flow rate defined by a bulking factor k, which represents the ratio of the volumetric flow rate of the fluid-debris mixture to the flow rate of the fluid alone, and can be linked to fire severity (48). Roughly speaking, a bulking factor of 1.00-1.25 corresponds to normal streamflow, a bulking factor of 1.25-1.67 corresponds to hyperconcentrated flow, and a bulking factor of 1.67-2.86 corresponds to mud or debris flows (48). These values follow definitions of debris flows as sediment-water mixtures with a sediment concentration of 50% or greater, and hyperconcentrated flows as mixtures with sediment concentrations of 20-40% (107; 48). 2D hazard models may assume a rigid bed (100; 83) or erodible bed (4; 124; 80; 90). In the case of erodible bed models, an entrainment formulation is adopted to account for mass transfer from the sediment bed into the fluidized layer, and thus the bulking process is resolved. While this eliminates the need for a bulking parameter, additional parameters are typically required to resolve sediment entrainment and/or transport processes (e.g., 26; 90, and others). Whether fixed or erodible bed modeling of debris flow hazards is preferable for a particular application will depend on the availability of data to parameterize models and tolerances for uncertainties and computational costs, as erodible bed models tend to have significantly higher computational costs than rigid bed models (88).

1.2 Design and Maintenance of Flood Infrastructure

Mitigation of post-fire flood hazards has mainly been approached with two types of infrastructure: debris basins, which capture eroded coarse sediment and debris at the outlet of mountain catchments, and flood channels, which are designed to convey mixtures of runoff and fine sediment past developed areas to downstream water bodies (132; 63). Johnson and McCuen (64) define a debris basin as "a structure designed to contain all or part of a single debris flow or multiple debris flows for the purpose of protecting homes, roads, and property downstream of a debris-generating area." Debris basins have been used in the western U.S., Japan, Europe, and Canada to mitigate hazards posed by sediment-laden flows, including debris flows (65; 64; 166; 110; 101; 173). In general, important debris basin design parameters for sizing debris basins include the frequency of the design flow event and the magnitude of the flow (64). In southern California, design practices vary regionally depending on local regulatory bodies, but generally call for the sizing of debris basins using a combination of probabilistic precipitation intensity data and empirical models of sediment yield that depend on watershed attributes such as slope, area, soil properties, and burn severity (48). Similarly, the sizing of flood channels is based on precipitation data and semi-empirical models of peak flood discharge (48).

Infrastructure is designed for a specific standard of performance defined by an annual return period, T, or an annual exceedance probability $p = 1/T$, and following guidelines established by county-level governments (48). For example, a channel designed to contain the 20-year return period flow event has an annual exceedance probability of 5%, or smaller if a safety factor is used. The exceedance probability of a flood channel, p_{c}, will not necessarily be the same as the exceedance probability of the precipitation used to size it, p_{p}, due to compounding factors that affect the likelihood of an overtopping event (i.e., when the flow rate through the channel exceeds its flow capacity). In particular, channels are designed using specific assumptions (models) about runoff and sediment loads produced by rainfall, and assuming regular maintenance to prevent loss of flow capacity. However, the frequency and intensity of precipitation and wildfires are affected by climate change (168; 28; 81; 144; 41), and sequences of storm events may lead to rapid sedimentation of debris basins and channels causing loss of channel capacity (48). The lack of regular maintenance of infrastructure (e.g., removal of sediment and debris) is also a growing problem based on resource constraints (155).

This dissertation presents a new, original model to estimate present and future compound, post-fire, near-mountain, sediment-laden flood hazards facing communities served by flood infrastructure of different types, including natural and built floodways. Specifically, we are interested in estimating the exceedance probability (and associated return period) of a flood channel (natural or engineered) downstream of a mountain catchment and debris basin vulnerable to clogging with sediment. Characterizing an exceedance probability is important for designing infrastructure to meet targeted levels of protection, quantifying the effect of maintenance on risks, and increasing risk awareness among communities and governments(95; 27; 54). Hence, this dissertation presents the Post-Fire Flood Hazard Model (PF2HazMo) to estimate the compound exceedance probability of debris basins and flood channels defending communities from harm. PF2HazMo is designed to simulate both present and future distributions of hazard estimates over multidecadal timescales to inform long-term flood risk management efforts under alternative climate or management scenarios. PF2HazMo is developed with a lumped model formulation and designed continuous simulation. Several key variables are treated as random variables, and thus a stochastic simulation approach is used and outputs (e.g., number of exceedances) are provided as probability distributions. Following application of PF2HazMo to estimate the probability of overtopping (and magnitude of bulked flows corresponding to specific exceedance probabilities), detailed 2D modeling can proceed to illuminate hazard levels on a street-by-street and parcel-by-parcel basis within impacted communities (85; 129). PF2HazMo is thus envisioned a framework for filling a major gap in our current understanding of flood risks and the chain of modeling needed to link climate-induced changes in wildfires and rainfall to changes in flood risks facing growing urban populations.

Chapter 2

PF2HazMo: Model Formulation

PF2HazMo is a stochastic continuous simulation model that is forced by a daily precipitation time series (e.g., from a Monte Carlo Markov Chain rainfall simulator) with the occurrence of fire and fire severity treated as random variables. A mass balance equation is solved for sediment to track the filling of the debris basin. Furthermore, the model tracks the capacity of flood channels over time based on the amount of channel deposition from debris basin overtopping, and predicts the occurrence of channel overtopping events (i.e., hazard to communities) by comparing flood peaks against channel capacity. Figure 2.1 illustrates a common progression of states that are captured during continuous simulation with PF2HazMo: The initial state is a healthy, vegetated watershed with infrastructure at full capacity (Fig. 2.1A). The second state (Fig. 2.1B) captures changes to watershed properties from wildfire, which contribute to heightened flows of runoff and sediment, and the accumulation of sediment in the debris basin. The third state (Fig. 2.1C) captures overtopping of the debris basin (with sediment) and/or the flood channel (with flood flows) from subsequent rainfall events. And the fourth state (Fig. 2.1D) captures the system following storm events or between storm events, when infrastructure capacity is restored with cleaning, and vegetation recovers over time. Finally, by using a stochastic modeling approach, thousands of different sequences are simulated over a long period of time (e.g., 100 years), and a probabilistic estimation of flood hazard levels is provided including the number of debris basin overtopping events per century and the number of channel overtopping events per century.

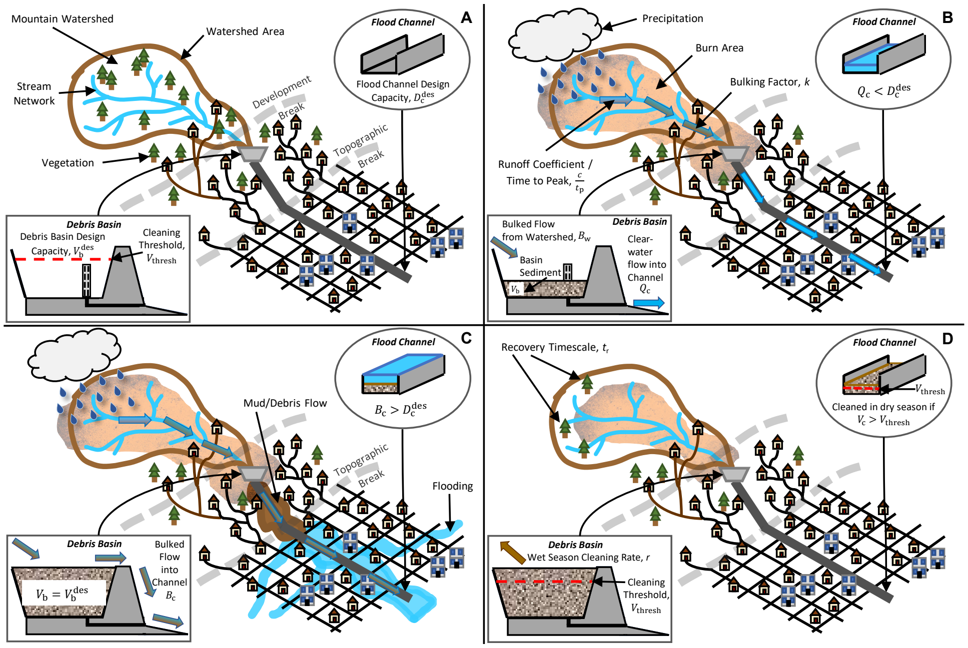

Figure 2.1: Progression of system states captured by Post-Fire Flood Hazard Model (PF2HazMo). (A) Pre-fire, clean infrastructure state, (B) Post-fire wet-weather state, (C) Post-fire wet-weather state with infrastruture overtopping, (D) Post-storm recovery state.

.

We apply Monte Carlo (MC) methods to simulate the compound hazard (75). MC methods provide a robust approach for characterizing the uncertainty inherent in estimates of compound hazards linked to the variability in the random variables that drive them–in this case, wildfire and precipitation. They can also be used to generalize complex models of physical systems into a set of basic events and interactions that is simpler, more computationally efficient, and more scalable than a model produced by analytic methods (75). Unlike deterministic approaches to modeling hydrologic processes, stochastic approaches like MC methods allow modelers to use a single record of precipitation or floods to forecast a range of statistically possible futures for a given watershed, enabling a much richer understanding of future hydrologic conditions and evaluation of flood infrastructure (162). Stochastic modeling approaches are preferable to deterministic ones when evaluating the implementation of different management alternatives because the former can determine whether a difference in outcomes between alternatives is significant in a statistical sense, while the latter can only provide a single estimate indicating whether the outcomes differ. Moreover, stochastic modeling is valuable for estimating the probability that a particular management or design alternative achieves a specific goal, which is particularly useful information for flood management personnel (10).

2.1 Model Overview

We consider a mountain watershed with a set of properties, $\mathbf{p}$, that control the volumetric flow rate of clear streamflow, Q, and sediment, J, in response to precipitation, P. Elements of $\mathbf{p}$ may include various factors such as watershed morphology, soil properties, vegetative cover, or burn severity, and precipitation can be interpreted in various ways (e.g., hourly, daily). For the moment, we leave this in a general form so the derivation herein is most easily transferred between systems and poised to leverage the best available information on a site-by-site basis. Hence, we write streamflow and sediment flux at the watershed scale as follows,

$$Q_{\mathrm{w}} = f_Q(\mathbf{p}, P) \tag{2.1}$$

$$J_{\mathrm{w}} = f_J(\mathbf{p}, P) \tag{2.2}$$

where the subscript w denotes *watershed* and the functions $f_Q()$ and $f_J()$ characterize peak streamflow and peak sediment fluxes, respectively. For this study, we use the Rational Method to compute Q_{w} as follows,

$$Q_{\mathrm{w}} = \frac{cPA}{T_{\mathrm{p}}} \tag{2.3}$$

where c is a dimensionless runoff coefficient representing the ratio of rainfall to surface runoff, P is the daily rainfall accumulation, A is the watershed area, and T_{p} is a time scale representing the time to peak of a triangular hydrograph. We note that model dependency on geomorphological parameters will depend on the choice rainfall-runoff models (e.g., 42; 23; 73).

The total sediment volume associated with a storm event can be written in a general way as follows,

$$\cancel{V}_{\mathrm{w}} = \int_0^{t_{\mathrm{s}}} J_{\mathrm{w}}\, dt \tag{2.4}$$

where t_{s} represents the storm duration.

$$\frac{d\cancel{V}_{\mathrm{b}}}{dt} = J_{\mathrm{w}} - J_{\mathrm{c}} - J_{\mathrm{e}} \tag{2.5}$$

where J_{c} represents the volumetric flux of sediment flowing out of the debris basin and into the flood *channel*, and J_{e} represents the flux of sediment removed from the debris basin by *excavation*. The sediment flux from the debris basin into the flood channel is assumed to be zero when debris basin storage is below capacity and equal to the inflow rate otherwise,

$$J_{\mathrm{c}} = \begin{cases} 0 & \text{if } \cancel{V}_{\mathrm{b}} < \cancel{V}_{\mathrm{b}}^{\mathrm{des}} \\ J_{\mathrm{w}} & \text{otherwise} \end{cases} \tag{2.6}$$

where $\not{V}_{\mathrm{b}}^{\mathrm{des}}$ represents the *design* capacity of the debris basin. The excavation flux is driven by human activity and generally occurs episodically between precipitation events. For example, excavation may occur over several days to weeks during dry weather periods once the infrastructure has filled to a cleaning threshold (e.g., 85% full), subject to various constraints such as the availability of funding, wetland protection policies, and the Endangered Species Act (116). J_{e} can thus be considered a function that is prescribed to vary over time depending on local maintenance practices. Additional details on the implementation of maintenance protocols within the model are provided in Section 2.5.

If the debris basin attenuates the flood peak, then the peak flow rate entering the channel can be expressed as a fraction of the peak flow from the watershed,

$$Q_{\mathrm{c}} = \alpha_{\mathrm{b}} Q_{\mathrm{w}} \tag{2.7}$$

although in many cases the debris basin will not be designed to attenuate the flood peak and thus $\alpha_{\mathrm{b}} = 1$.

The bulked flow of water and sediment, a simple sum of Eq. 2.1 and 2.2, has been previously introduced for sizing infrastructure and quantifying hazards in areas impacted by mud and debris flows and appears as follows,

$$B = Q + J = kQ \tag{2.8}$$

where k represents a bulking factor expressed as follows,

$$k = \frac{Q+J}{Q} = \frac{1}{1-\frac{c_{\mathrm{v}}}{100}} \tag{2.9}$$

where c_{v} represents the percentage concentration of sediment by volume in the bulked flow. Streamflow in small watersheds and alluvial fans is typically characterized by a bulking factor of 1.25 or less (1.0 corresponds to clear water), but after burn events, watersheds may produce hyperconcentrated flows with a bulking factor of up to 1.67 or mud and debris flows with a bulking factor of 2.0 or greater (48). The magnitude of the bulking factor, k, is varied over time to represent the effects of the occurrence and severity of wildfires on watershed hydrology, as described in detail in Section 2.2.

Flood hazards downstream of mountain watersheds occur when the bulked flow rate into the flood channel, B_{c}, exceeds the channel capacity (more information on how channel design capacities are typically determined can be found in Section 2.4). While flood channels are designed to accommodate a peak discharge associated with a storm or flood of a certain return period, over time they may fill with sediment and may also grow vegetation that reduces channel capacity. Consequently, channel capacity is assumed to decrease with sedimentation as follows,

$$D_{\mathrm{c}}^{\mathrm{eff}} = \begin{cases} D_{\mathrm{c}}^{\mathrm{des}}\left(1-\frac{\cancel{V}_{\mathrm{c}}}{\cancel{V}_{\mathrm{c}}^{\mathrm{des}}}\right) & \text{if } \frac{\cancel{V}_{\mathrm{c}}}{\cancel{V}_{\mathrm{c}}^{\mathrm{des}}} < 1 \\ 0 & \text{otherwise} \end{cases} \tag{2.10}$$

where $D_{\mathrm{c}}^{\mathrm{des}}$ is the design capacity of the channel, $\cancel{V}_{\mathrm{c}}$ is the volume of sediment in the channel and $\cancel{V}_{\mathrm{c}}^{\mathrm{des}}$ is the design volume of the channel. Now that both the bulked flow rate in the channel and the channel capacity are established, the flood hazard, H, is given by the exceedance of channel flow over capacity as follows,

$$H = \begin{cases} B_\mathrm{c} - D_\mathrm{c}^\mathrm{eff} & \text{if} B_\mathrm{c} > D_\mathrm{c}^\mathrm{eff} \\ 0 & \text{otherwise} \end{cases} \tag{2.11}$$

The above formulation captures the interdependence between wildfires, precipitation, infrastructure sedimentation and and hazards, and is poised to inform research into the ways in which flood hazards are impacted by changes in fires, rainfall, infrastructure design, and infrastructure maintenance. Several modes of interdependence are captured by the model as follows: First, wildfires alter watershed properties, $\mathbf{p}$, that increase the bulk discharge (Eq. 2.8) through increases in the clear water flux (Eq. 2.1) and sediment fluxes (Eq. 2.2). Secondly, bulked flows that cannot be contained by debris basins reduce the capacity of flood channels (Eq. 2.10) and lower the threshold for channel bank overtopping (Eq. 2.11). And third, the capacity of debris basins and channels is impacted by excavation and cleaning schedules, which in turn are impacted by available funding and various environmental constraints (Section 2.5).

2.2 Wildfire occurrence and severity models

The bulking factor, k, is used to quantify the effect of wildfire on streamflow and sediment flux as a function of the time elapsed since the fire occurred. Multidecadal records of sediment production and streamflow from the San Gabriel Mountains of southern California show that the effect of wildfire on erosion and runoff is greatest immediately following the fire, which strips hillslopes of vegetation and may alter surficial soil properties, and decays exponentially during the first five years following fire as vegetation and surficial soils recover (79). Studies of sediment yields in the Transverse Ranges of southern California have used a similar exponential decay function termed a “lingering effect” to model the decreasing influence of wildfire on sediment production over time as watershed vegetation recovers; in these studies, the decay constant has been varied to represent a recovery time (i.e., time to return to pre-fire conditions) of two to ten years (39; 38). Hence, the occurrence of a wildfire is represented by an increase in the bulking factor from a pre-fire, baseline level, k_0, to a post-fire level, k_1. Following the start of the fire, the bulking factor decays exponentially according an adjustable parameter termed the “recovery timescale” of the watershed, T_r, as follows,

$$k(t) = k_0 + (k_1 - k_0)\, e^{-t/T_\mathrm{r}} \tag{2.12}$$

where t is the number of days elapsed since the start of the wildfire. Once the bulking factor falls within 1% of k_0, the watershed is no longer considered to be actively burned, and $k(t) = k_0$ until the next fire occurs. Thus, the recovery time of the watershed following a given fire will depend on the value of the post-fire bulking factor, k_1, which is taken to be a proxy for the severity of the fire. The greater the k_1, the longer it will take for the bulking factor to return to its baseline level, k_0. For each wildfire, k_1 is simulated stochastically following Equation 2.14 below.

Fire occurrence is modeled using a MC method that makes use of the probability that a fire will occur on a given day during the fire season, p_f. This daily exceedance probability is modeled as a Bernoulli random variable as follows,

$$p_\mathrm{f} = 1 - \left(1 - \frac{1}{T_\mathrm{f}}\right)^{1/n} \tag{2.13}$$

where T_f is the annual fire interval and n is the number of days in the fire season. The parameter T_f is adjustable and can be changed to simulate the effect of different historical or projected fire frequencies on post-fire flood hazards. On each day of the fire season, the output from a uniform number generator, $u \sim U(0,1)$, is compared to p_f. If $u < p_\mathrm{f}$, an active burn is initiated and the bulking factor for that day is set to k_1. Thereafter, the magnitude of the bulking factor will decay exponentially according to Equation 2.12 until it is within 1% of the pre-fire bulking factor, at which point it will be reset to k_0. Otherwise, if $u \geq p_\mathrm{f}$, then $k(t) = k_0$.

In this study, fire occurrence is limited to the months of July to August ($n = 62$) according to the peak fire season in California (81), but can be adjusted based on the fire season of any region or to simulate different climate change scenarios. We consider fire intervals of 50, 20, 15, 10, 5 and 2 years based on a map of fire intervals for major vegetation types in California from 1908-2012, which shows that the range of fire intervals for mountain watersheds in southern California spans from 7 to 52 years (151). We include the 2-year and 5-year fire interval scenarios to represent possible futures in which wildfire frequency has increased relative to historical levels. Note that the selection of the 2- and 5-year fire intervals is not based on specific predictions of future wildfire frequency in the region, but rather is intended to illustrate the sensitivity of post-fire flood hazards to hypothetical increases in fire frequency. In an effort to avoid an overly complex model of the effect of wildfire on watershed hydrology, only one active burn can be simulated at a time, which is a reasonable assumption at the watershed scale since a wildfire consumes fuel, and another wildfire is unlikely to occur in the same area while the watershed is recovering (96).

Given the considerable natural variability in fire intensity and thus burn severity of wildfires that may occur within a watershed over time, the post-fire bulking factor, k_1, is modeled as a uniformly distributed random variable with a specified range as follows,

$$k_1 = k_1^{\min} + (k_1^{\max} - k_1^{\min})\, v \tag{2.14}$$

where $k_1^{\min}$ and $k_1^{\max}$ are the lower and upper limits of the range, respectively, and $v \sim U(0, 1)$. We use a uniform random distribution since no prior information is known about the distribution of post-fire bulking factors, and thus assign probabilities equally to all possible bulking factors within the specified range. The limits of the post-fire bulking factor range can be selected based on the range of observed sediment fluxes from a given watershed or to represent the effect of different burn severities on post-fire sediment fluxes. We assume that the post-fire bulking factor increases with increasing burn severity, an assumption supported by studies that found increasing sediment fluxes with increasing burn severity class (16; 39; 160).

By representing wildfire occurrence and severity as stochastic processes, many scenarios of varying fire frequencies and severities can be simulated and the potential effects of wildfire characteristics on post-fire flood hazards are more thoroughly explored. For this study, k_1 was uniformly sampled from a range representing the severity of a fire as follows:

1. Low burn severity: $1.10 < k_1 < 1.25$
2. Moderate burn severity: $1.25 < k_1 < 1.67$
3. High burn severity: $1.67 < k_1 < 2.86$

We chose these ranges for each burn severity class because they roughly demarcate transitions in flow types between normal streamflow, hyperconcentrated flow, and mud flows and debris flows (48).

2.3 Precipitation model

Following Wilks (172), precipitation was simulated as a stochastic process using a first-order Markov chain to describe precipitation occurrence and MC sampling from an appropriate probability distribution to describe precipitation amounts for days with rain (e.g., 121; 141). The Monte Carlo Markov Chain (MCMC) rainfall simulator was developed using a long-term daily precipitation record (1932-2020) from the Big Tujunga Dam station in Los Angeles, California (ID: USC00040798) retrieved from the Climate Data Online database maintained by the U.S. National Oceanic and Atmospheric Administration (NOAA). This meteorological station was chosen for its length of record and its location at high elevation in the San Gabriel Mountains, since watersheds prone to post-fire flood hazards tend to be mountainous.

To preserve the distribution of wet versus dry years present in the long-term precipitation dataset, we divided the data into subsets for wet years (N=27 years) and dry years (N=44 years), where "wet years" were defined as those with total annual precipitation greater than or equal to the mean. Years missing 10% or more daily values were excluded from the analysis. We used the wet-year and dry-year designations to calculate the conditional probability of transitioning from a dry year to a wet year, p_{DW}, and from a wet year to a wet year, p_{WW}. This was done by counting the number of transitions for each possible type of transition: dry-to-wet (DW), dry-to-dry (DD), wet-to-dry (WD), wet-to-wet (WW). Then the annual transition probabilities were calculated as follows,

$$p_{\mathrm{DD}} = \frac{F_{\mathrm{DD}}}{N_{\mathrm{D}}} \tag{2.15}$$

$$p_{\mathrm{DW}} = 1 - p_{\mathrm{DD}} \tag{2.16}$$

$$p_{\mathrm{WW}} = \frac{F_{\mathrm{WW}}}{N_{\mathrm{W}}} \tag{2.17}$$

where F represents the number of times a transition occurred and N represents the number of wet or dry years on record (143; 133; 1).

Modeling daily precipitation occurrence as a first-order Markov process assumes that the probability of observing precipitation on a given day depends only on whether precipitation occurred the previous day, regardless of whether precipitation occurred on earlier days in the time series. We define a "wet day" as a day on which at least the minimum reportable precipitation amount occurred, 0.254 mm. The parameters p_{01} and p_{11} represent the conditional probability of transitioning from a dry day to a wet day and transitioning from a wet day to a wet day, respectively. These daily transition probabilities were estimated from the wet-year and dry-year subsets separately by grouping the data by ordinal day (1 to 365, where 365 represents December 31 of a non-leap year) and performing the same calculations in Equations 2.15-2.17 on a daily time scale. Again, years missing 10% or more daily values were excluded from the analysis. Average daily transition probabilities were calculated using a 14-day moving average of the empirical probabilities to smooth extreme values (Figure A.1).

The MCMC rainfall simulator generates $m \times 365$ days of a daily precipitation time series, where m is the number of years in the time series, as follows: for the first year of the time series, a random number is generated to determine the wet or dry status of the first year, with a 50% chance for either outcome. The appropriate wet-year or dry-year daily transition probabilities are then used to simulate one year of a daily precipitation time series. This is done by generating a random number to determine the wet/dry status of the first day in the time series, which in turn determines the "threshold transition probability," p_{t}, that will be used to predict the wet/dry status of the next day. The threshold transition probability for day t is given by,

$$p_{\mathrm{t}} = \begin{cases} p_{01} & \text{if } X_{t-1} = 0 \\ p_{11} & \text{if } X_{t-1} = 1 \end{cases} \tag{2.18}$$

For each day of the year, p_{t} is compared to the output from a uniform random number generator, $u_t \sim U(0,1)$. Rainfall occurrence on day t is then calculated as follows,

$$X_t = \begin{cases} 1 & \text{if } u_t \leq p_{\mathrm{t}} \\ 0 & \text{otherwise} \end{cases} \tag{2.19}$$

The precipitation amount for each wet day is determined by randomly sampling from a Weibull distribution fit to the observed non-zero precipitation amounts from wet years and dry years separately. The Weibull distribution was selected after comparing the fit of four probability distributions commonly used for non-zero rainfall amounts in the literature (e.g., 135; 161; 178). Goodness of fit was assessed with a comparison of quantile-quantile (Q-Q) plots between the fitted probability distributions (Figure A.2) and Q-Q plots of the wet-year and dry-year subsets versus the fitted Weibull distribution (Figure A.3).

The wet/dry status of the next year in the time series is determined in a similar manner to that shown in Equations 2.18 and 2.19, except the annual transition probabilities, p_{DW} and p_{WW}, are used.

2.4 Infrastructure design standards

In southern California, due to the frequency of post-fire flood events, many flood control agencies estimate bulking factors or sediment yields for watersheds that produce high levels of sediment, burn frequently, or are located upstream of critical infrastructure, such as hospitals or transportation infrastructure (48). Bulking factors are applied as a safety factor to the peak discharge used to design flood control channels, while sediment yields are estimated to determine the design capacity of debris basins. The specific equations and procedures used to determine design bulking factors and sediment yields vary widely from county to county, but in general they involve a design storm of a certain return level, which is translated into a design peak discharge using a rainfall-runoff relationship. Two counties in particular, Los Angeles and Ventura County, provided detailed descriptions of the design standards for debris basins and flood channels in design manuals (77; 76; 158; 159). Specifically, Los Angeles County requires all debris basins to be designed for a 50-year design storm (termed the "Capital Flood"), and the sediment yield for a "design debris event" is determined using curves calculated for each "debris producing area" in the county based on watershed area and an assumption of four years since the watershed was last burned. Bulking factor curves are used to calculate bulking factors used to design flood channels in sediment producing watersheds where a debris basin does not exist (77). Ventura County, on the other hand, requires debris basins for watersheds with areas <5 mi^2 to be designed to hold 125% of the sediment volume expected from a 100-year design storm, provided sufficient land is available. The design sediment yield is determined using a regression equation that takes into account the watershed area and morphology, as well as a dimensionless "fire factor" that represents the percentage of non-recovery of a watershed following a burn; normal (i.e., non-emergency) design conditions assume 4.5 years since the watershed was last burned. It should be noted that the Ventura County Debris Basin Manual states, "A number of the debris basins do not have sufficient storage for the 100-yr debris yield and therefore could possibly fill with sediment during extreme storm events" (158). Bulking factors are applied to the design of flood channels downstream of watersheds known to produce high levels of sediment or experience frequent fires as well as those designed to protect critical infrastructure shortly after a fire (159).

The two key design criteria implemented in the model to represent regional differences in infrastructure design standards are the precipitation of the design storm, P^{des}, and the decision whether to use a clear-water or a bulked peak discharge as the design discharge. In the model presented here, P^{des} is determined by performing an extreme value analysis on a 100-year precipitation time series generated by the MCMC rainfall simulator. A Generalized Extreme Value distribution was fit to the 100-year time series of annual maximum precipitation to determine the magnitudes of the 50-year and the 100-year design storms (Figure A.4). Next, the peak discharge associated with the return level of the design storm is calculated using the Rational Method as follows,

$$Q_{\text{w}}^{\text{peak}} = \frac{cP^{\text{des}}A}{T_{\text{p}}} \tag{2.20}$$

where $Q_{\text{w}}^{\text{peak}}$ is the peak clear-water discharge from the watershed, c is a dimensionless runoff coefficient, A is the watershed area, and T_{p} is a time scale representing the time to peak of a triangular hydrograph. Note, however, that any rainfall-runoff model may be used to calculate $Q_{\text{w}}^{\text{peak}}$.

The design discharge may be calculated as either a clear-water or a bulked volumetric flow rate. If the bulked design discharge is used, a design bulking factor, k_{des}, will be applied to the clear-water discharge, $Q_{\text{w}}^{\text{peak}}$, to determine the design capacity of the flood control channel. Otherwise, the channel design capacity is set equal to $Q_{\text{w}}^{\text{peak}}$. Similarly, the capacity of the debris basin also depends on the design storm return period and whether bulking is applied to the flow from the watershed. Based on a clear-water design standard or a bulked design standard, the capacity of the debris basin is calculated as follows,

$$
{\rlap{-}V}_{\mathrm{b}}^{\mathrm{des}} = \begin{cases} 0.15 \times cP^{\mathrm{des}}A & \text{clear-water standard} \\ (k_{\mathrm{des}} - 1)cP^{\mathrm{des}}A & \text{bulked standard} \end{cases} \tag{2.21}
$$

assuming that the concentration of sediment in normal streamflow within an alluvial fan is typically at most 15% by volume (48). Note that the use of the 15% sediment concentration is not a safety factor, but rather an approximation of the typical sediment flux expected from an unburned watershed used to determine the design capacity of the debris basin assuming a clear-water design standard.

In the present study, we compare four sets of infrastructure design standards generalized from the design approaches described above:

1. 50C: 50-year design storm ($p_{\mathrm{p}} = 0.02$), clear-water design discharge
2. 50B: 50-year design storm ($p_{\mathrm{p}} = 0.02$), bulked design discharge
3. 100C: 100-year design storm ($p_{\mathrm{p}} = 0.01$), clear-water design discharge
4. 100B: 100-year design storm ($p_{\mathrm{p}} = 0.01$), bulked design discharge

It is important to note that by including a clear-water design discharge we do not imply that such a design standard is operationally applied to watersheds that are known to burn frequently of produce high levels of sediment. Rather, it is included to provide a conceptual contrast to the effects on the flood hazard of bulking the design discharge. Including a clear-water design standard also allows the exploration of what might happen if a watershed not previously identified as fire-prone was burned and its infrastructure was not designed to convey significantly bulked flows.

Finally, we note that the flood infrastructure design standards described herein are representative of debris basin design globally, in that the capacity of the infrastructure is determined based on the magnitude of an event with a particular (design) return period (65; 64; 101). We acknowledge, however, that differences in designs can be expected based on differences in equations for frequency analysis and the estimation of (post-fire) flow rates.

2.5 Infrastructure maintenance models

One example of a typical maintenance schedule for debris basins in Riverside County is annual inspection during the summer months to determine maintenance needs; if the cleaning threshold is met or exceeded, the debris basin will be returned to 100% capacity. In a year during which a major fire has occurred, the capacity of debris basins is restored or sometimes enhanced beyond 100% (i.e., with excavation beyond the initial grading of the basin) as soon as possible following fire containment. While excavation of debris basins can occur during the wet season, it is avoided by flood control agencies when possible because wet sediment is difficult to excavate, costly to move, and may not be accepted at the ultimate location of disposal. The excavation rate varies depending on how urgently the need for cleaning is, i.e., how close the debris basin is to overfilling, with faster cleaning rates and higher maintenance costs the closer the capacity is to 0% (116).

These maintenance protocols have been generalized and implemented as four maintenance approaches:

1. S: Summer Cleaning

2. SA: Summer + After-fire Cleaning
3. SAW7: Summer + After-fire + Wet Season Cleaning with 7-day waiting period
4. SAW1: Summer + After-fire + Wet Season Cleaning with 1-day waiting period

When the Summer Cleaning model is active, the levels of sediment in the debris basin and the flood channel are each checked each day during the summer months (June 1 to September 29) of each year; if the level of sediment in a given facility is greater than or equal to the cleaning threshold, the facility will be "excavated" and returned to full capacity.

When the After-fire Cleaning model is active, the level of sediment in the debris basin is checked on September 30 of each year, the nominal last day of the summer; if the level of sediment in the debris basin is greater than or equal to the cleaning threshold, the debris basin will be "excavated" and returned to full capacity.

Finally, when the Wet Season Cleaning model is active, the level of sediment in the debris basin is each checked each day during the wet season (October 1 to April 30) of each year; if the level of sediment in the debris basin is greater than or equal to the cleaning threshold *and* if a certain number of days have passed without rain, the debris basin will be "excavated" at a certain cleaning rate (volume of sediment per day). The "waiting period" between storms and cleaning rate are used to represent the effort to incrementally excavate sediment during dry periods between storms in the wet season; both parameters can be estimated from debris basin cleaning records.

2.6 Model Summary and Limitations

The framework developed herein for hazard simulation can be considered a lumped system dynamics model for estimating exceedance probabilities in channel reaches downstream of debris basins and upstream of confluences from other streams. Key physical elements of the framework include the watershed, debris basin, and flood channel as shown in Fig. 2.1, and the key state variables include the bulking factor, debris basin storage of sediment, channel storage of sediment, daily precipitation accumulation, daily sediment fluxes, and flood peaks accounting for water and sediment fractions. Each of these state variables represents approximations of processes that could be subject to more refined modeling. In particular, the generation of runoff and entrainment of solids from hillslopes and channels involves many different physical processes active at a range of spatial and temporal scales (62; 96; 134). It should be noted that while unit-area runoff and sediment fluxes are generally expected to decrease with increasing contributing area in semiarid regions (e.g., 91; 97; 164), the model as currently configured estimates that these variables are insensitive to changes in watershed area (Figure S5). This is a consequence of calculating clear-water runoff from the watershed (Q_{w}) using the Rational Method (Equation 2.3) and sediment flux from the watershed (J_{w}) as a linear function of Q_{w} and the bulking factor, k. Additionally, the clogging of channels may result from complex interactions between channel geometry, channel vegetation, hydraulic structures, and the flow regime such as whether and to what extent the flow entrains large woody vegetation, mud, and rocks (122; 108; 85). Finally, the probability of wildfire occurrence and the severity of a given wildfire depend on several factors including the availability and composition of fuel, climatic controls such as humidity, and the topography of the landscape (82; 32). In this light, stochastic modeling approaches are advantageous because uncertainty can be captured with random variables that span a range of possible values, as we have demonstrated for the bulking factor.

Chapter 3

PF2HazMo Parameterization, Calibration, and Validation

This chapter presents a systematic approach for applying PF2HazMo to estimate sediment-laden hazards including parameter estimation, model calibration, and validation. The section begins with a description of data sources and methods that support PF2HazMo applications on a catchment-by-catchment basis, continues with results that illuminate model sensitivities and strategies for calibration and validation, and closes with discussion about model strengths and limitations.

3.1 Methods

The methodological sections that follow are organized into six subsections that cover: (1) a description of the study catchments and the data used to force, calibrate, and validate the model; (2) model sensitivity and error propagation analysis; (3) estimation of uncalibrated model parameters; (4) model calibration; and (5) model validation.

3.1.1 Study Sites and Data

A set of three small mountain watersheds (<11 km^2) in Riverside County, California are utilized in this study to present methods of parameter estimation, calibration, and validation for PF2HazMo (Fig. 5.2). These catchments were burned by the 2018 Holy Fire and have similar percentages of area burned, average slope, and aspect (Table 3.4). The Coldwater watershed represents a gauged watershed with a U.S. Geological Survey (USGS) streamgage at its outlet; however, there is no flood infrastructure located downstream. McVicker and Leach watersheds are both ungauged, and each have a debris basin and flood channel located downstream. McVicker is upstream of a concrete-lined channel, while Leach is upstream of an unlined, or soft-bottom, flood channel, allowing us to compare how the model performs for different channel types. Further, all three basins are located upstream of urban areas (dark grey areas in 5.2, defined by population density >1,000 people per sq. mi.), and hence estimation of post-fire flood and debris flow risks is important for public safety.

Environmental Setting

The study watersheds are located in the Santa Ana Mountains of southern California within the Santa Ana River watershed, which drains into the Pacific Ocean. The Santa Ana Mountains are part of the Peninsular Ranges, a group of mountain ranges oriented from north to west that are characterized by Jurassic and Cretaceous plutonic, mainly granitic rock that are more resistant to erosion than the neighboring Transverse Ranges to the north (60). In particular, the underlying lithology of the study sites is Mesozoic to Precambrian metamorphic rocks intruded by granitic rocks as well as Mesozoic volcanic rocks (14). The climate is classified as hot-summer Mediterranean to hot semi-arid according to the Köppen climate classification (7). Average annual precipitation in the region is about 451 mm, with most of it falling as rain from October to April (109). The vegetation is Chaparral-dominated;

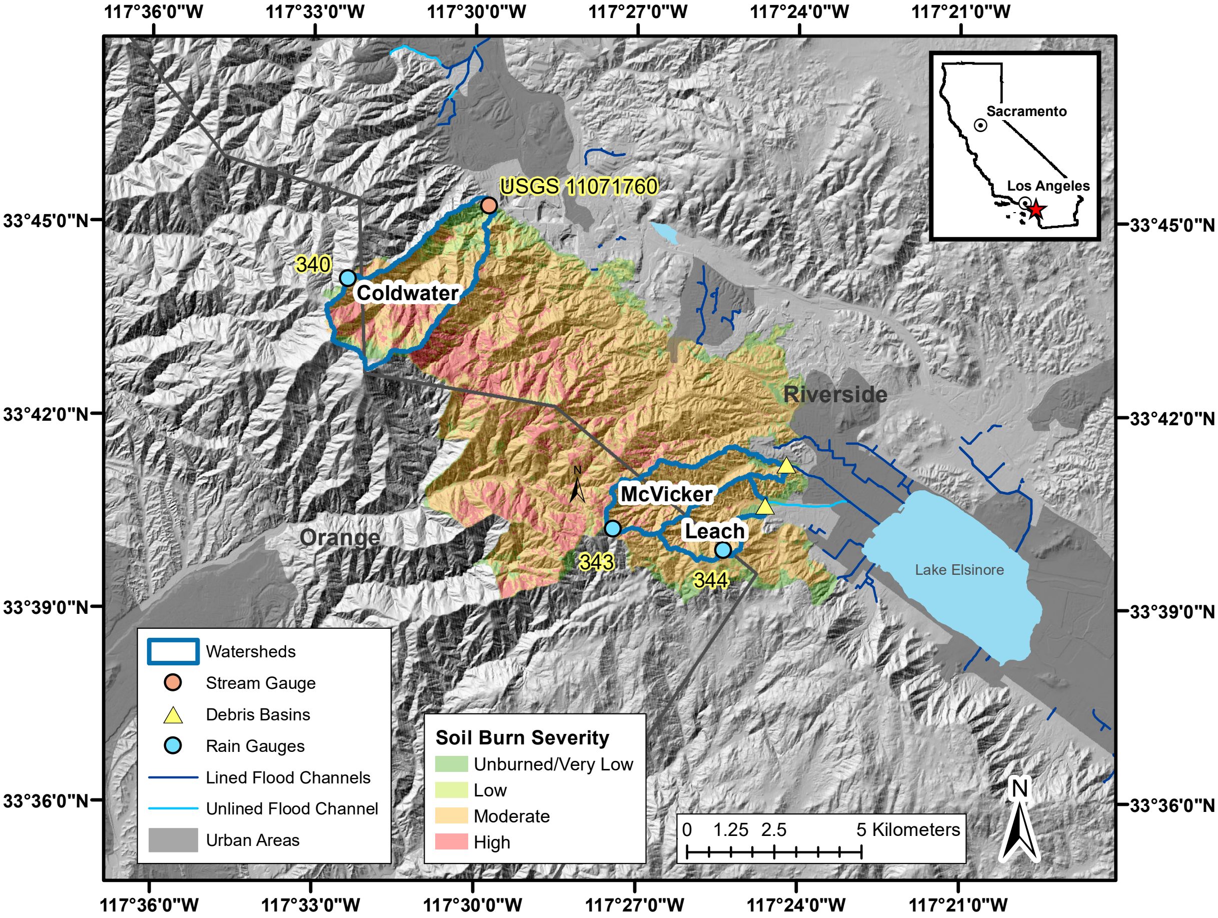

Figure 3.1: Map of study area showing study watersheds, burn severity for 2018 Holy Fire, and locations of rain gauges, stream gauge, and flood control infrastructure.

.

indicative vegetation types include Diegan coastal sage scrub, mesic chaparral, and sparse coniferous vegetation (170; 113).

The mean fire return interval, or the average time between fires under the presumed historical fire regime, for these watersheds is approximately 40 years (78). The 2018 Holy Fire was the first major wildfire to affect these watersheds (i.e., to burn >10% of the watershed area) since 1987 for the Coldwater watershed and since 1954-56 for the Leach and McVicker watersheds, according to historical fire perimeter data (13).

On 6 August 2018, the Holy Fire ignited near Trabuco Canyon in the Santa Ana Mountains and burned 9,300 hectares by the time it was contained on 17 October 2018 (13). Mud and debris flows subsequently occurred during the 2018-19 wet season (117).

Rainfall and Runoff Data

Rainfall data from three tipping bucket rain gauges operated by Riverside County Flood Control and Water Conservation District (hereafter referred to as "Riverside County") were acquired to force PF2HazMo simulations of the 2018-19 wet season. Precipitation data was available for the Coldwater rain gauge (340, Figure 5.2) from 19 November 2018 to 1 April 2019, while data availability for the McVicker (343) and Leach (344) rain gauges was from 1 November 2018 to 1 March 2021. The rain gauges recorded precipitation depth at irregular time intervals in increments of 0.04 inches per tip; the raw data was aggregated by day to force model simulations at a daily timestep. Rain gauge data was also used to estimate the time to peak model parameter, tp, as described in Section 3.1.2.

Instantaneous streamflow data at an interval of 15-minutes from 4 December 2018 to 31 March 2019 were retrieved for USGS streamgauge 11071760 and used to calibrate the Runoff Response parameter. Peak flows were identified based on a visual analysis of the maximum daily discharge time series and an understanding of when the major storm events of the wet season occurred from discussions with Riverside County; the total daily precipitation, maximum daily flow rate time series, and observed peak flow rates for Coldwater watershed are shown in Figure B.1. These observed post-fire peak flows were compared to the simulated daily peak flows that occurred on the same dates as the observed flows to calculate model error metrics and calibrate the model.

Overtopping Data

Time-lapse cameras installed by Riverside County at the Leach and McVicker debris basins provided observations of debris basin overtopping that were used to validate the model. Time-lapse footage taken on days with major storm events (29 November 2018, 6 December 2018, 17 January 2019, 2 February 2019, and 14 February 2019) were analyzed. Three (3) overtopping events were observed at Leach debris basin on 6 December 2018, 17 January 2019, and 14 February 2019, while one (1) overtopping event was observed at McVicker debris basin on 14 February 2019. Additionally, drone survey footage of the flood channel downstream of the Leach watershed showed evidence of channel overtopping on 14 February 2019. To the authors' knowledge, no video, photographic, or anecdotal evidence exists for the overtopping of the flood channel downstream of the McVicker watershed during the 2018-19 wet season.

3.1.2 Model Sensitivity and Error Propagation

Characterizing the sensitivity of PF2HazMo to the parameters listed in Table 3.1 and their mutual influence on model errors is important, and can be helpful, for guiding model parameter estimation and calibration strategies. Here, "sensitivity analysis" implies varying the value of each model parameter by a small amount, one at a time, and quantifying the resulting effect on the model output to determine which parameters have the greatest influence

Table 3.1: PF2HazMo parameters.

Parameter Name	Symbol	Definition
Watershed Area	A	Drainage area of mountain canyon.
Runoff Response	c_t	Ratio of the runoff coefficient to the time to peak.
Time to Peak	t_{p}	Duration from beginning of storm to peak runoff.
Fire Interval	t_{f}	Recurrence interval of wildfires in years.
Post-fire Bulking Factor	k_1	Ratio of the combined water and sediment volumetric flux to the water volumetric flux.
Recovery Timescale	t_{r}	Time scale for watershed recovery after fire.
Debris Basin Design Capacity	$\rlap{-}V_{\mathrm{b}}^{\mathrm{des}}$	Storage capacity of sediment/debris basin.
Flood Channel Design Capacity	$D_{\mathrm{c}}^{\mathrm{des}}$	Flow capacity of flood channel downstream of debris basin.
Infrastructure Cleaning Threshold	$\rlap{-}V_{\mathrm{thresh}}$	Fraction filled that triggers cleaning.
Wet Season Cleaning Waiting Period	w	Number of days with no rain needed before debris basin cleaning can commence.
Wet Season Debris Basin Cleaning Rate	r	Daily excavation rate for debris basin during wet season.

on model results. In contrast, "error propagation analysis" implies simultaneous varying all parameter values across their respective ranges and assessing their collective effect on errors in model outputs.

Sensitivity Analysis

Table 3.1 presents the model parameters included in the sensitivity analysis. Fire interval was not included in the sensitivity or error propagation analyses because the purpose of the tests is to determine the sensitivity of model parameters that could be calibrated to a specific site, but the fire interval is a parameter based on either the historical fire regime or is set to a value representative of future fire regimes and is not a focus of calibration efforts. Additionally, since the model of wildfire occurrence is stochastic, implementing a given fire interval entails differences in the relative timing of wildfires and precipitation between simulation trials, which makes it difficult to distinguish the effect of varying the parameter's value from the effect of varying the sequencing of wildfires and precipitation.

For each parameter except for the wet season debris basin cleaning rate (r) and the peak flow timescale (t_p), the mean parameter estimate was used as a baseline value. Observations were used to define the ranges for the r and t_p parameters, and since the distributions were skewed, we used the median instead of the mean as the baseline. For each parameter, the baseline value was increased or decreased by 10%. Model outputs used to measure sensitivity included the number of channel exceedances, number of debris basin exceedances, sum of sediment flows into the debris basin, sum of sediment flows into the channel, sum of overbank flows, and maximum overbank flows over the course of a one-year simulation period. These six output variables were chosen to capture both hazard variables and sediment volumes that bear on management costs.

For sensitivity analysis, a one-year daily time series of precipitation was stochastically generated using the Monte Carlo Markov Chain (MCMC) rainfall simulator described in Jong-Levinger et al. (66); the same precipitation time series was used in all simulation trials for consistency. The simulation starts on June 1st and continues through May 31st of the following year (365 days), proceeding at a daily time step. Since fires typically occur during July through August in California (81), for all simulation trials the fire was set to occur on July 1st, one month after the start of the simulation, to ensure that variability in model outputs was due to changes in parameter values rather than the timing of the fire and precipitation.

Model sensitivities were quantified using the Sensitivity Coefficient, ϕ_i, defined by the ratio of the relative change in model output to the relative change in parameter values as follows:

$$\phi_{i,j} = \frac{\Delta y_i/\overline{y}}{\Delta x_j/\overline{x}} \tag{3.1}$$

where y_i represents model output variable (i = 1, 2, ... m, m=6), x_j represents model parameters (j = 1, 2, ... n, n=10) and $\overline{x}$ and $\overline{y}$ represent mean/median values (50). Model parameters were subsequently ranked by sensitivity coefficient for each output variable, and a count of the number of times a parameter was ranked among the top three most sensitive parameters was taken as on overall measure of parameter importance.

Error Propagation Analysis

Error propagation analysis accounts for the combined influence of all parameters on model outputs when varied across their statistical distributions, unlike sensitivity analysis which isolates the effect of small changes to individual parameters (36). A total of 500 one-year model simulations were completed with all parameters randomly sampled from a uniform distribution between the reported minimum and maximum value, except for the wet season debris basin cleaning rate (r) and the peak flow timescale (t_p). Observations were available for these parameters, so we sampled the data uniformly at random, with replacement (n=66 and n=80, respectively).

Once model output data were generated across the 500 parameter combinations, correlation and partial correlation coefficients were first computed between each model output variable and each parameter. Second, model parameters were ranked by highest squared correlation coefficient. And third, the number of times a parameter ranked in the top three for each model output variable was counted to obtain an overall ranking of each parameter relative to its error propagation.

Model Parameter Range Estimation

The ranges of values for each model parameter are presented in Table 3.2 based on the following considerations: The range of values for the runoff response parameter, c_t, was estimated by first taking the runoff coefficient for undeveloped land between 0.1 and 0.9 (87, Table 2). Next, storm duration was computed for each site using 2018-21 rain gauge records for Leach (344) and McVicker (343) (Figure 5.2), and the time to peak parameter tp was estimated as storm duration divided by 2 (136).

Both c_t and tp were considered in the sensitivity and error analysis. The c_t parameter is used to calculate peak discharge from the watershed outlet, but tp is used separately to calculate the volume of sediment from the watershed outlet ($\forall_s = Q_w t\mathrm{p}(k-1)$); thus it is important to understand the sensitivity of both parameters. Storm duration (taken as twice the time to peak) was estimated from the rain gauge records by defining storms as continuous rainfall with at least 0.2 inches of depth and 0.1 in/hour of intensity, identifying new storms after 6 hours with <0.05 inches of rainfall. Storm durations >24 hours were excluded since the model timestep is daily.

Table 3.2: Model parameter ranges used in the sensitivity and error analyses.

Parameter Name	Symbol	Units	Minimum	Mean/Median	Maximum
Runoff Response	c_t	1/seconds	2.33×10^{-6}	7.52×10^{-4}	1.50×10^{-3}
Time to Peak	t_p	hours	0.167	4.90	11.9
Post-fire Bulking Factor	k_1	unitless	1.25	2.06	2.86
Recovery Timescale	t_r	days	140	637	1,134
Debris Basin Design Capacity	$\not{V}_\mathrm{b}^\mathrm{des}$	m^3	1.09×10^4	1.50×10^5	2.89×10^5
Flood Channel Design Capacity	$D_\mathrm{c}^\mathrm{des}$	m^3/s	1.94	484	965
Infrastructure Cleaning Threshold	$\not{V}_\mathrm{thresh}$	% filled	75	85	95
Wet Season Cleaning Waiting Period	w	days	1	7	14
Wet Season Debris Basin Cleaning Rate	r	$\mathrm{m}^3/\mathrm{day}$	336	1624	4826

The minimum value for the post-fire bulking factor represents the lower bound of hyperconcentrated flow, while the maximum value represents the upper range of debris flow (48).

PF2HazMo accounts for watershed recovery from fire with an exponential decay model for the bulking factor, k, as follows,

$$k(t) = k_0 + (k_1 - k_0)e^{-t/t_\mathrm{r}} \tag{3.2}$$

Previous studies have reported that the recovery time is between two and ten years (39; 38; 79), and thus t_r was estimated by assuming $k(t) = 1.01k_0$ when t equals the the observed recovery time, and rearranging Eq. 3.2 to solve for t_r.

We calculated debris basin capacity according to Equation 21 and channel capacity according to Equation 20 in Jong-Levinger et al. (66) assuming a bulked design standard. Bound estimates were based on a 50-year precipitation return level estimated from extreme value analysis of a long-term daily precipitation record (1932-2020) from the Big Tujunga Dam station in Los Angeles, California (ID: USC00040798) (NOAA), the average drainage area for a watershed in southern California (39), and design bulking factors of 1.15, typical of normal streamflow in an alluvial fan, to 2.0, the highest design bulking factor currently in use in southern California (48). For channel capacity estimation, we used the minimum and maximum values of t_p mentioned above. A minimum runoff coefficient of 0.1 was used as above, but the maximum was set to 0.4 since we found that the resulting number of channel exceedances was zero for most of the simulations otherwise.

The range of cleaning threshold values was based on communication with Riverside County, which typically restores infrastructure to full capacity during the dry season when 85% of the capacity is filled with sediment. The minimum and maximum values were obtained by adding or subtracting 10% of the volume filled.

The range of waiting period values is based on the assumption that maintenance crews must wait between one and 14 days after a storm occurs before excavating sediment from infrastructure based on correspondence with Riverside County.

The range of wet season debris basin cleaning rates is based on daily debris basin cleaning records for Leach and McVicker debris basins from December 2018 to April 2019 provided by Riverside County. The median was used as the measure of central tendency since the distribution was right-skewed.

3.1.3 Parameter Estimation Methods

PF2HazMo is applied by providing estimates for model parameters, some of which are bracketed by previous work or direct measurements, and others which are calibrated. In this section, sources of data for model parameter estimates are reported. Parameters selected for calibration and the calibration approach is described in the following section. A summary of the estimation methods for uncalibrated model parameters is presented in Table 3.3.

Watershed Morphology

Watershed area was estimated using 10-m DEMs from the USGS using ArcGIS (152; 30). Additional watershed characteristics including the mean slope, length of the longest flow path, and relief were needed to estimate the post-fire bulking factor and were calculated by the StreamStats online tool developed by the USGS (153). StreamStats allows the user to specify the location of a watershed outlet and delineates the watershed using a 30-m DEM; these and other watershed characteristics are provided in the Basin Characteristics report.

Time to Peak

While the runoff response parameter, c_t, could be used to calculate peak flows from the watershed using the Rational Method, the time to peak parameter, t_p, needed to be estimated separately to estimate the fluxes of water and sediment entering the debris basin. We assumed each storm could be modeled with a triangular hydrograph with equal rising and falling limbs. The time to peak parameter represents the amount of time between the start of direct runoff production and the peak of the hydrograph, as observed at the watershed outlet. The time to peak was estimated as $\Delta D/2 + L$, where ΔD is the storm duration and L is the watershed lag (136). For each watershed, ΔD was estimated as the median storm duration for the 2018-19 wet season using rainfall data from the rain gauge nearest each watershed. L was estimated using the Soil Conservation Service (SCS) watershed lag method using the watershed characteristics from StreamStats (71).

Table 3.3: Summary table of parameter estimation methods for uncalibrated model parameters.

Parameter Name	Symbol	Approach	Data	Reference
Watershed Area	A	GIS analysis	10-m DEM from USGS	-
Time to Peak	t_{p}	Sum of storm duration divided by 2 and watershed lag	Rain gauge records, watershed morphology	(71)
Post-fire Bulking Factor	k_1	HEC-HMS hydrologic and erosion modeling (curve number and LA Debris Method)	Land cover, soil properties, watershed morphology, burn severity, precipitation frequency curve	(59)
Recovery Timescale	t_{r}	Fit exponential curve to area-averaged vegetation index time series	Satellite-derived NDVI and EVI at 16-day, 250-m resolution from MODIS	(45)
Debris Basin Design Capacity	$\rlap{-}V_{\mathrm{b}}^{\mathrm{des}}$	GIS analysis of DEMs from Riverside County	UAV photogrammetric surveys of debris basins	
Flood Channel Design Capacity	$D_{\mathrm{c}}^{\mathrm{des}}$	2D flood inundation modeling	0.5-m Lidar-derived DEM from Riverside County	(128)
Infrastructure Cleaning Threshold	$\rlap{-}V_{\mathrm{thresh}}$	Communication with Riverside County	-	(117)
Wet Season Cleaning Waiting Period	w	Analysis of excavation records	Excavated sediment volumes at roughly daily intervals	-
Wet Season Debris Basin Cleaning Rate	r	Average daily volume excavated	Excavated volumes of sediment at roughly daily intervals	-

Post-fire Bulking Factor

We estimated the post-fire bulking factor range by developing a lumped (i.e., single-basin) model for each watershed using HEC-HMS software (148), calibrating the curve number parameter to pre-fire peak discharge frequency estimates, then increasing the curve number to reflect the expected post-fire increase in runoff following Livingston et al. (2005). The resulting time series of post-fire discharge and sediment load were integrated over each simulated storm to calculate a range of post-fire bulking factors. The following methods are based on a set of HEC-HMS tutorials developed for the Gallinas Creek Watershed in New Mexico following the 2022 Hermits Peak-Calf Canyon Fire (59).

We used the SCS curve number method as the loss method since there are several studies documenting how the curve number can be adjusted to reflect the post-fire condition (e.g., 138; 43; 21; 18). We calculated an initial estimate for the pre-fire curve number by intersecting National Land Cover Database 2019 land cover data and hydrologic soil group data from the Soil Survey Geographic Database (SSURGO) (29; 137). Using a land use and soil group lookup table, we calculated an area-weighted average curve number for each watershed (58). This curve number was then used to calculate the maximum potential retention, S, and the initial abstraction, I_{a}, assuming $I_{\mathrm{a}} = 0.2S$ following Mockus et al. (94), as well as the watershed lag time following Kent et al. (71). We used the SCS unit hydrograph method as the transform method, using a peak rate factor of 550 based on the steepness of the study watersheds. We forced the model with precipitation frequency estimates for a 2-year to 500-year storm using the frequency storm method and the same basin-averaged precipitation frequency estimates described in Section 3.1.4 to develop a precipitation-frequency curve. To distribute the rainfall throughout the storm over time, we used a precipitation intensity pattern for a 6-hour storm from the Riverside County Hydrology Manual representative of a reasonable distribution of rainfall likely to cause critical runoff conditions during a major storm event (114, Plate E-5.9).

We used the initial pre-fire curve number estimate to simulate the peak discharge frequency curve and compared it to the peak discharge frequency curve retrieved from StreamStats (see Section 3.1.4). We then calibrated the pre-fire curve number to the discharge frequency curve by adjusting it by a constant factor between 0 and 1 until the percent error in the area-normalized runoff volume was less than 10% and the NSE was greater than 0.90.

Next, to obtain the post-fire curve number, we adjusted the calibrated pre-fire curve number using the following two-step procedure developed by Livingston et al. (84): (1) we calculated the percentage of the watershed area burned at moderate and high burn severity of the Burn Area Reflectance Classification map for the Holy Fire to determine the Wildfire Hydrologic Impact classification (5), and (2) we used the corresponding relationship between pre-fire curve number and the post-fire to pre-fire curve number ratio to calculate the corresponding post-fire curve number. The watershed lag was updated to reflect the post-fire curve number.

The final step of calculating the post-fire bulking factor range was simulating post-fire sediment load. We used Los Angeles District Debris Method (LA Debris Method) Equation 1 as the erosion model for McVicker and Leach watersheds and LA Debris Method Equation 2-5 for Coldwater watershed according to the drainage area constraints of each model (40). We chose this erosion model because it consists of multiple equations that can be applied to watersheds with a wide range of drainage areas (0.26-518 km^2) and accounts for the effect of time since fire with a parameter termed the "Fire Factor." The Fire Factor is a dimensionless parameter of the LA Debris Method that represents the impact of wildfire on debris yield with a value of 6.5 representing ten years since 100% of a given watershed burned at a value of 3.15 representing one year since 100% of the watershed burned. Since the goal was to obtain a range of post-fire bulking factors from which to sample randomly, we ran one simulation using a Fire Factor of 6.5 (the "high sediment" scenario) and another using a Fire Factor of 3.15 (the "low sediment" scenario). The LA Debris Method requires an Adjustment-Transposition (A-T) Factor to be specified; this parameter is designed to account for differences in geomorphology between the San Gabriel Mountains of Los Angeles County where the regression equations were developed and that of the watershed of interest (40). For this study, we set the A-T factor to 1.0 due to a lack of sufficient debris yield data for these or surrounding watersheds to estimate it. We note that the actual debris yield of the study watersheds is likely somewhat less than predicted since the Peninsular Ranges in which they are located are known to have a lower debris potential than that of the San Gabriel Mountains (40; 49).

From the resulting simulated time series of post-fire flow rates and sediment loads, we calculated the bulking factor for each storm in the frequency curve as the sum of the volumes of water and sediment integrated over the duration of the storm divided by the volume of water. The minimum and maximum bulking factors estimated from both the high and low sediment scenarios were used to define the bounds of the post-fire bulking factor range.

Recovery Timescale

The recovery timescale parameter, t_{r}, represents the rate of watershed recovery after the watershed is burned by wildfire–that is, the exponential decay rate of the post-fire bulking factor, k_1, back to the pre-fire baseline bulking factor, k_0. The recovery timescale is implemented in the equation for the bulking factor (Eq. 3.2). To estimate the recovery timescale, we assume the watershed vegetation recovers at a rate commensurate to the decay rate of the post-fire bulking factor, since vegetation regrowth is the main process by which soil becomes re-stabilized following wildfires (20; 134). The recovery rate of watershed vegetation was estimated following Gouveia et al. (45), who used post-fire Normalized Difference Vegetation Index (NDVI) time series to model vegetation recovery. NDVI is one of the most common satellite-derived vegetation indices used to study post-disturbance vegetation recovery, and several studies have used NDVI time series to evaluate post-fire vegetation recovery in the southwestern U.S. (e.g., 53; 157; 142). Essentially, since NDVI is an indicator of vegetation greenness, Gouveia et al. (45) define the “lack of greenness,” $y(t)$ as:

$$y(t) = \mathrm{NDVI}(t) - \mathrm{NDVI}^{*}(t) \tag{3.3}$$

where $\mathrm{NDVI}^{*}(t)$ is an annual cycle that represents the “ideally healthy state of vegetation along the phenological year.” The lack of greenness variable drops below zero when a fire burns the vegetation, and an exponential decay curve of the form:

$$y(t) = ae^{-bt} \tag{3.4}$$

where t is the time since the start of the fire and $a = \mathrm{NDVI}(t = 0)$-$\mathrm{NDVI}^{*}(t = 0)$, can be fit to the post-fire time series such that the decay rate parameter, b, may be found through linear regression. Comparing Equations 3.2 and 3.4, it becomes apparent that the recovery timescale may be estimated as $t_{\mathrm{r}} = 1/b$.

We applied this approach to NDVI and Enhanced Vegetation Index (EVI) time series data from the Moderate Imaging Spectroradiometer (MODIS) on the Terra satellite; EVI data were included in the analysis to compare the results from the two vegetation indices since EVI is designed to minimize canopy-soil variations and have improved sensitivity where vegetation is more dense, and since it has also been used to study post-fire vegetation recovery (177; 72; 24). NDVI and EVI images that represent 16-day Maximum Value Composites at a resolution of 250 meters from 2000-2023 were spatially averaged by watershed area in Google Earth Engine. The resulting time series of spatially averaged NDVI and EVI were normalized according to Equation 3.3 by estimating $\mathrm{NDVI}^{*}(t)$ and $\mathrm{EVI}^{*}(t)$ as the mean monthly maximum values over the pre-fire period. Eleven missing values in years 2001 and 2002 were replaced with the long-term monthly mean NDVI/EVI values for the pre-fire period. Before curve fitting, we ensured the pre-fire NDVI/EVI time series were stable through time by conducting a Mann-Kendall test on the water-year averaged annual values and found that there was no monotonic trend with time. The fit of the exponential decay curves to the normalized, spatially averaged vegetation index time series, 95% confidence intervals, R^2, RMSE, and bulking factor curves resulting from the estimation of t_{r} are shown in Figure B.2.

Debris Basin Capacity

For Leach watershed, the debris basin capacity was estimated through analysis of a DEM produced from an unmanned aerial vehicle (UAV) photogrammetric survey of the debris basin conducted by Riverside County using ArcGIS (30). The capacity of the debris basin was increased in November 2018 before the first post-fire wet season began in anticipation of increased sediment fluxes, and since Riverside County conducted the photogrammetric survey just after this improvement was completed, it captured the debris basin in its empty, "design capacity" state. The DEM produced from the photogrammetric data had a resolution of 15 cm (0.5 ft) and an absolute vertical accuracy of <5-7 cm (0.16-0.23 ft) at the 95% confidence level, which includes the ground control point error (115). We manually removed non-ground features such as vegetation from the point cloud to produce a bare earth DEM, then used the Surface Volume tool in ArcGIS to estimate the volume of the empty debris basin. For McVicker watershed, the debris basin design capacity was estimated by Riverside County from a UAV photogrammetric survey they conducted in September 2018 before the wet season began with similar vertical accuracy.

Table 3.4: Model parameters used to estimate post-fire flood hazards for each study watershed.

Parameter Name	Units	Coldwater	McVicker	Leach
Watershed Area	km^2	10.9	5.86	3.86
Mean Watershed Slope (30-m DEM)	%	60.8	46.3	45.4
Length of Longest Flow Path	km	6.44	6.44	3.22
Watershed Relief	m	1,342	801	603
Runoff Response	unitless			
Frequency		3.36×10^{-5}	2.82×10^{-5}	3.08×10^{-5}
MAE		1.47×10^{-5}	1.47×10^{-5}	1.47×10^{-5}
NSE/RMSE		1.24×10^{-5}	1.24×10^{-5}	1.24×10^{-5}
Mean % Error		2.38×10^{-6}	2.38×10^{-6}	2.38×10^{-6}
Time to Peak	hours	5.58	6.02	5.73
Watershed Area Burned	%	98.0	99.4	99.96
Moderate Severity	%	57.6	89.0	89.0
High Severity	%	17.9	5.05	2.74
Wildfire Hydrologic Impact (Livingston et al., 2005)		Moderate	Moderate	Moderate
Post-fire Bulking Factor	unitless			
Lower Bound		1.001	1.03	1.04
Upper Bound		1.01	1.38	1.52
Recovery Timescale	days	1,103	726	737
Debris Basin Design Capacity	m^3	-	78,912	20,642
Flood Channel Design Capacity	m^3	-	52.5	10.0
Infrastructure Cleaning Threshold	% volume filled	-	85	85
Wet Season Cleaning Waiting Period	days	-	1	1
Wet Season Debris Basin Cleaning Rate	m^3/day	-	1,710	2,064

Flood Channel Capacity

We estimated flood channel capacities for both Leach and McVicker using PRIMo, a dual-grid flood inundation model, to determine the maximum flow rate the flood channels could convey without producing overbank flows (128). We used a DEM produced from an airborne Lidar survey conducted in September 2018 before the start of the wet season with a resolution of 0.46 m (1.5 ft) and vertical accuracy of 3.02 cm (0.099 ft, RMSE) to estimate the design capacities of the flood channels. After hydro-conditioning the DEM in ArcGIS to remove bridges and culverts, we forced PRIMo with a constant volumetric flow rate, a no-flow boundary condition at the edge of the domain upstream of the input point source, and a dry boundary condition at downstream end of the model domain. The input flow rates were increased or decreased iteratively until the channel overtopped, and the model was run until a steady state was reached for each simulation trial. Since the flood channel downstream of the Leach watershed is an unlined channel and that downstream of the McVicker watershed is a concrete-lined channel, we used Manning n values of 0.030 and 0.013, respectively, based on Chow (25). Additionally, the Leach flood channel had a brick wall along its southern bank that was not resolved by the DEM and needed to be enforced in the simulation to prevent unrealistic channel overtopping; the grid edge classification method developed by Kahl et al. (67) was used to implement a 1.5-m tall no-flow boundary to simulate this wall.

Infrastructure Cleaning Standards

The infrastructure maintenance model parameters include the infrastructure cleaning threshold, the wet season cleaning waiting period, and the wet season debris basin cleaning rate. The infrastructure cleaning threshold was set to when 85% of the debris basin or flood channel is filled based on discussions with Riverside County (116); this threshold applies to the cleaning of both the debris basin and the flood channel. The wet season cleaning waiting period and debris basin cleaning rate were estimated based on records of debris basin excavation volumes for Leach and McVicker debris basins from Riverside County for the 2018-19 wet season at a daily timescale. Daily excavation volumes for each debris basin were averaged over the wet season to obtain the cleaning rate, and waiting periods were roughly based on the number of days following a storm without rain that passed before sediment was excavated. Importantly, only the debris basins are cleaned during the wet season as well as the dry season according to conventional maintenance practices; channels are cleaned during the summer only (116).

3.1.4 Calibration Methods

We calibrated PF2HazMo to the first wet season following the Holy Fire, when streamflow and infrastructure overtopping data were available, to assess the performance of the modeling framework with respect to reproducing observed post-fire peak flows and infrastructure exceedances. Streamflow data was used to calibrate the runoff response parameter, c_t, based on its high sensitivity as will be revealed in the results.

For both the calibration and validation, a one-year simulation period was used spanning a wildfire event and post-fire wet season where rainfall, streamflow, and overtopping were observed. The simulation begins on 1 August 2018 and fire occurrence is simulated on 6 August 2018, the day the Holy Fire ignited. With each simulation, a post-fire bulking factor value is chosen uniformly at random from the estimated post-fire bulking range (Section 3.1.3), and thus the sediment yield properties of each simulation exponentially decay thereafter in accordance with vegetation recovery timescales estimated for each watershed. Observed daily rainfall totals from the rain gauge nearest each watershed are used to force the simulation, with 41 days of rainfall during the wet season depending on the rain gauge. The simulation ends on 31 March 2019, about ten days after the last day with observed rainfall. The parameter values used to apply the model to each study watershed are shown in Table 3.4.

Rainfall-Runoff Model Calibration

PF2HazMo predicts runoff from rainfall using a type of rational method as follows:

$$Q_{\mathrm{w}} = \frac{cPA}{t_{\mathrm{p}}} \tag{3.5}$$

where c is the runoff coefficient, Q_{w} is the clear-water discharge at the watershed outlet, P is the daily precipitation total, A is the area of the watershed, and t_{p} is the time to peak of a triangular hydrograph with equal rising and falling limbs.

Given the availability of precipitation and streamflow data, calibration targeted the ratio of the runoff coefficient to $c_t = c/t_{\mathrm{p}}$ (Gage Data Approach). Additionally, a second calibration strategy was developed targeting the availability of regional precipitation-frequency and discharge-frequency curves (Frequency Curve Approach). We developed both approaches because, in an ideal scenario, streamflow observations would be available for the watershed of interest to be used to calibrate c_t directly; however, many watersheds are too steep to install gauges, or post-fire bulked flows may be so forceful that they destroy monitoring equipment (115). Since precipitation and discharge frequency estimates are available for the majority of the continental United States and its territories from the National Oceanic and Atmospheric Administration (NOAA) and the USGS, respectively, PF2HazMo could potentially be applied broadly given the availability of a suitable calibration method for leveraging these data.

Applying the Gage Data Approach, we used observed post-fire streamflow data for the Coldwater watershed to calibrate c_t using multiple error metrics (objective functions) commonly used in hydrologic modeling. Observed peak flows were identified based on a visual analysis of the maximum daily discharge time series and an understanding of when the major storm events of the wet season occurred from discussions with Riverside County. Through manual calibration of the model, we determined the optimal value for c_t was within the range $(2 \times 10^{-6}, 4 \times 10^{-5})$. We then conducted an automated calibration process in which we ran the model for 100 linearly spaced candidate values within this range and calculated the corresponding Nash-Sutcliffe efficiency (NSE) index, the root mean squared error (RMSE), the mean absolute error (MAE), and the mean percent error (% Error) by comparing the observed peak flows to the median of the simulated peak flow distribution on the same days of the wet season. The equations for the error metrics are as follows:

$$\begin{aligned}
\text{NSE} &= 1 - \frac{\Sigma_{i=1}^{n} |y_i - x_i|^2}{\Sigma_{i=1}^{n} |x_i - \overline{x}|^2} && (3.6) \\
\text{RMSE} &= (\frac{1}{n} \Sigma_{i=1}^{n} |y_i - x_i|^2)^{1/2} && (3.7) \\
\text{MAE} &= \frac{\Sigma_{i=1}^{n} |y_i - x_i|}{n} && (3.8) \\
\%\text{Error} &= |\frac{y_i - x_i}{x_i}| \times 100 && (3.9) \\
& && (3.10)
\end{aligned}$$

where x represents observed peak flows, y represents simulated peak flows, n is the number of measured-predicted data pairs, and $\overline{x}$ is the mean of observed peak flows. We chose this suite of error metrics rather than a single objective function because they each have advantages and disadvantages. For example, mean error metrics such as MAE and mean % error are less affected by outliers than are squared error metrics, while relative change metrics (such as %

error) highlight errors in low flows more than in high flows (61). For each error metric, we can obtain an optimal parameter estimate by minimizing (in the case of RMSE, MAE and % error) or maximizing (in the case of NSE) the metric and then compare the outputs from the calibrated models to observations of peak flows and overtopping events. In summary, we can assess how different error metrics (objective functions) bias hazard estimation.

Applying the Frequency Curve Approach, which targets the estimation of c_t in an ungauged watershed, we obtained precipitation frequency estimate grids from NOAA Atlas 14, which represent spatially interpolated point precipitation frequency estimates from a national network of precipitation-reporting stations at a resolution of 30 arc-seconds (106). We retrieved annual maximum series for a 6-hour storm for California for return periods of 2, 5, 10, 25, 50, 100, 200, and 500 years. We chose a 6-hour duration to capture the relatively short-duration, high-intensity storms that commonly trigger hyperconcentrated and debris flows in the region (139). We then calculated the watershed area-averaged precipitation depth for each return period for the three study watersheds using ArcGIS and used these spatial averages as our precipitation frequency estimates. Discharge frequency estimates for the same return periods were obtained by applying the StreamStats online tool to each watershed individually (153). These discharge estimates are calculated using regional regression equations developed by fitting a log-Pearson Type III distribution to annual peak flow data through water year 2006 from a network of USGS streamgages in California with 10 or more years of data (44). The three study watersheds are located in the South Coast Region (Region 5) of the USGS regional regression analysis, which includes non-desert southern California. Once the precipitation and discharge frequency estimates for each return period were obtained, we estimated c_t through linear regression of $P \times A$ and Q_w, where c_t is the slope of the line with intercept forced to zero. In the following results sections, we refer to this parameter estimation method as the “Frequency” method.

3.1.5 Validation Methods

PF2HazMo was validated with applications to the Leach and McVicker catchments in Riverside County. Here, detailed monitoring was carried out by Riverside County Flood Control and Water Conservation District from November 2018 to April 2019, a period that immediately followed the Holy Fire. Overtopping events are documented from timelapse videography, and sediment volumes removed from the debris basin and channels are documented by drone surveys and sediment disposal contracts which include volumes of material transported away from the site. Infrastructure overtopping data are described in Section 3.1.1. Finally, as a check to ensure the model conserved sediment mass/volume, we compared the sediment influx, outflux, and storage change of the debris basins and found that the residual was comparable to numerical precision 10^{-11} (Figure B.4).

3.2 Results

3.2.1 Model Sensitivity and Error Analyses

Sensitivity Analysis

Figure 3.2 compares the sensitivity coefficients between model parameters for each model output variable. For some output variables, one model parameter is clearly more sensitive than the others, such as the cleaning waiting period, w, for the number of basin exceedances, or the post-fire bulking factor, k_1, for the number of channel exceedances. However, there are a number of parameters for which the sensitivity coefficient is greater than or equal to one for multiple model outputs, such as the runoff response, c_t.

To better understand which model parameters were consistently sensitive across output

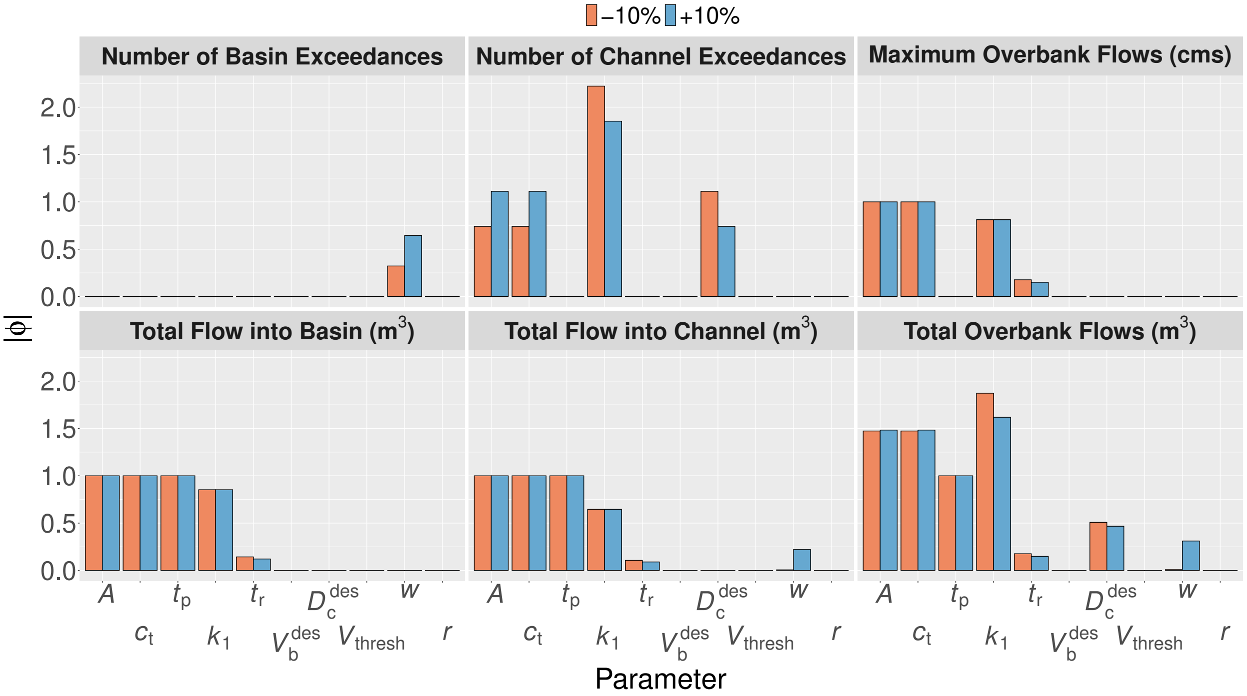

Figure 3.2: Absolute value of sensitivity coefficients, ϕ, for each model parameter and output variable resulting from a 10% increase or decrease in the parameter value from the mean/median.

.

Table 3.5: Ranking of model parameters based on greatest sensitivity coefficient across output variables.

Parameter	# Times Ranked in Top 3
Watershed Area	5
Runoff Response	4
Post-fire Bulking Factor	3
Time to Peak	2
Flood Channel Design Capacity	1
Debris Basin Design Capacity	1
Wet Season Cleaning Waiting Period	1

parameters, we ranked the parameters by sensitivity coefficient separately for each output variable and then counted the number of times each parameter ranked in the top three. The result of this overall sensitivity ranking is shown in Table 3.5. Watershed area was ranked in the top three most sensitive model parameters for five of the six output variables, while runoff response, post-fire bulking factor, and time to peak were also highly ranked for multiple output variables. Hence, the most sensitive model parameters are those which contribute to the peak (bulked) flow which drive the hazards.

Error Propagation Analysis

Correlation coefficients linking changes in model outputs to changes in model inputs were also used to rank the importance of input parameters. An overall ranking by squared correlation coefficient and squared partial correlation across all output variables is presented in Table 3.6. These results are similar to the sensitivity analysis, in that watershed area, runoff response and time to peak parameters all ranked highly. The post-fire bulking factor, flood channel design capacity, and we season cleaning waiting period also appear as important parameters relative to error propagation (relative to at least one model output variable).

Table 3.6: Ranking of model parameters based on greatest squared correlation and partial correlation coefficient across output variables.

Parameter	# Times Ranked in Top 3 by r^2	# Times Ranked in Top 3 by r_{p}^2
Watershed Area	6	6
Runoff Response	5	5
Time to Peak	4	4
Post-fire Bulking Factor	1	1
Flood Channel Design Capacity	1	1
Wet Season Cleaning Waiting Period	1	1

Based on the results from the sensitivity and error analyses, model calibration targeted the runoff response parameter c_t, the post-fire bulking factor was treated as a random variable (bounded by post-fire erosion estimates from HEC-HMS modeling, and all other parameters were estimated using the methods presented in Section 3.1.3.

3.2.2 Calibration to Observed Post-fire Peak Flows

Figure 3.3 compares observed peak bulked flows to the distribution of simulated peak bulked flow in the Coldwater catchment when c_t is calibrated in five different ways: the first four options rely on in-situ gage data and one of four different objective functions (Gage Data Approach), and the final option designed for ungaged basins relies on regional hazard data (Frequency Curve Approach). First, results show that calibrating PF2HazMo to regional hazard data leads to significantly higher peak bulked flows than suggested by local gage measurements, irrespective of the objective function used. The median of the peak flow distribution based on regional hazard data ("Frequency" in Figure 3.3) is almost four times greater than that of the observed peak flows for the 2018-19 wet season. The other simulated peak flow distributions were produced by calibrating the c_t parameter to the observed peak flows, each using a different error metric as the objective function for the parameter optimization. Using NSE and RMSE as the objective function resulted in the same peak flow distribution, since both are squared error metrics; hereafter we refer to the simulation results produced by using NSE or RMSE as the objective function as “RMSE” for simplicity. The medians of the peak flow distributions using MAE, NSE, and RMSE (as an objective function) all fall within the notch of the boxplot of the observed peak flows; since the width of the notch roughly represents a 95% confidence interval and the notches of the simulated and observed distributions overlap, this suggests that the medians are not significantly different. However, it is important to interpret the notch of the observed distribution with caution due to the small sample size of observed flows (n=4). The median of the peak flow distribution based on RMSE calibration is closest to that of the observed distribution in terms of percent error relative to the median of the observed distribution. Finally, the peak flow distribution when calibrated by % Error has the lowest median of all the simulated distributions, which is expected since % Error is a relative change metric and this type of error metric tends to emphasize errors in low flows. The MAE, NSE, RMSE, and % Error values corresponding to calibration with each of the five calibration methods are reported in Table B.1.

3.2.3 Validation with Observed Overtopping Events

Validation of the model is approached with applications to the Leach and McVicker catchments that adopt site-specific parameters for measurable properties (e.g., watershed area, debris basin capacity, flood channel capacity, infrastructure cleaning attributes), the calibrated value of c_t taken from the nearby Coldwater Creek catchment (Gage Data Approach) or calculated using regional hazard data (Frequency Curve Approach), and parameter ranges for other variables as described previously. Hence, PF2HazMo is validated with an application that relies only upon updates to readily observable physical properties. Moreover, validation is pursued with the four different calibrated values of c_t described in the pre-

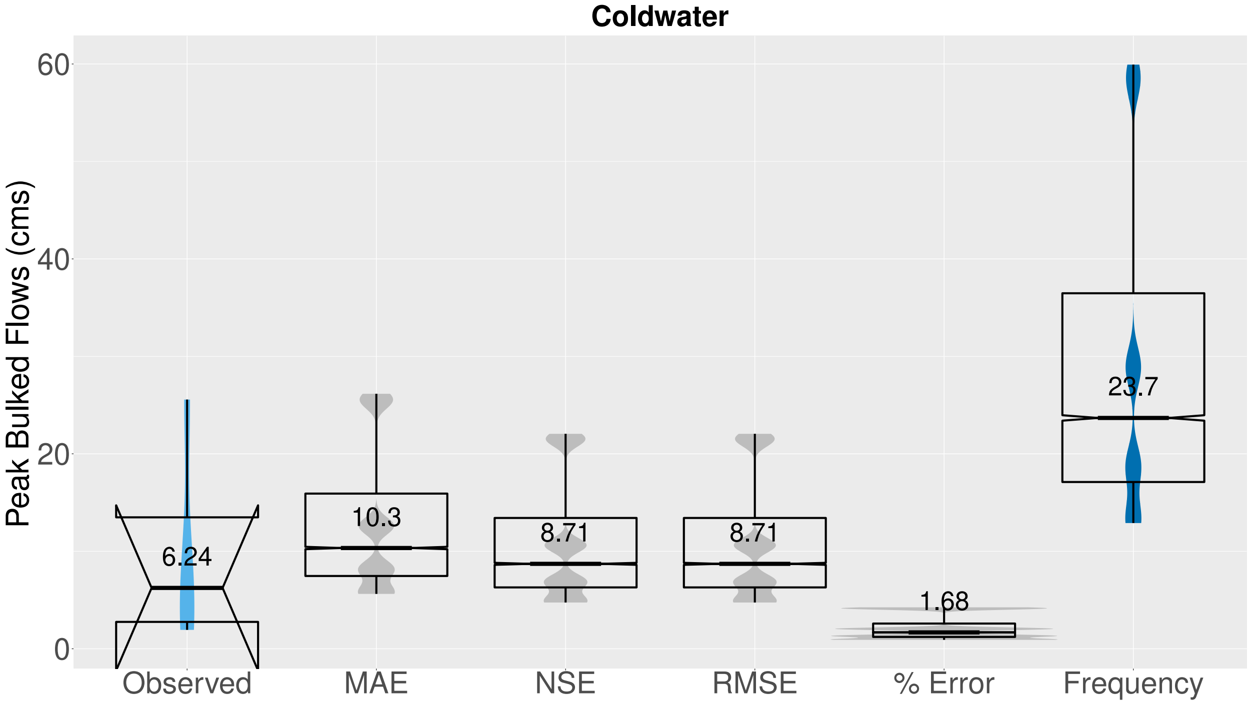

Figure 3.3: Observed (light blue), gage-data calibrated (grey), and frequency-curve calibrated (dark blue) peak bulked flow distributions for Coldwater watershed during 2018-19 wet season. Simulation results for different calibration methods are compared, where MAE/NSE/RMSE/% Error refer to the error metric used to calibrate c_t to observed peak flows and “Frequency” refers to estimating c_t using regional precipitation and discharge frequency estimates. Numbers indicate median values. Sample size for observed peak flows is n=4; sample size for each simulation trial is n=12,000.

.

vious section, and a comparison between the simulated distribution of exceedances and the observed number of exceedances is shown in Figure 3.4 for both channels and debris basins. Figure 3.4A shows that for Leach watershed, calibration using RMSE as the objective function produces the best fit between the median simulated and observed number of channel exceedances, though the simulated number of basin exceedances was overpredicted (median=17, observed=3). For McVicker watershed, all calibration methods correctly and precisely predicted zero channel exceedances, while the number of basin exceedances was overpredicted by roughly an order of magnitude for all but the % Error calibration method, which predicted zero basin exceedances (observed=1, Figure 3.4B). Across watersheds and infrastructure types, the Frequency calibration method resulted in a higher number of exceedances than observed (by a factor of ~8-28), while calibrating the model to observed post-fire flows produced similar results for the MAE, NSE, and RMSE objective functions, with the % Error objective function tending to underpredict either the number of channel or basin exceedances.

To understand how well the model captures the interacting dynamics of storms, bulking factors, and infrastructure capacity on days when infrastructure overtopping events were actually observed, Figure 3.5 presents the percentage of simulation runs that predicted overtopping for each day of the wet season, with observed overtopping days shaded in blue. The percentage of simulations predicting overtopping can be thought of as the level of agreement between stochastic simulation trials; a high percentage of simulations predicting overtopping on a specific day, even when the post-fire bulking factor was sampled randomly for each simulation, can be thought of as solution "convergence" in a probabilistic sense. For the Leach flood channel, the observed exceedance on 14 February 2019 was predicted by >89% of simulation runs for the Frequency, MAE, and RMSE calibration methods (Figure 3.5A). Notably, the % Error calibration method did not result in any simulations predicting channel overtopping throughout the entire wet season. For the Leach debris basin, all three observed exceedances were predicted by >50% of simulation runs for the Frequency

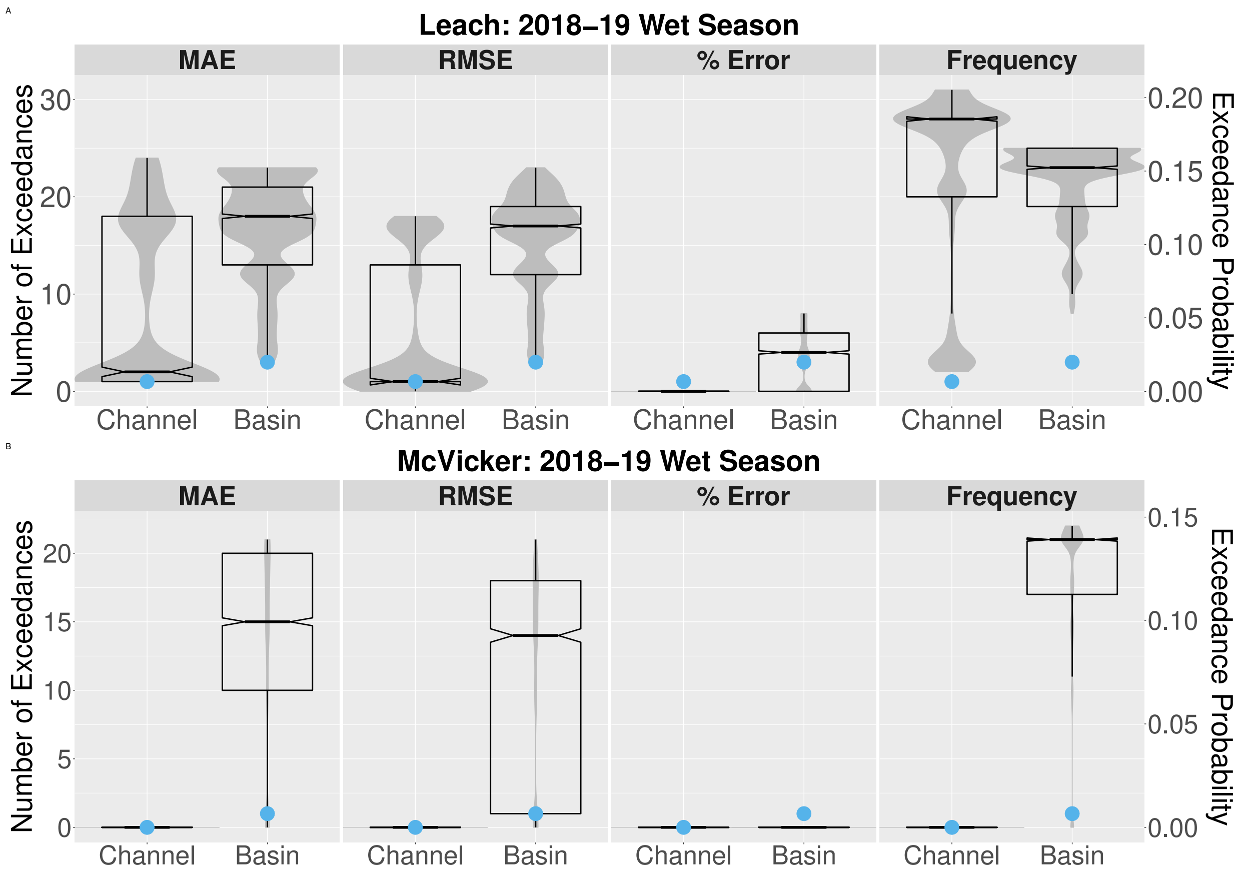

Figure 3.4: Simulated number of flood channel and debris basin exceedances for each calibration method (grey distributions) with observed number of exceedances shown as blue points for (A) Leach watershed and (B) McVicker watershed. Exceedance probability refers to the daily infrastructure exceedance probability during a given wet season, defined from November 1st to March 31st.

.

calibration method (Figure 3.5B). However, for the MAE and RMSE calibration methods a majority of simulation trials did not predict the basin exceedance on 6 December 2018. The reason for this is that the percentage of simulation runs that predicted the Leach debris basin had filled to capacity by 6 December 2018 was only 20% for MAE and 5% for RMSE (data not shown). The debris basin cannot overtop until it has filled to capacity, so if the estimated peak flows or bulking factor are lower than what was observed for early-season storms, the debris basin will not fill as quickly as it did in reality. Another example that emphasizes the importance of the timing of infrastructure filling versus the timing of precipitation is the three days following the Leach debris basin overtopping event on 14 February 2019: 100% of simulations predict overtopping for the Frequency, MAE, and RMSE calibration methods on those days. The reason is that the basin was predicted to have filled completely by that date and rain continued to fall the following three days, thus preventing wet season cleaning (waiting period = 1 day) and resulting in additional basin overtopping events. It is possible that additional basin overtopping events were observed in the days following the 14 February 2019 event, but no timelapse video for this period was provided to us by Riverside County, presumably because the largest and most interesting impacts on the infrastructure had subsided by that point. The % Error calibration method resulted in <25% of simulations predicting overtopping for Leach debris basin for any of the dates on which overtopping was observed.

For the McVicker debris basin, the Frequency, MAE, and RMSE calibration methods each resulted in >50% of simulations predicting overtopping on 14 February 2019, when basin overtopping was observed (Figure 3.5C). The % Error calibration method did not result in any simulations predicting basin overtopping throughout the entire wet season. Overall, the Frequency calibration method most consistently produced a high level of agreement between simulation trials that infrastructure overtopping would occur on days when it was observed. This result is likely due to the higher estimated c_t value produced by the Frequency method, which results in greater peak clear-water flows and thus greater sediment fluxes from the watershed (Table 3.4). Indeed, Figure 3.5 shows that the percentage of simulations predicting overtopping roughly scales with the estimated value of c_t for each calibration method (Frequency > MAE > RMSE > % Error).

3.2.4 Long-Term Compound Hazard Predictions with Calibrated Model

Following calibration and validation, PF2HazMo offers a platform to study future changes in risks from factors such as changes in wildfire frequency and intensity, changes in precipitation and changes in infrastructure design and maintenance. As an illustration, we used PF2HazMo to simulate the number of channel exceedances over 100 years for Leach and McVicker watersheds under both a "present fire regime" scenario and a "future fire regime" scenario in which the fire frequency is increased. We used the model parameters in Table 3.4, selecting the NSE/RMSE estimate for the c_t parameter since it resulted in the best overall fit between simulated and observed peak bulked flows, number of infrastructure exceedances, and timing of overtopping events (Sections 3.2.2-3.2.3). The present fire regime scenario was defined by a mean fire recurrence interval of 40 years, which represents the average period between wildfires under the presumed historical fire regime, spatially averaged across the area of the study watersheds (78). The future fire regime, characterized by a fire recurrence interval of 20 years, was based on a projection from California's Fourth Climate Change Assessment that under a high emissions scenario (Representative Concentration Pathway 8.5) by 2100, the frequency of large fires would increase by nearly 50 percent (8). The 100-year precipitation time series used to force the model was stochastically generated using the MCMC rainfall simulator described in Jong-Levinger et al. (66).

A comparison of the number of channel exceedances per century under present and future fire regimes for Leach watershed is shown in Figure 3.6. The Leach flood channel has a design

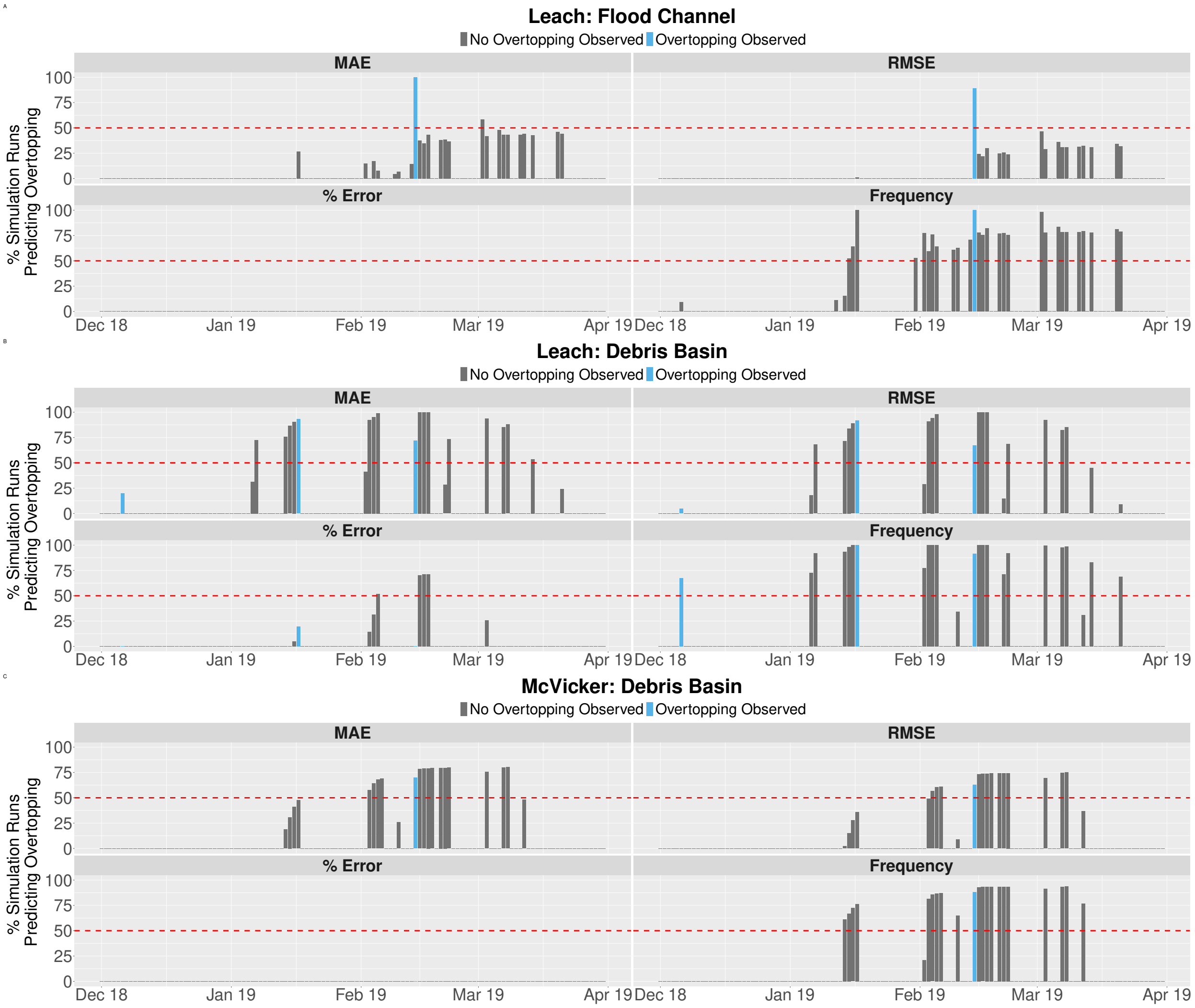

Figure 3.5: Percent of simulation runs (n=3,000) that predicted overtopping on each day of the wet season for (A) Leach flood channel, (B) Leach debris basin, and (C) McVicker debris basin. Blue shading indicates days when overtopping was observed; height of bar represents percentage of runs that predicted overtopping. Red dashed line represents 50%.

capacity capable of conveying a roughly 50-year flood based on the discharge-frequency curve for the watershed; this means that the median number of floods per century under present conditions estimated by PF2HazMo, five, represents three more exceedances than would be expected by ignoring post-fire sediment fluxes and their impact on infrastructure clogging. Under future conditions, PFHazMo estimates a median of seven channel exceedances per century, or a roughly 14-year flood return period. To put these flood frequencies into perspective, we define a "hazard amplification factor",

$$A_F = T_{\mathrm{p}}/T_{\mathrm{c}} = p_{\mathrm{c}}/p_{\mathrm{p}} \tag{3.11}$$

which represents a ratio of the return period of channel exceedances for the marginal hazard (precipitation in the absence of wildfire) to that of the compound hazard (considering both wildfire and precipitation as hazard drivers). The amplification factor for Leach watershed under the present fire regime is 2.5, while that under the future fire regime is 3.6, highlighting the importance of considering the probability of post-fire bulked flows when designing flood infrastructure. Lastly, turning attention to the shape of the distributions in Figure 3.6, the tails are quite long and narrow, especially for the present hazards distribution, indicating it is possible that much greater flood frequencies than the median could be observed, though the probability is small. Notably, the density of the present distribution is more concentrated about its minimum value of five than is the future distribution, indicating a future shift towards a greater likelihood of increased flood frequencies.

In contrast to the hazard estimates for Leach watershed, for McVicker watershed, zero floods per century were predicted for both the present and future fire regime scenarios. The design flood channel capacity for McVicker watershed that we estimated using 2D flood inundation modeling is 52.5 cms (1,854 cfs). Based on the discharge-frequency curve for this watershed (153), the capacity of the flood channel is greater than even the magnitude of a 500-year

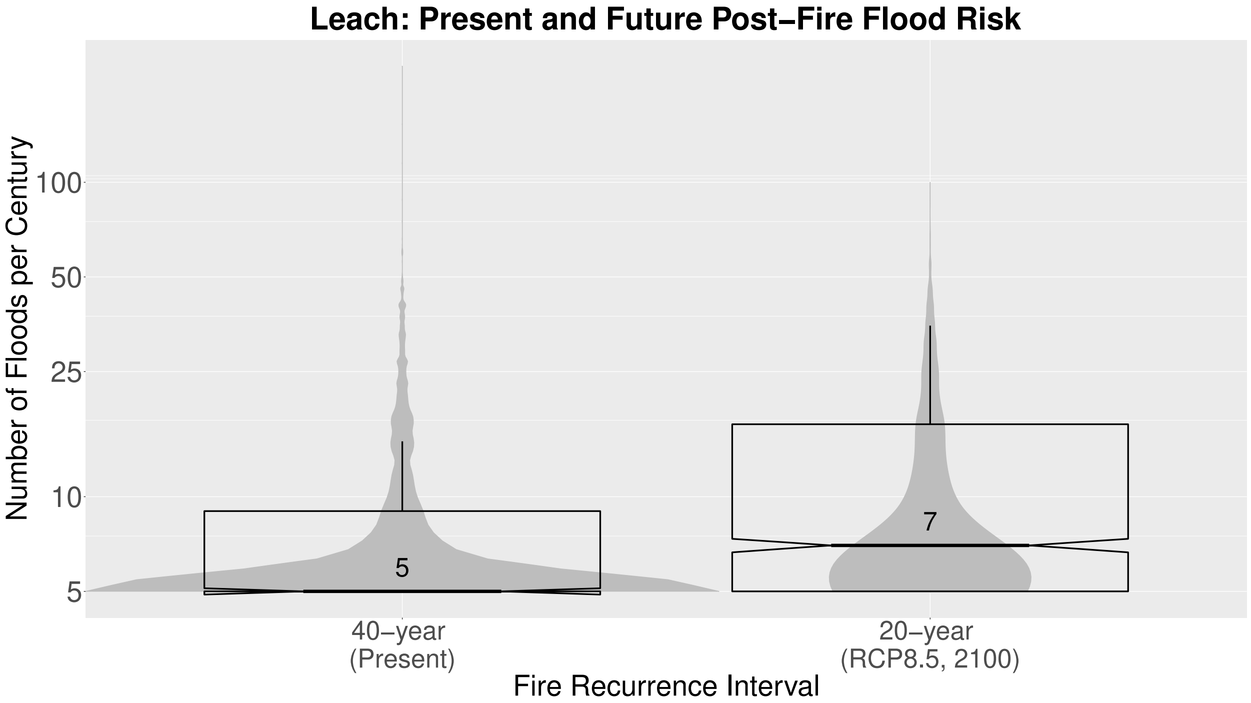

Figure 3.6: Estimated number of flood channel overtopping events per century under historical (40-year) and projected future (20-year) fire recurrence intervals for Leach watershed. Numbers indicate median values. Simulation results for McVicker watershed estimated zero flood channel overtopping events for both scenarios. Y-axis was log transformed.

.

flood (30.9 cms or 1,090 cfs). Thus, in this case the concrete-lined flood channel provides a level of protection against floods that can handle the projected compound flood hazards under the future fire regime.

3.3 Discussion

3.3.1 Model Applications

The preceding results indicate that different calibration methods are suited to different project goals. For example, the Frequency calibration method appears to work better for simulating higher magnitude peak flow events with longer return periods. To this point, comparing the discharge-frequency curves produced from HEC-HMS simulations to the discharge frequency estimates from StreamStats used to calibrate them reveals a better fit for events with a 25-year return period or longer (Figure B.3). Thus, the Frequency method may be best suited for applications for which more conservative peak flow estimates over longer time horizons are needed, such as the design of debris basins or flood channels downstream of watersheds that burn frequently or are know to produce high sediment yields. This calibration method may also be the best option available if the watershed of interest is ungauged and no nearby streamflow records exist.

On the other hand, if sufficient streamflow records are available, we have demonstrated that PF2HazMo can be calibrated based on these observations and an appropriate range for the post-fire bulking factor to accurately simulate channel exceedances. During the critical period just after a wildfire yet before the start of the wet season, the simulation framework can be used to forecast the number of infrastructure exceedances over the course of the wet season to direct resources to infrastructure maintenance and capacity enhancement efforts or identify infrastructure systems with low levels of protection for emergency planning purposes. By calibrating a HEC-HMS model to pre-fire streamflow using the curve number parameter and subsequently updating the curve number and lag time with satellite-derived burn severity data following Livingston et al. (84), a range of bulking factors that reflects the burned watershed can be estimated. Since the lumped model and curve number approaches are relatively simple to implement and the required data is readily available (from public land cover, soil property, and topographic databases), the bulking factor range can be estimated for a given watershed within a matter of days. This post-fire bulking range is then randomly sampled from to quantify the uncertainty regarding post-fire infrastructure exceedance probabilities and provide flood risk managers with a range of potential infrastructure exceedances and bulked flows to plan around. Based on the results presented in Section 3.2.2, we recommend using NSE/RMSE or MAE as the objective function for calibrating the c_t parameter, as % error produces estimates that underpredict exceedances.

3.3.2 Comparison to Other Studies of Post-fire Streamflow and Erosion

By conducting sensitivity and error analyses we identified that the model parameters that have the greatest influence on model response are the runoff response, c_t, the post-fire bulking factor, k_1, the time to peak, t_{p}, and the flood channel design capacity, $D_{\mathrm{c}}^{\mathrm{des}}$. The runoff coefficient and time to peak parameters represent the influence of land cover and precipitation intensity/storm duration on peak flows, while the post-fire bulking factor and its decay over time implicitly are estimated using data on watershed morphology (e.g., slope, relief, length of longest flowpath), the time since the most recent fire, watershed area burned at moderate to high severity, and soil properties–factors that have all been identified as important drivers of post-fire hydrologic response (39; 40; 69; 73; 131; 171; 105; 164). Our analysis both underscores the importance of these variables and calls attention to the influence of the capacity of the flood channel downstream of the burned watershed on post-fire flood hazards.

Calibrating the model to observed post-fire peak flows produced a range of simulated peak flows that ranged from ∼1-60 cms with median estimates that differed based on the calibration method and objective function used. The observed peak flows (median=6.24 cms) for Coldwater watershed had a return period of less than 25 years based on its discharge-frequency curve (Figure B.3), but estimates from the California Geological Survey for the peak flow during the 6 December 2018 storm were 34 (±17) cms, which is roughly a 50-year event (personal communication). These estimates represent the clear-water equivalent flows needed to generate observed peak flow conditions observed in the field and were developed through either direct measurement of flow velocity and cross-sectional area or slope-area back-calculation using the Manning Equation and the broad-crested weir formula. The California Geological Survey estimates are much better aligned with the simulated distribution of peak flows produced using the Frequency method than with the streamgage data for Coldwater watershed (Figure 3.3). Additionally, Wilder et al. (2020) simulated post-fire streamflow for watersheds burned by the Holy Fire in the Santa Ana Mountains, including Coldwater, using a five-parameter Random Forest model; their estimates for the 13 watersheds in that region were on the same order of magnitude as our estimates using the Frequency method and the California Geological Survey's estimates. While it is possible that the streamgage used in this study had a negative bias, after calibrating PF2HazMo to the observed streamflow the number of overtopping events was accurately predicted, with most simulations overpredicting the number of basin overtopping events. This discrepancy between measured and estimated post-fire peak flows highlights the need for more post-fire streamflow gauge data.

3.3.3 Model Limitations

The methods for estimating model parameters and the stochastic hazard framework described herein will not perform well in all applications. The post-fire bulking factor range estimated for Coldwater watershed was 1.001-1.01, which is essentially no different than the baseline bulking factor value (Table 3.4). While the bulking factors estimated for McVicker and Leach included those representative of hyperconcentrated flow, those estimated for Coldwater did not; one potential reason for this is that the drainage area for Coldwater was large enough to fall into a different area class than that of McVicker and Leach, resulting in the use of LA Debris Method Equation 2 within HEC-HMS to estimate sediment loads. LA Debris Method Equation 2 weights drainage area much less than does LA Debris Method Equation 1, used to estimate sediment loads for McVicker and Leach, and since the drainage area for Coldwater was on the lower end of the range of areas for which the regression equation was developed (11 km^2 versus 7.8-26 km^2), this could have led to an underestimate in the post-fire bulking factor range. Previous studies of post-fire sediment yields find that unit-area sediment yields decrease as drainage area increases, so this result could be due to the larger watershed area of Coldwater than Leach or McVicker (164; 40; 105).

We tested other erosion models implemented in HEC-HMS including the USGS Emergency Assessment and Long-Term Debris Models, but these also resulted in bulking factors close to 1. Another possibility was that Coldwater watershed simply did not experience much erosion during the first wet season following the Holy Fire: this idea is supported by an estimate from the California Geological Survey that sediment concentrations in runoff from Coldwater were roughly 5-10% based on an analysis of runoff images from a storm event on 29 November 2018 and field observations following the storm (22). The lower threshold for hyperconcentrated flow is often considered to be a sediment concentration of 20%, so while these estimates are greater than the estimates we produce using the LA Debris Method Equations in HEC-HMS, they are still typical of normal streamflow. Post-fire erosion estimates produced from the differencing of DEMs derived from airborne Lidar show that among ten other watersheds burned by the Holy Fire, Coldwater produced relatively low estimates; however, McVicker produced similarly low erosion levels and yet we estimated significantly higher bulking factors for McVicker watershed (47). Without sediment concentration data it is difficult to know whether the low bulking factor range estimated for Coldwater was realistic, but modelers interested in post-fire erosion modeling with HEC-HMS should note that lower bulking factor estimates for larger watersheds are possible.

The present study was limited in scope to the first wet season following fire due to the lack of a longer dataset. While the range of post-fire bulking factors in this study was based on data from the first wet season following the fire, actual sediment concentrations will vary based on the intensity of subsequent precipitation events and the recovery of vegetation, which is dependent on climatic factors such as drought (170). Since the hazard estimates are based on the wet season immediately following the fire and since we assumed an A-T factor of 1 for the LA Debris Method (representative of the San Gabriel Mountains, which tend to produce higher sediment yields than do the Santa Ana Mountains), they can be considered a "worst case scenario" estimate of post-fire flood hazards. Evaluation of model predictions against longer post-fire streamflow and infrastructure overtopping time series is needed to better assess how the model performs after the first post-fire wet season for the first few years after the fire.

Finally, we note that the impact of short-duration, high-intensity rainfall on peak bulked flows is not resolved well by the model due to the use of a daily timestep. We aimed to partly address this by using a 6-hour storm when selecting the precipitation frequency estimates used to calibrate the c_t parameter using the Frequency method, but we acknowledge this is an indirect way of incorporating the impact of high-intensity precipitation. Short-duration, high-intensity rainfall has been shown to be important for generating post-fire debris flows and hyperconcentrated flows as well as generating watershed-scale erosion (68; 69; 164; 139; 140). Additionally, we note that "future" projections of post-fire floods are forced with a daily rainfall time series that has the statistical properties of the long-term precipitation gauge record it was parameterized with and does not reflect non-stationary trends such as an increased frequency of high-intensity events (see Jong-Levinger et al. (66)). Increased temporal resolution to resolve the effects of high-intensity storm events as well as a modified precipitation probability distribution that reflects the projected effects of climate change on the regional precipitation regime are features of the stochastic modeling framework that are being considered for future work.

3.4 Conclusion

PF2HazMo is a stochastic hazard estimation framework that can be calibrated and parameterized with readily available data to estimate post-fire bulked flows and flood infrastructure overtopping events over single wet season to multi-year timescales. An appropriate calibration method should be chosen based on the objective of the modeling effort; then reasonable estimates of bulked flows and infrastructure can be used to inform infrastructure design/maintenance approaches, emergency planning strategies, and risk communication efforts. Additionally, the model may be applied to multiple watersheds across a region to quickly obtain a first-order estimate of the spatial distribution of post-fire flood risk and inform flood management strategies via stakeholder engagement.

Chapter 4

Flood Hazard Amplification by Wildfires

This chapter is based on the following published work:

Jong-Levinger, A., Banerjee, T., Houston, D., & Sanders, B. F. (2022). Compound Post-Fire Flood Hazards Considering Infrastructure Sedimentation. *Earth's Future*, 10(8), e2022EF002670. `https://doi.org/10.1029/2022EF002670`

which was highlighted in *Nature Climate Change*,

Franke, J. (2022). Combined force of fire and water. *Nature Climate Change*, 12(9), 778-778. `https://www.nature.com/articles/s41558-022-01472-9`

4.1 Introduction

PF2HazMo is an original model for estimating compound, post-fire, sediment-laden flood hazards, and is uniquely poised to improve understanding about changes in flood risks resulting from changes in wildfire frequency and intensity. Hence, this chapter presents an examination of flood hazard amplification by wildfires, with hazard amplification defined as the ratio of future/present exceedance probability.

The ability to characterize hazard amplification is important not only for improving the design of infrastructure and promoting infrastructure maintenance, but also for increasing risk awareness within affected communities (95; 27; 54). Moreover, improved understanding of exceedance probabilities can be paired with 2D simulations of extreme events for more effective risk communication (85; 129). Two specific questions about post-fire flood hazards will be addressed herein:

1. How does the frequency of channel exceedances vary in areas exposed to post-fire compound flood hazards based on current design standards and maintenance approaches?
2. How will the frequency of channel exceedances change in the future based on increasing fire frequency and fire severity?

The remainder of the chapter is organized as follows: Section 4.2 (Methods) presents the simulation scenarios and model outputs generated to address the preceding questions. Section 4.3 (Results) shows the estimation of hazards for a range of fire frequencies and severities, infrastructure design standards, and maintenance approaches. Section 4.4 (Discussion) contrasts the exceedance probabilities of channels due to the compound hazard versus those of the precipitation used for design due to the marginal hazard, and contemplates the implications for risk management. Section 4.5 presents conclusions.

4.2 Methods

4.2.1 Hazard Simulations

Results are organized into two sets of simulation scenarios: Model Illustration Scenarios and Stochastic Hazard Scenarios. The Model Illustration Scenarios demonstrate how the framework estimates compound post-fire flood hazards under three infrastructure management scenarios using 100-year stochastic simulations that account for the combined effects of wildfires, rainfall, infrastructure design and maintenance. The Stochastic Hazard Scenarios consist of four sets of scenarios used to systematically investigate post-fire flood hazards in relation to four separate factors: infrastructure design standard, infrastructure maintenance approach, fire interval, and fire severity. The model settings for each simulation scenario are shown in Table 4.1.

The model parameters that were not varied within a given simulation scenario were kept constant between the different scenarios to ensure a fair comparison. The baseline parameter values used in this study were chosen to simulate a representative watershed system and flood infrastructure system in southern California and are displayed in Table 4.2. The same synthetic precipitation time series was used in each simulation (displayed in Figure 4.1a) for consistency across results.

4.2.2 Model Outputs

For each scenario, a total of 3,000 MC trials were simulated, each trial yielding a 100-year daily time series of peak channel flows and channel capacities from which the number of years per century with at least one channel exceedance, n_c, was computed. The annual exceedance

Table 4.1: Simulation scenarios.

	Scenario Name	Model Settings*	Model Output	Figure
Model Illustration Scenarios	Scenario 1: Low Protection	50C, S	Overbank flows (m^3/s)	4.1
	Scenario 2: Moderate Protection	50B, S		
	Scenario 3: High Protection	50B, SAW1		
Stochastic Hazard Scenarios	Design Standards and Fire Interval	50C, 100C, 50B, 100B 50, 20, 15, 10, 5, 2 (years)	Empirical flood return period (years)	4.2
	Maintenance Approach and Fire Interval	S, SA, SAW7, SAW1 50, 20, 15, 10, 5, 2 (years)	1. Empirical flood return period (years) 2. Sediment excavated from infrastructure (m^3)	4.3 4.4
	Design Standards and Burn Severity	50C, 100C, 50B, 100B $1.10 < k_1 < 1.25$, $1.25 < k_1 < 1.67$, $1.67 < k_1 < 2.86$	Empirical flood return period (years)	4.5
	Maintenance Approach and Burn Severity	S, SA, SAW7, SAW1 $1.10 < k_1 < 1.25$, $1.25 < k_1 < 1.67$, $1.67 < k_1 < 2.86$	Empirical flood return period (years)	4.6

*Abbreviations are defined in Sections 2.2, 2.4, and 2.5.

Table 4.2: Baseline model parameters.

Variable/Parameter	Value	Rationale
Watershed Area, A	3 km^2	Average area of watershed in southern California (39)
Pre-fire bulking factor, k_0	1.00	Corresponds to clear streamflow
Post-fire bulking factor, k_1	1.25-2.86	Represents a range of flow types from hyperconcentrated flow to debris flows
Fire Interval	20 years	Roughly representative of southern California (151)
Design Standard	50B	Represents standard used by Los Angeles County, which has set precedents in the estimation of design bulking factors for the region (48)
Design bulking factor, k_{des}	1.20	Based on past studies by the Ventura County Watershed Protection District (159)
Maintenance Approach	S	A commonly used approach in southern California (116)
Infrastructure cleaning threshold	85% filled	Based on correspondence with Riverside County (116)
Debris basin cleaning rate	1,800 m^3/day	Based on debris basin excavation records provided by Riverside County
Watershed recovery timescale, T_{r}	365 days	Assumes recovery time of 5 years following debris flow event (79)
Runoff coefficient, c	0.3	Used to calculate Q_{w}; based on commonly used values for natural land use types with >6% slope

probability, p_c, was computed for each MC trial empirically as follows,

$$p_\mathrm{c} = n_\mathrm{c}/100 \tag{4.1}$$

and a flood return period, T_c, follows as,

$$T_\mathrm{c} = 1/p_\mathrm{c} \quad \text{for} \quad p_\mathrm{c} > 0 \tag{4.2}$$

The progression of MC trials yields distributions of T_c values that are examined to infer dependencies on infrastructure design standards, infrastructure maintenance approaches, fire interval, and wildfire severity. Distributions are presented by combining box plots and violin plots. Box plots are displayed as follows: widths are proportional to the square-root of the sample size for each scenario; the central line corresponds to the median and the lower and upper edges correspond to the first and third quartiles, respectively; the upper whisker is calculated as min(max(x), Q3 + 1.5 × IQR); the lower whisker is calculated as max(min(x), Q1 - 1.5 × IQR); and outliers are not displayed. For the violin plots, Gaussian kernel smoothing was used.

We note that a “No Fires” scenario was also considered as a check on numerical consistency. In the absence of wildfire, the compound hazard reverts to the marginal hazard scenario (precipitation and runoff in the absence of wildfire), and the channel return period matches the precipitation return period, $T_\mathrm{c} = T_\mathrm{p}$. In all cases, the computed median value of T_c from 3,000 MC simulations was found to match the return period (either 50- or 100- year) of the precipitation return level used for runoff modeling, peak discharge estimation (Eq. 2.1), and sizing of channels according to the clear-water design standard.

4.3 Results

4.3.1 Illustration of Compound Post-Fire Flood Hazard Estimation

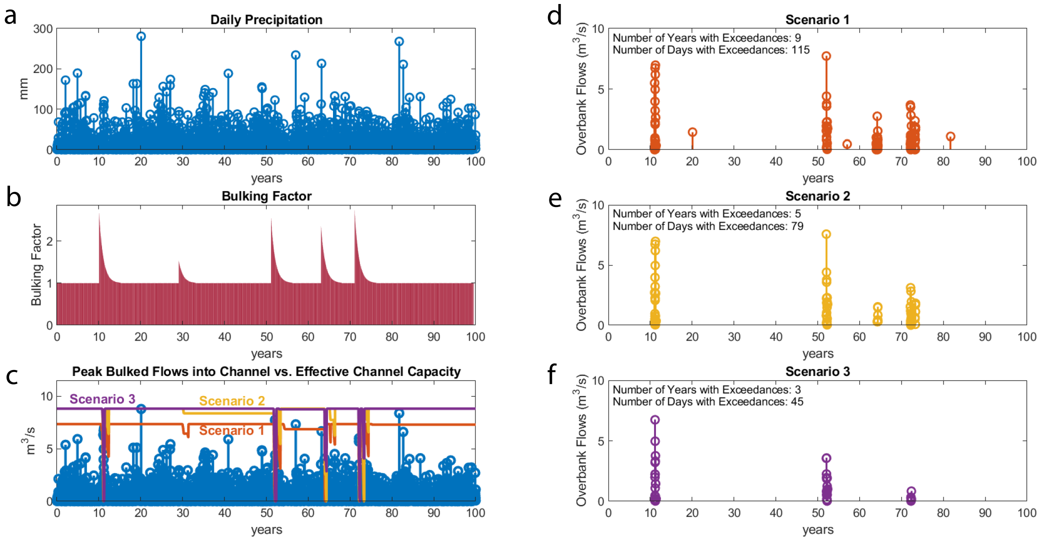

Figure 4.1: Time series of (a) daily precipitation, (b) bulking factor, (c) peak bulked flows from the debris basin into the channel and (d,e,f) the corresponding time series of overbank flood flows for three management scenarios. Management scenarios are defined in Table 4.1. The effective flood channel capacity time series for the three scenarios are compared in panel (c).

.

The simulation begins with 100-year stochastic time series of daily precipitation (Fig. 4.1a), the bulking factor (Fig. 4.1b), and daily peak bulked flows into flood channels (Fig. 4.1c, blue stem plot). Note that the simulation includes five fire events with different peak bulking factors, which correspond to random numbers, and that the bulking factor exponentially decays back to a baseline value of unity for several years after each fire event. The filling of infrastructure with sediment is sensitive to the management scenario (Scenario 1, 2 or 3), which in turn impacts the capacity of the flood channel (Fig. 4.1c, orange, yellow and purple lines, respectively) and the number of days when peak bulked flows exceed channel capacity (Fig. 4.1d, e and f, respectively).

Hazards can be estimated based on the number of years or days with exceedances of the channel capacity. Figures 4.1d, e and f show that with increasingly conservative flood management approaches (Scenario 1, 2 and 3, respectively), the number of years with exceedances of channel capacity is reduced (9, 5, and 3 out of 100) and the number of days with exceedances is reduced (115, 79 and 45 over 100 years).

An important dynamic captured by the simulation framework is the coincidence of high bulking factors and high peak precipitation, which leads to high peak bulked flows. For example, following a fire event in Year 10 that yields a bulking factor exceeding 2.0, overtopping events are predicted across all three management scenarios with rainfall less than 150 mm/day; on the other hand, rainfall of nearly 300 mm/day in Year 20 only yields a small rate of overtopping in Scenario 1, while no flooding is predicted under Scenarios 2 and 3.

4.3.2 Flood and debris hazards vs. fire interval

Figure 4.2 shows T_c distributions across four different *infrastructure design standards* (50C, 100C, 50B, and 100B) and six different *fire intervals* (50-yr, 20-yr, 15-yr, 10-yr, 5-yr and 2-yr). Return period is expected to decrease below that of the precipitation design level (50 or 100 years) with wildfires that alter runoff and sediment production, and Figure 4.2 shows the rates of decrease with decreasing fire intervals. Notably, median flood return period was computed to be 2 to 10.5 times smaller than expected based on a 50-year design standard and 3 to 16 times smaller than expected based on a 100-year design standard. For example, infrastructure designed based on a 50-year design storm assuming clear-water discharge (50C) delivers protection corresponding only to a 10-year return period when the fire interval is 10 years. Further, infrastructure designs that take a more conservative approach, such as a 100-year design storm assuming a bulked discharge (100B), only offer protection corresponding to a 20-year return period when the fire interval is 10 years. The most conservative design

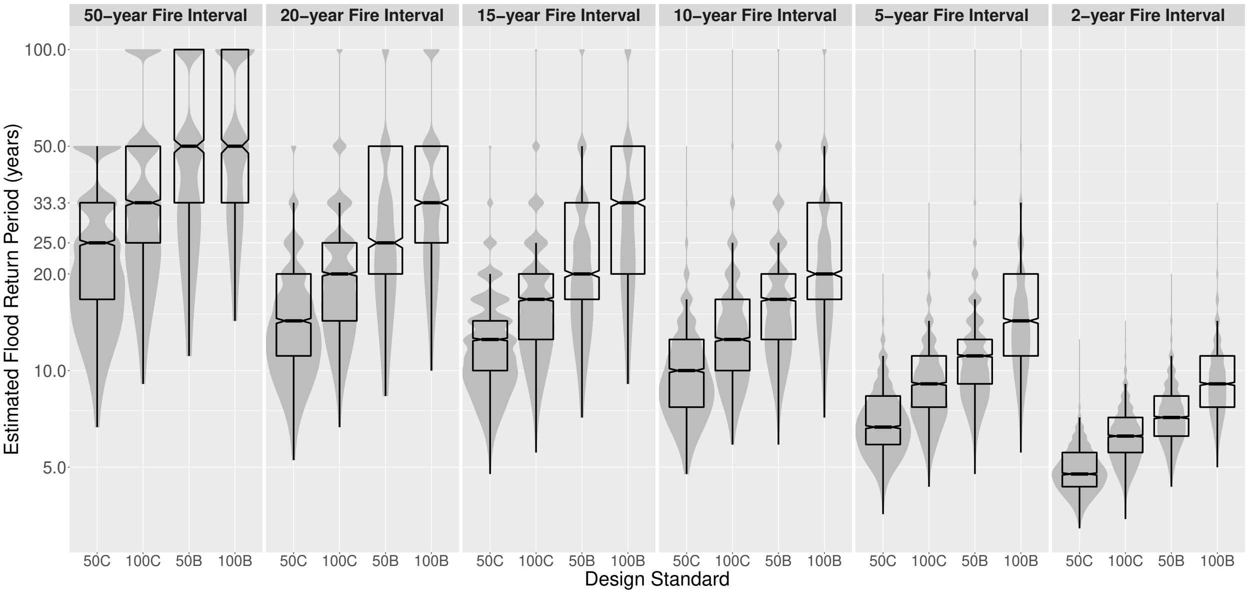

Figure 4.2: Simulated distributions of flood return period versus infrastructure design standard (50C, 50B, 100C, 100B) and fire interval.

scenario (100B) produces a median flood return period that is 1.8 times larger than that of the least conservative design scenario (50C), across all fire frequencies.

Figure 4.3 shows T_c distributions across four different *maintenance approaches* (S, SA, SAW7, and SAW1) based on the same fire intervals as before and infrastructure designed based on a 50-year storm and a bulked discharge (50B). The comparison of the flood return period distributions shows that differing maintenance approaches play a major role in moderating risks. For example, the most conservative maintenance scenario (SAW1) produces a median flood return period that is twice as large as that of the least conservative maintenance scenario (S).

Sediment management costs tend to vary based on a number of factors such as sediment size distribution, presence of contaminants, challenges with access, level of moisture, and access to a disposal site (10), but a controlling consideration is the volume of material that needs to be removed.

Figure 4.4 shows the total volume of sediment excavated from debris basins (Fig. 4.4a) and

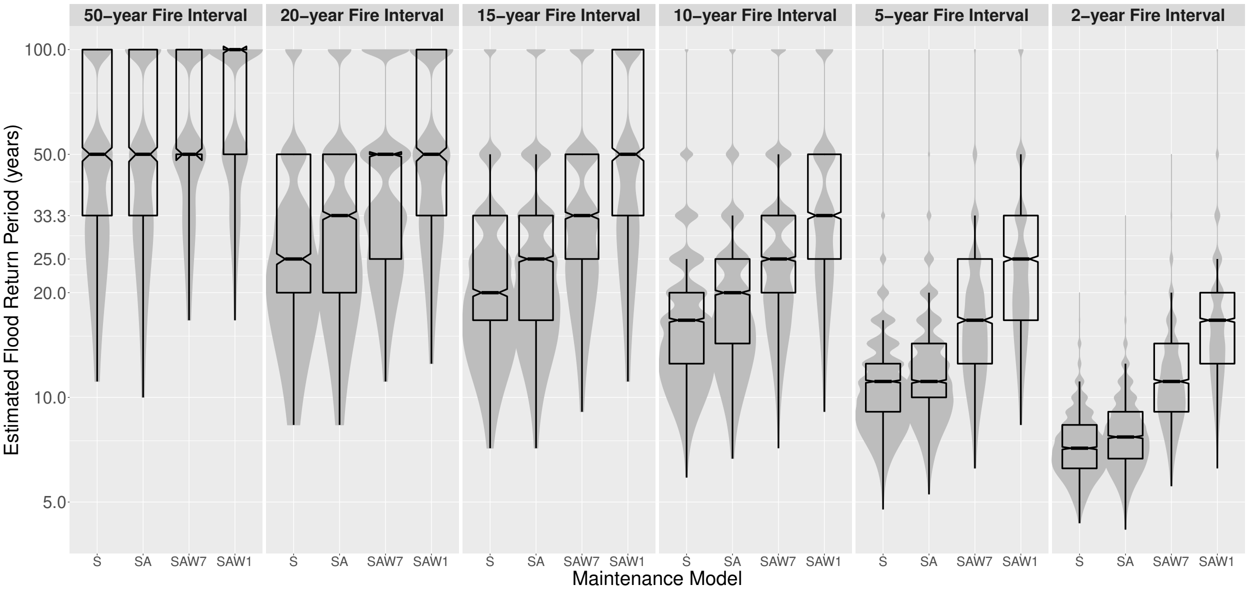

Figure 4.3: Simulated distributions of flood return period versus infrastructure maintenance approach (S, SA, SAW, SA1) and fire interval.

.

flood channels (Fig. 4.4b) per century under the each of the maintenance models. The volume of sediment removed from debris basins increases with more intensive maintenance practices, and this results in a decrease in the amount of sediment removed from flood channels. The median sediment volume removed from the debris basin across fire frequencies for the SAW1 maintenance scenario was approximately 2.2 times greater than that of the S maintenance scenario. As a result, about 52% less sediment needed to be removed from the channel under the SAW1 scenario than under the S scenario. Figure 4.4 also shows that the amount of sediment that needs to be excavated from infrastructure per century increases dramatically with decreasing fire interval: under the 2-year fire interval scenario, the amount of sediment removed from the debris basin was 9.7 times greater and the amount removed from the flood channel 12 times greater than that under the 50-year fire interval scenario across all maintenance approaches.

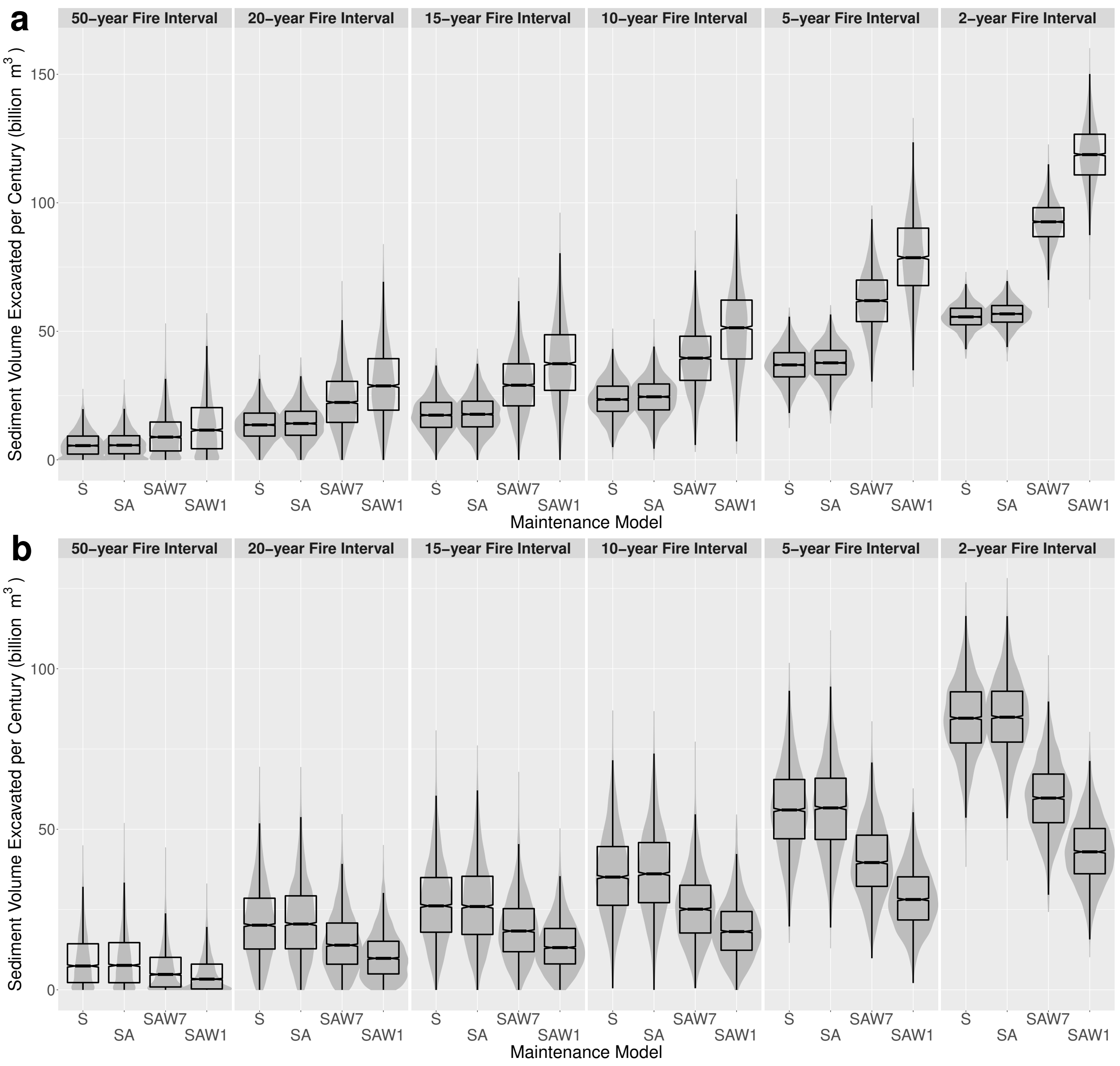

Figure 4.4: Simulated distributions of sediment volume removed from (a) debris basins and (b) flood channels per century versus maintenance approach (S, SA, SAW7, SAW1) and fire interval.

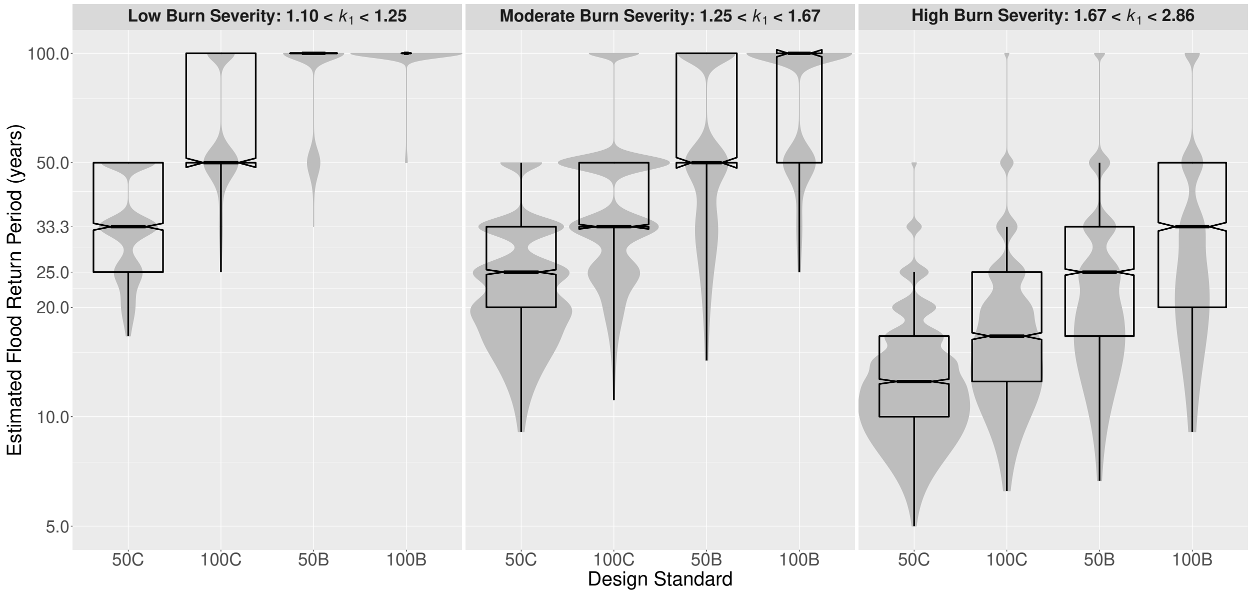

Figure 4.5: Simulated distributions of flood return period versus infrastructure design standard (50C, 50B, 100C, 100B) and fire burn severity (Low, Moderate, and High). Missing values are due to a lack of annual channel exceedances during simulation trials.

4.3.3 Flood and debris hazards vs. burn severity

Attention now turns to the influence of burn severity on flood return periods, which enters the modeling framework through the bulking factor, k. Figure 4.5 shows T_c distributions across the four *infrastructure design standards* (50C, 100C, 50B, and 100B) and three different levels of *burn severity* (Low, Moderate, and High). Figure 4.5 shows that with increasing burn severity, flood return periods are reduced. For example, in the case of Moderate Burn Severity, infrastructure designed based on a 100-year design storm and bulked design discharge (100B), the most conservative design standard considered, delivers protection corresponding to a 100-year return period, based on the median value. In transitioning from Moderate to High Burn Severity, the median T_c for design standard 100B is reduced from 100 to 33.3 years, corresponding to a three-fold increase in flood frequency.

Figure 4.6 shows T_c distributions across the four *maintenance approaches* (S, SA, SAW7, and SAW1) and three different levels of *burn severity* (Low, Moderate and High). These

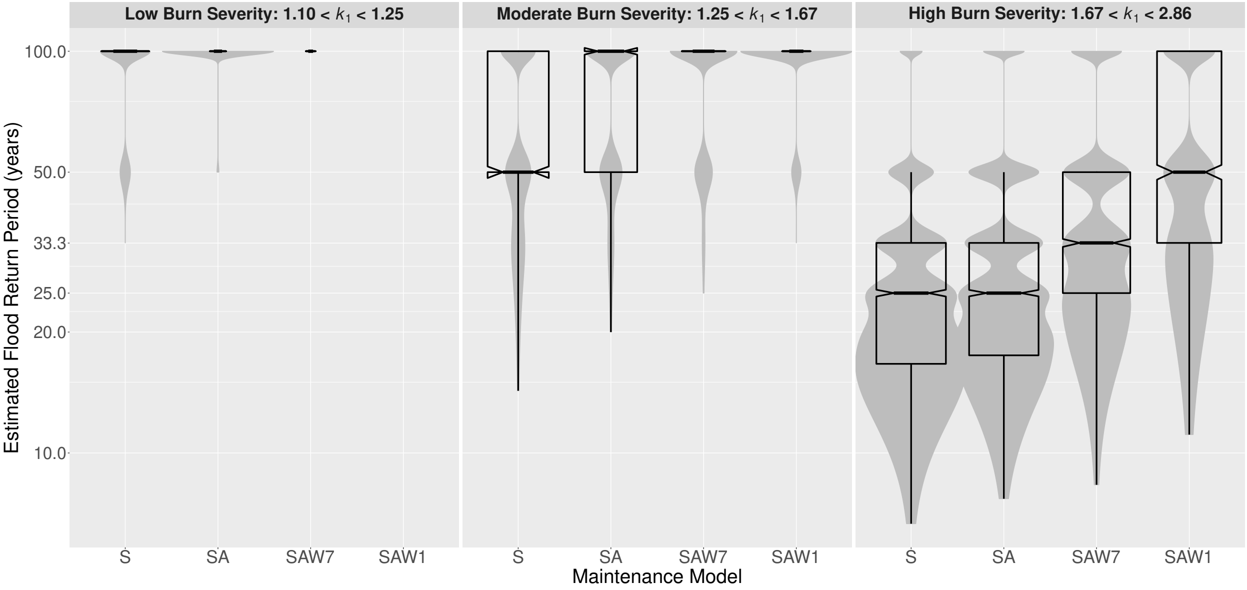

Figure 4.6: Simulated distributions of flood return period versus infrastructure maintenance approach (S, SA, SAW7, SAW1) and fire burn severity (Low, Moderate, and High). Missing values are due to a lack of annual channel exceedances during simulation trials.

.

simulations are based on infrastructure designed with a 50-year bulked (50B) design standard, and for cases of Low Burn Severity, that that level of protection is exceeded under all maintenance approaches: the median value of T_c is 100 years or greater in all cases. With Moderate Burn Severity, the median value of the simulated T_c distribution is 50 years based on the summer-only cleaning model (S)and increases to 100 years with the three other maintenance models. And finally, the case of High Burn Severity, the median T_c falls to 25 years for the summer cleaning scenarios (S and SA) and to 33.3 years for the SAW7 scenario, but retains the 50-year level of protection using the SAW1 maintenance approach. In the case of the High Burn Severity, the level of bulking is much higher than that assumed for infrastructure design purposes ($k_{\mathrm{des}} = 1.2$), which leads to a major reduction in the level of infrastructure performance compared to that of the Low and Moderate Burn Severity scenarios.

4.4 Discussion

The previous results clearly show that peak bulked flows may exceed the capacities of channels located below burn areas at frequencies far greater than inferred by the exceedance probability of precipitation used for infrastructure design. To this end, we define a hazard amplification factor,

$$A_F = T_{\mathrm{p}}/T_{\mathrm{c}} = p_{\mathrm{c}}/p_{\mathrm{p}} \tag{4.3}$$

which represents a ratio of the *frequency* of overtopping events for the marginal hazard (precipitation in the absence of wildfire) to that of the compound hazard. Results presented here point to hazard amplification factors ranging from 1.0 to 16.0 across all simulation scenarios.

To get a sense of present post-fire flood risks, consider the range of hazard amplification factors that results from scenarios combining the 50B and 100B design standards with the range of historically observed fire intervals in southern California, 7 years to 52 years (151): the median hazard amplification factors are 1.0, 2.0, 4.0, and 6.0 for the 50B/52-year scenario, 100B/52-year scenario, 50B/7-year scenario, and 100B/7-year scenario, respectively. For context, we note that the 50B design standard is a generalized representation of the design standard used by Los Angeles County (76; 77), which operates nearly 200 debris basins across the county.

Now consider future scenarios in which the fire interval decreases to 5 years or 2 years, resulting in median amplification factors of 4.5 and 7.0 for the 50B design standard and 7.0 and 11 for the 100B design standard, respectively (Figure 4.2). These constitute compound hazard estimates up to an order of magnitude greater than the return level for which the flood infrastructure is designed. With respect to our choice of 2 years for the lower bound of the fire interval, we do not expect fire intervals in the region to decrease below this value based on projections of future fire intervals and a review of post-fire watershed recovery in Mediterranean climates that found a minimum recovery period of 2 years (35; 163). This simple comparison demonstrates the potential of the modeling framework to predict future hazards based on any distribution of hazard drivers (e.g., fire interval, fire severity, precipitation intensity, changes in maintenance). Previous studies have documented the value of stochastic modeling for studying infrastructure performance (12), and there is growing interest in understanding non-stationarity in flood hazards. For example, non-stationarity in flood hazards has been linked to land use or land cover change (86), sea level rise (165), and more intense precipitation extremes (11; 144). However, predicting future distributions of hazard drivers is not straightforward. For example, projections of future precipitation have proven challenging, especially for California (55). That said, our model can be used to determine the consequences of assuming a particular distribution for a given hazard driver on the post-fire flood hazard, which may prove useful to flood management agencies until the uncertainty in projections is reduced.

The design and construction of flood infrastructure, as well as its maintenance, is affected by many factors including available financial resources and government permit requirements. Maintenance costs for infrastructure cleaning generally scale with the volume of material to be excavated, and the timing of the excavation. Excavation during the wet season may be several times more expensive than dry season excavation due to the physical processing required of wet sediment and mud, the challenge of finding a disposal site and other factors (116). Modeling results show the volumes of material requiring excavation increase by about an order of magnitude as fire interval decreases from 50 years to 20 years (Figure 4.4). Furthermore, simulations show that the volumes of material requiring excavation from channels decrease as excavation of debris basins becomes more aggressive. Our model produces quantitative estimates of the magnitude of excavation required to maintain flood infrastructure performance that could help flood management agencies evaluate the cost effectiveness of different maintenance approaches under multiple climate change scenarios and multidecadal planning timescales.

Increased awareness of hazard amplification among exposed populations could prove especially valuable for public safety. Given the short time period between wildfire containment in Summer or Fall and potential precipitation-induced flooding and debris flows in Winter or Spring, emergency responders and residents of the wildland-urban interface could be fatigued from fire mitigation and evacuation and less able to respond quickly to post-fire flooding and debris flows. Furthermore, residents who trust that debris basins and flood control channels will be sufficient to contain post-fire runoff and who are unaware of potential overtopping could be relatively unconcerned about flooding and debris hazards and be less prepared to respond (95; 54; 56). In addition, post-wildfire debris flows can travel with surprising speed several kilometers from the burn area, impacting unexpecting residents of the urbanized lowlands who in many cases may be of a lower socioeconomic status with fewer resources to respond compared to residents on higher ground along the wildland-urban interface (Fig. 2.1). Impacts on lowland residents could be particularly severe if sediment fluxes clog downstream flood control infrastructure resulting in unpredictable flow paths through these communities. For these reasons, advancing a greater understanding about hazard amplification and the potential limitations of flood control protections among emergency agencies and residents of these areas will be very important given the expected intensification of fire and storm events in coming years.

4.5 Conclusion

In this study, a new model is developed for estimation of compound post-fire flood hazards below mountain catchments based on multiple interdependent factors including the frequency and severity of wildfires, the effect of wildfire on sediment production and flood peaks, the presence of debris basins and flood channels to mitigate hazards, the loss of channel capacity from sedimentation and clogging, and the restoration of channel capacity with infrastructure maintenance. Compound hazards are estimated by counting overtopping events within century-long Monte Carlo simulations with stochastic inputs. While the model is applied here with parameters representative of southern California, it can be parameterized for other regions, making it highly transferable.

Application of the model shows that the hazard facing human populations may be up to an order of magnitude greater than what would be expected based on the return period of the primary hazard driver (rainfall) used for infrastructure design. Moreover, we find that this hazard amplification is sensitive to design standards. For example, in southern California where fire intervals are roughly 20 years on average, infrastructure designed based on extreme rainfall with a 50-year return period yields a level of protection corresponding to a 15- or 25-year return period depending on whether a clear-water (50C) or bulked flow (50B) design approach is used, respectively. This corresponds to a hazard amplification of 2.0-3.3. Similarly, designs based on extreme rainfall with a 100-year return period yields a level of protection corresponding to roughly 20- and 30-year return periods depending on whether a clear-water (100C) or bulked flow (100B) design approach is used. This corresponds to a hazard amplification of 3.3-5.0. Considering that the 50B and 100B design standard scenarios were based on infrastructure design standards currently used by two highly populated counties in southern California, these hazard amplification factors point to concerning limitations to the protection of human development from post-fire flood risk.

Simulations also show that differing maintenance approaches influence hazard amplification. For example, with a 20-year fire interval and a 50-year bulked design standard, the flood return period can range from 25 to 50 years across the four maintenance scenarios based on operational maintenance approaches in Riverside County. This corresponds to an hazard amplification of 2.0 and 1.0, respectively.

Stochastic simulations also reveal the sensitivity of compound post-fire flood hazards to a prominent aspect of the effects of climate change in southern California, increased wildfire frequency. For example, if fire intervals were to shift from 20 to 10 years, the median flood return period for the 50-year bulked flow design approach would be reduced from 25 to 17 years. Hence, the hazard amplification would increase from 2.0 to 3.0. Furthermore, simulations show that shifts in burn severity also increase the hazard amplification. For example, infrastructure that is constructed based on a 50-year bulked flow design standard and experiences only moderate burn severity events (which match the design standard) exhibit a 50-year level of protection, but a shift to high burn severity reduces the flood return period to 25 years, corresponding to a hazard amplification of 2.0.

The ability of this original modeling framework to quantify compound post-fire flood hazards as a function of wildfire severity and frequency, precipitation intensity, and flood infrastructure design and maintenance makes it a useful tool for risk management. In particular, model applications can support flood risk communication efforts to increase awareness of the heightened flood hazards. Furthermore, the model could be applied to back-calculate the sizing of infrastructure and maintenance levels needed to achieve a specific standard of protection, such as a 50-year return period.

Chapter 5

Spatial Distribution of Hazards and Risks

5.1 Introduction

Characterization of the spatial distribution of sediment-laden flood hazards is essential to increase risk awareness, develop flood mitigation strategies, and increase community risk awareness and preparedness. Southern California is especially vulnerable to sediment-laden flood hazards based on combinations of steep topography, frequent wildfires, expansive urban development, and intense precipitation (70). Riverside County, California is a particularly good test case for estimating post-fire flood risk due to the presence of three mountain ranges forming a border around the most populated portion of the county: the Santa Ana Mountains, the San Bernardino Mountains, and the San Jacinto Mountains. The San Bernardino Mountains are well known for producing debris flows during post-fire storms, and post-fire debris flows have been observed in the San Jacinto as well (17; 39). Further, many areas of Riverside County are currently unoccupied by human development but are rapidly being developed as nearby urban centers such as Los Angeles expand. This rapid urbanization trend creates a patchwork of rural, peri-urban, and urban areas that is an interesting setting for the study of sediment-laden floods: for example, concrete-lined flood channels do not exist for many communities that are less densely populated or that were established before the construction of formal flood infrastructure was common (117). Instead, these areas have natural, or unlined, flood channels that have poorly defined banks and tend to shift flow paths over time. The spatial heterogeneity in population density and the presence (or absence) of formal flood infrastructure makes Riverside County the ideal setting for a regional study of flood hazards downstream of mountain canyons.

Previous work developed a parameterization and calibration framework for PF2HazMo to apply the model to specific watersheds and flood infrastructure systems. The present study systematically applies PF2HazMo to watersheds across the Santa Ana Mountain Range in Riverside County to obtain a spatial distribution of sediment-laden flood risk. The identification of flood risk hotspots can inform the design and maintenance of both current and future flood infrastructure and support long-term emergency preparedness and risk communication efforts. An analysis of potential drivers of areas with the greatest risk including differences in natural factors such as watershed topography, fire recurrence interval, and precipitation extremes, as well as anthropogenic factors such as the type and capacity of flood infrastructure, is necessary to develop a better understanding of the spatial distribution of present-day post-fire flood hazards. Once this baseline hazard is understood, a comparison to simulations of future post-fire flood risk accounting for changes to wildfire and precipitation frequency and intensity will provide an understanding of the management strategies needed for long-term flood risk management.

This study aims to address the following research questions:

1. Where are the hotspots of post-fire flood risk in Riverside County, CA based on current

fire frequencies, precipitation statistics, and infrastructure capacities and maintenance approaches?

2. What are the key drivers (both natural and anthropogenic) of post-fire flood risk for catchments with the greatest risks?

Since post-fire flood frequency estimates for Leach watershed, which had an unlined channel, were much greater than those for McVicker watershed, which had a concrete-lined channel, we hypothesize that in general, infrastructure systems with lined channels mitigate flood risk better than those with unlined channels (see Section 3.2.4).

5.2 Methods

The following methodological sections cover a description of the study catchments, the methods used and data analyzed to apply the modeling framework, and the correlation and significance testing analysis used to determine the drivers of the sediment-laden hazard.

5.2.1 Site Identification and Description

Watersheds were selected for hazard modeling by examining maps of wildfire variables (such as fire recurrence interval and historical fire perimeters), precipitation variables (such as 100-year 15-minute precipitation intensity), and downstream population characteristics (such as population density). We targeted areas where high fire hazard, high precipitation hazard, and high population intersected and noted whether flood infrastructure was present in these areas. Finally, we consulted with Riverside County to identify additional locations where post-fire flood hazards had occurred in the past based on their expertise and boots-on-the-ground experience. Figure 5.1 presents the watersheds included in the regional application of

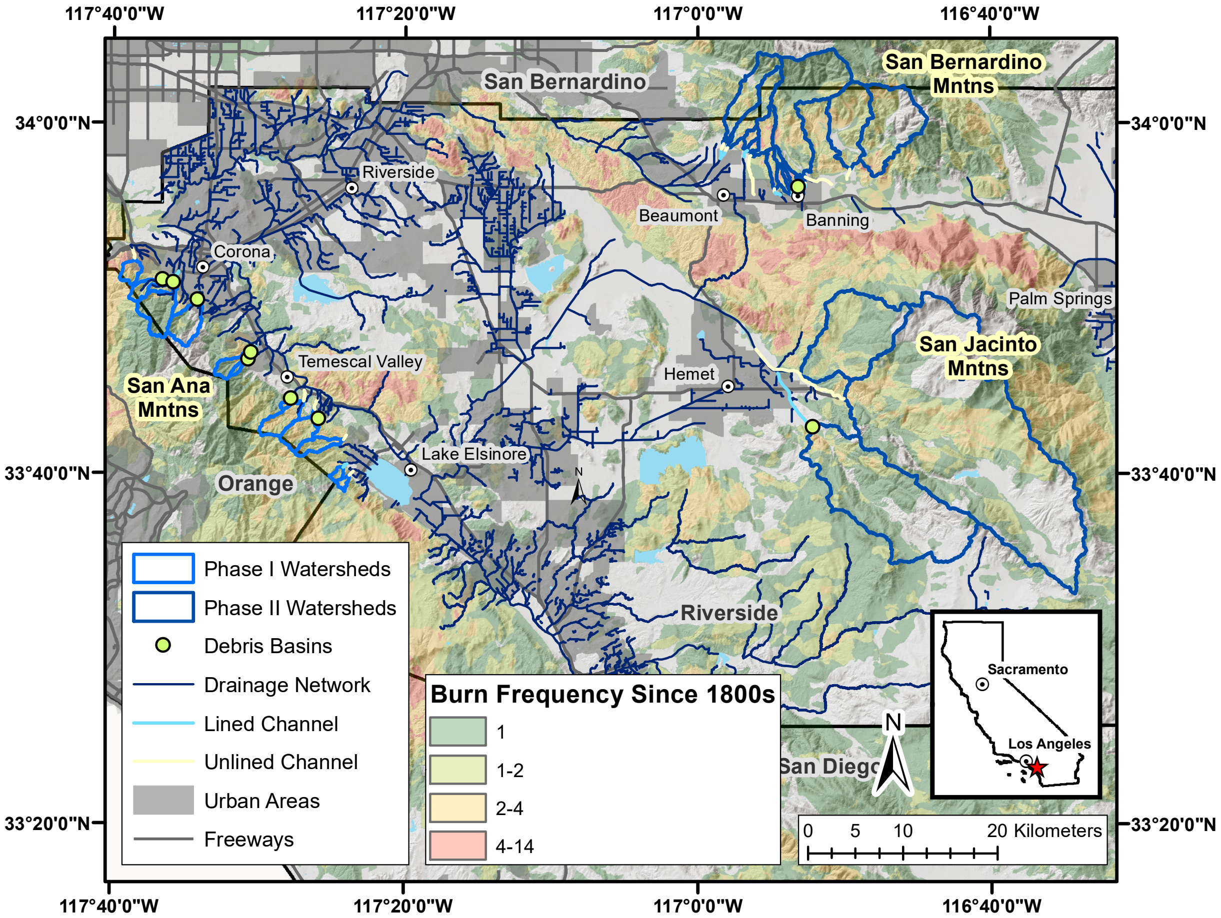

Figure 5.1: Map of Riverside County watersheds for which the spatial distribution of hazards will be estimated. Urban areas are defined by population density >1,000 people per sq. mi.

.

PF2HazMo. Phase I watersheds are covered in this chapter, while the estimation of hazards for Phase II is currently underway.

The Phase I watersheds included in this study represent mountain watersheds across the Santa Ana Mountains with variability in drainage area, watershed slope, mean fire interval, precipitation intensity, and infrastructure type and capacity (n=13). Of the 13 study sites, six have only a flood channel, three have only a debris basin, and four have both types of flood infrastructure. Of the ten watersheds with downstream flood channels, five are concrete-lined and five are unlined (i.e., soft-bottom/natural). Additionally, the downstream populations display spatial variation in characteristics such as population density, median household

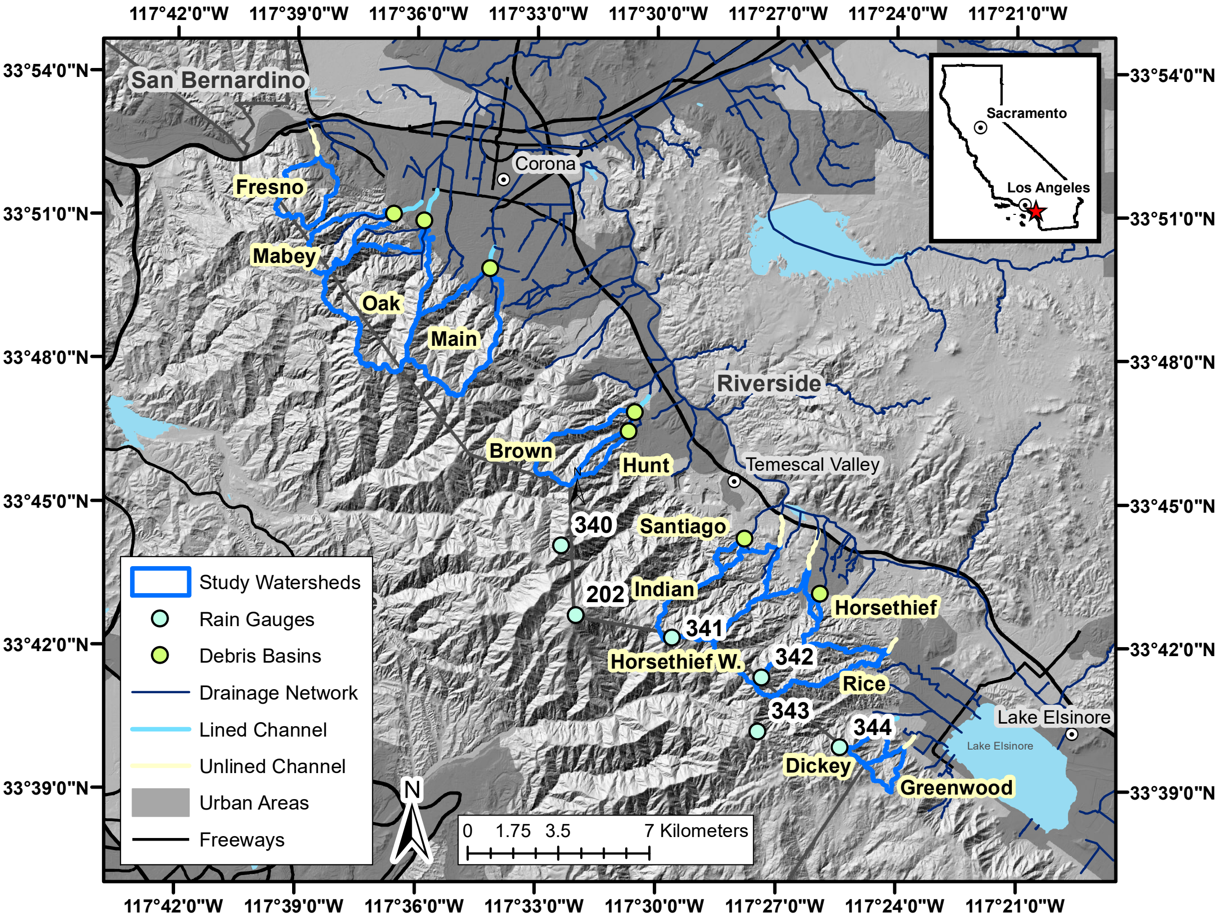

Figure 5.2: Map of watersheds included in the present study (Phase I). Urban areas are defined by population density >1,000 people per sq. mi.

.

income, and Neighborhood Disadvantage Index (NDI), a composite social vulnerability index calculated from 25 socioeconomic variables from the American Community Survey (130). Figure 5.2 displays a map of the catchments studied in Phase I. The methods used to calculate these physical and socioeconomic site characteristics are described in Section 5.2.5.

5.2.2 Simulation Scenario

Present-day sediment-laden flood hazards are estimated by considering a 100-year simulation of wildfires, storm events, and infrastructure maintenance. The model is forced with a time series of daily precipitation reflective of historical precipitation statistics that is spatially averaged over the contributing area of each watershed to reflect differences in spatial rainfall patterns. Wildfire occurrence and severity are treated as random variables, fire frequency is set to the mean fire recurrence interval (representative of the historical fire regime), and fire severity is bracketed by a range of post-fire bulking factors estimated on a site-by-site basis. The post-fire recovery timescale is also treated as a random variable, since the recovery time of watershed vegetation following fire has been linked to vegetation type, water availability during recovery period, terrain slope/aspect, burn severity, and soil hydrological properties and thus has significant spatial heterogeneity that is best captured through random sampling for the purposes of this study (45; 53; 72; 24). Across the study sites, infrastructure design capacities are estimated from data on the actual capacities of "empty" flood infrastructure, and the infrastructure maintenance approach consists of summer, after-fire, and wet season cleaning with a cleaning threshold of 85% and a wet season waiting period of 1 day based the standard maintenance schedules and excavation records of Riverside County. PF2HazMo model outputs include the number of flood channel and debris basin exceedances per century and the annual exceedance probability of each type of infrastructure (depending on which is present for each study site). The annual exceedance probability is calculated as the number of years with at least one exceedance divided by 100 years, the number of years in the simulation. We report annual exceedance probabilities based on channel exceedances if the study site has a flood channel or based on debris basin exceedances if only a debris basin is present. For each study watershed, 3,000 stochastic simulation trials are produced to generate a distribution of estimates for each hazard variable.

5.2.3 Parameter Estimation

Table 5.1 summarizes the model parameters and estimation methods used to parameterize the model for regional hazard estimation.

Table 5.1: Summary table of model parameters and estimation methods.

Parameter Name	Symbol	Approach	Data	Reference
Watershed Area	A	GIS analysis	10-m DEM from USGS	-
Runoff Response	c_t	Frequency Curve Approach	Regional Rainfall and Discharge Frequency Estimates	Section 3.1.4
Time to Peak	t_{p}	Median storm duration across rain gauges	Rain gauge records	(71)
Fire Interval	t_{f}	Spatially average over watershed area	30-m raster of mean fire return interval	(78)
Post-fire Bulking Factor	k_1	LA Debris Method with A-T Factor for Santa Ana Mntns	Regional Rainfall Frequency Estimates, sediment yield estimates from DEM differencing, watershed morphology	(40)
Recovery Timescale	t_{r}	Defin range based on observed post-fire vegetation recovery times	Reported recovery times in literature	(79; 39; 38)
Debris Basin Design Capacity	$\cancel{V}_{\mathrm{b}}^{\mathrm{des}}$	GIS analysis	1-DEM from USGS	
Flood Channel Design Capacity	$D_{\mathrm{c}}^{\mathrm{des}}$	2D flood inundation modeling	1-DEM from USGS, 0.5-m Lidar-derived DEM from Riverside County	(128)
Infrastructure Cleaning Threshold	$\cancel{V}_{\mathrm{thresh}}$	Set to 85% based on communication with Riverside County	-	(117)
Wet Season Cleaning Waiting Period	w	Set to 1 day based on analysis of excavation records	Excavated sediment volumes at roughly daily intervals	-
Wet Season Debris Basin Cleaning Rate	r	Average daily volume excavated	Excavated volumes of sediment from Leach and McVicker debris basins	-

Runoff Response and Time to Peak

The runoff response parameter, c_t was estimated using the Frequency Curve Approach described in Chapter 3, Section 3.1.4. Since observed streamflow data was only available for a single streamgauge in the Phase I study region with <5 years of data, we chose to apply the Frequency Curve Approach to each watershed, which calibrates the runoff response parameter, c_t, to precipitation and discharge frequency estimates spatially interpolated from regional networks of ground-based observations. Since the objective of this study is to estimate flood hazards on a multidecadal time scale (100 years), calibrating the runoff response parameter based on long time series of extreme hazard statistics will ensure the model produces hazard estimates reflective of the peak flow statistics in the region. Descriptions of the precipitation and the discharge frequency estimates used to estimate the runoff response parameter are provided in Sections 5.2.5 and 5.2.5, respectively.

The time to peak parameter, t_p, was estimated from statistical analysis of observed storm durations using rain gauge data. We calculated t_p as storm duration divided 2, an approximation of the method described by (136). The rain gauge observations used to estimate the time to peak parameter are described in detail in 5.2.5.

Post-fire Bulking Factor

The range of post-fire bulking factors, k_1, for each watershed was estimated by applying the LA Debris Method to each "*n*-year" return period event in the frequency curves for each watershed, using a range of Fire Factors, and setting the lower and upper bounds to the minimum and maximum estimated bulking factor, respectively. This approach is essentially the same as that used in Chapter 3 (see Section 3.1.3), but instead of using HEC-HMS to apply the LA Debris Method to simulated hydrographs, the LA Debris Method is applied directly using the appropriate peak precipitation and flow statistics for each watershed.

The LA Debris Method consists of a set of five regression equations with unit sediment yield as the dependent variable (sediment volume normalized by watershed area) and watershed area, relief ratio, Fire Factor, and either 1-hour peak precipitation or unit peak discharge (volumetric discharge normalized by watershed area) as the independent variables. Each of the five equations is applicable to a class of watershed areas, with Eqn. 1 applicable to areas in the range (0.256-7.77 km^2) and Eqn. 5 applicable to areas in the range (129-518 km^2); the fact that the method was developed for a wide range of watershed areas makes it particularly suited to regional applications. The relief ratio is defined as the watershed relief (difference between highest and lowest elevation) and the length of the longest flow path (maximum stream length measured along the longest stream); Section 5.2.5 explains how these values were obtained. The Fire Factor is a dimensionless parameter that represents the impact of wildfire on debris yield with a value of 6.5 representing ten years since 100% of a given watershed burned at a value of 3.15 representing one year since 100% of the watershed burned; we simulated sediment yields for each of these cases to obtain a representative range of post-fire bulking factors. Finally, the hydrological forcing for the LA Debris Method is 1-hour peak precipitation for Eqn. 1 and unit peak runoff for Eqns. 2-5. This difference in hydrological forcing is due to the lack of availability of peak discharge observations for small watersheds and strong correlation with 1-hour maximum precipitation found in the study (40). To implement the LA Debris Method, we spatially averaged 1-hour precipitation frequency grids by watershed area; these were used directly for watersheds that fell in the area class represented by Eqn. 1. To obtain unit peak runoff, we used the Rational Method to calculate the peak discharge corresponding to the 1-hour, area-averaged precipitation and the runoff response parameter, estimated as discussed in Section 5.2.3. The peak discharge calculated from the Rational Method was then divided by watershed area to obtain the unit area runoff needed to apply the LA Debris Method.

Another new methodology applied in this study is the use of a dimensionless parameter termed the Adjustment-Transposition (A-T) Factor to modify the sediment yield estimates from the LA Debris Method to account for the erosion rate specific to the Santa Ana Mountains. The A-T Factor, developed by Gatwood et al. (40), allows the LA Debris Method to be applied outside the region to which its regression equations were developed by estimating the A-T factor based on event-based or annual average sediment-yield data for the site of interest. Since this study aims to produce a spatial distribution of flood hazard estimates, accounting for differences in the geomorphic and geologic properties of the mountain ranges in the region is important. The estimation of the A-T Factor for the Santa Ana Mountains from post-fire sediment yield data is described in Section 5.2.5.

Recovery Timescale

The recovery timescale, t_r was treated as a random variable by sampling from a range of values representative of the range of recovery times reported in the literature for post-wildfire watershed vegetation recovery in southern California. While it is possible to estimate this parameter on a site-by-site basis using the method using remotely sensed vegetation indices described in Section 3.1.3, preliminary testing of the application of the method to burn areas throughout Riverside County found that there is a substantial amount of noise in the vegetation recovery signal. Indeed, studies have shown that post-fire vegetation recovery is a function of many factors including water availability during the recovery period (e.g. drought, soil moisture), terrain slope/aspect, burn severity, and soil hydrological properties (45; 53; 72; 24). Estimation of these confounding factors across the study region is outside the scope of this study, and the finding that the recovery time scale is not a highly sensitive model parameter when ranked by sensitivity coefficient or correlation coefficient (Section 3.2.1) motivate our choice to treat the recovery timescale as a random variable. The range of recovery timescales was bracketed by watershed recovery times of two to ten years (79; 38; 39). The recovery timescale was back-calculated by setting $k(t) = 1.01k_0$ when t equals the the observed recovery time and rearranging Eq. 3.2 (Section 3.1.2) to solve for t_r.

Infrastructure Capacity and Maintenance Parameters

To estimate debris basin capacity, we used the same method as delineated in 3.1.3 in which we estimated the volume of the empty debris basin using the Surface Volume tool in ArcGIS (30). The Digital Elevation Model (DEM) used in this analysis had a horizontal resolution of 1-m and is described in greater detail in Section 5.2.5.

To estimate flood channel capacity, we used PRIMo, a dual-grid flood inundation model, to determine the maximum flow rate the flood channels could convey without producing overbank flows (128) as described in 3.1.3. The flood inundation simulations were conducted for all channels simultaneously owning to PRIMo's ability to produce flood simulations over regional scales at fast compute times. Since the model domain was large (roughly 25 km square), we used spatially distributed Manning resistance parameters based on 30-m National Land Cover Database (NLCD) 2019 data (29). The NLCD classes were assigned Manning resistance parameter values based on Chow (25) for most undeveloped land cover types; land use types that typically represented the location of unlined channels were assigned Manning resistance values used by Riverside County and the U.S. Army Corps of Engineers representative of "natural channels with heavy vegetation" (31). Manning resistance parameters for medium and high intensity development were based on (34). We used a 1-m DEM from the USGS as the terrain data used for flood inundation modeling and an upscale factor of 5 for all but three sites: for the Mabey site, the channel width was approximately 5 m, so we used an upscale factor of 2 to resolve the flow dynamics at the appropriate scale. For the Dickey and Greenwood sites, channel widths were even smaller, $\sim$4 m, so we used a 0.46-m resolution DEM derived from Lidar as the terrain forcing with an upscale factor of 2 (see Section 5.2.5). Lastly, when calculating infrastructure exeedances we applied a tolerance to overbank flows to constrain the number of simulated exceedances, which otherwise would count any amount of overbank flooding as an exceedance. We set the overbank flow tolerance to 2% of the design infrastructure capacity.

The same infrastructure maintenance parameter values were used across all sites for consistency and based on communication with Riverside County. The infrastructure cleaning threshold was set to 85% based on the typical maintenance protocols implemented by Riverside County (116). The wet season cleaning waiting period, w, was set to one day based on an analysis of wet season debris basin cleaning frequency from excavation records for the 2018-19 wet season for Leach and McVicker debris basins (detailed in Section 3.1.3). The wet season debris basin cleaning rate, r, was set to the average daily volume of sediment excavated based on excavation records for both Leach and McVicker debris basins.

5.2.4 Correlations with Hazard Drivers and Population Characteristics

To develop an understanding of the drivers of sediment-laden flood hazards in areas facing the greatest risks, we performed correlations between the simulated hazard variables and a suite of physical and socioeconomic variables aggregated to the watershed scale. The physical factors included: watershed area, runoff response parameter, average percentage slope of the watershed, mean bulking factor, area-averaged fire interval, area-averaged 15-minute 100-year precipitation, debris basin capacity, and flood channel capacity. The socioeconomic factors included: population density per square mile, median household income, and NDI. Data sources and pre-processing procedures for the correlation variables are described in Section 5.2.5.

Correlation analysis was conducted using the R programming language and the “rcorr” function from the Hmisc package (111; 51). Spearman correlation was used to determine whether a monotonic correlation between hazard variables and the aforementioned physical and socioeconmic variables existed; we used Spearman correlation, a nonparametric measure of rank correlation between variables, since the data for several variables were not normally distributed. The sign of the reported Spearman rank correlation coefficient, ρ, indicates the direction of the relationship between two variables, while the value ranges between -1 and 1; a value close to -1 or 1 indicates a monotonic, though not necessarily linear, relationship in which one variable tends to increase or decrease as the other increases.

5.2.5 Data Sources

Precipitation

We retrieved Daymet V4 daily rainfall grids at 1-km resolution for 42 years (1 January 1980 to 31 December 2021) from Google Earth Engine and averaged them by watershed area to generate the model forcing. Daymet V4 daily precipitation summaries represent an interpolation of rainfall observations from a national network of ground-based meteorological stations, the NOAA National Centers for Environmental Information's Global Historical Climatology Network (146). To obtain a 100-year time series of daily rainfall from the 42-year time series for each watershed, we first spatially averaged the rainfall grid by watershed area using ArcGIS (30) for each day in the time series; then, we repeated the time series sequentially three times and truncated the result to 100 years. This allowed us to capture the historical precipitation statistics of each site while accounting for spatial variability over the area of the watershed, which is especially important for larger watersheds.

Precipitation frequency estimates were needed to estimate the runoff response parameter, the post-fire bulking factor, and the 15-minute precipitation variable for the correlation analysis. To estimate the runoff response parameter, we retrieved precipitation frequency estimate grids for a 6-hour storm duration for return periods of 2, 5, 10, 25, 50, 100, 200, and 500 years from NOAA Atlas 14 as described in Chapter 3 (106). We then spatially averaged the precipitation estimates by watershed area to obtain a spatial average for each watershed. To estimate the post-fire bulking factor, the LA Debris Method Eqn. 1 specifies that 1-

hour maximum precipitation must be used to estimate debris yield, so we retrieved NOAA Atlas 14 precipitation frequency estimates for the same return periods for a 1-hour storm duration and performed the same spatial average analysis to produce a 1-hour precipitation frequency curve for each watershed. Finally, as a precipitation variable to include in the correlation analysis described in Section 5.2.4, we retrieved the 15-minute duration, 100-year precipitation grid and calculated a spatial average over the area of each watershed. We chose the 15-minute duration because 15-minute peak rainfall intensity was found to be a significant driver of debris flow volumes during storms within two years after wildfire in the Transverse Ranges of southern California (39).

Lastly, sub-daily rainfall data were needed to estimate the time to peak parameter from observed storm duration. We used precipitation data from six tipping-bucket rain gauges located near the study watersheds at high elevations to calculate storm durations; the rain gauge records had record lengths from one wet season to 26 years, with gauge 202 having the longest record (see Figure 5.2). Rainfall data was quality controlled by removing values greater than 0.08 in, or twice the precipitation per tip. We then applied a storm identification algorithm written in MATLAB that separates the precipitation into storms after 6 hours with <0.05 in of rainfall and omits storms with a depth of <0.3 and an intensity of <0.2 in [add matlab citation]; the intensity threshold is based on the 6-hour precipitation intensity threshold for triggering debris flows reported in (139).

Discharge Frequency Estimates

Discharge frequency estimates corresponding to the same return periods as the precipitation frequency estimates were obtained by applying the StreamStats online tool to each watershed individually (153). These discharge estimates are calculated using regional regression equations developed by fitting a log-Pearson Type III distribution to annual peak flow data through water year 2006 from a network of USGS streamgages in California with 10 or more years of data (44).

Topography and Watershed Morphology

Watershed area was calculated using a 10-m DEM from the U.S. Geological Survey (USGS) using ArcGIS software (30). Average percentage slope of the watershed was determined using the same 10-m DEM after applying the Fill tool in ArcGIS to remove noise in the form of elevation sinks. Watershed characteristics such as relief and length of longest flow path were used to estimate the post-fire bulking factor and were calculated for each watershed using the StreamStats online tool (153).

Debris basin capcity and most of the channel capacities were estimated using a 1-m DEM from the USGS produced in 2018 before the start of the wet season (154). Dickey and Greenwood channels were estimated from We used a DEM produced from a 0.46-m DEM derived from an airborne Lidar survey conducted in September 2018 before the start of the wet season with a resolution of 0.46 m (1.5 ft) and vertical accuracy of 3.02 cm (0.099 ft, RMSE). The reason it is important that the topographic data were surveyed before the start of the wet season is that sediment can accumulate in the flood channels during post-fire storms, and the infrastructure capacity estimates are meant to represent clean/empty infrastructure. DEMs used for channel capacity estimation were hydro-conditioned in ArcGIS to remove bridges and culverts.

Fire Interval

A 30-m raster of mean fire return interval from the LANDFIRE program was used to calculate a spatially averaged fire interval for each watershed area (78). This variable represents the average number of years between fires under the presumed historical fire regime as calculated by a vegetation disturbance dynamics model (123). It is a joint product of the

U.S. Department of Agriculture Forest Service and the U.S. Department of the Interior.

Sediment Yield Estimates

To apply the LA Debris Method equations for estimating post-fire sediment yields regionally, Gatwood et al. (40) developed a dimensionless parameter to account for regional differences in geomorphology and geology called the Adjustment-Transposition, or "A-T" Factor. The A-T Factor can be estimated using event-based or periodically collected sediment yield data to modify the sediment yield estimates produced by the method based on the erosion rates of the specific location to which they pertain. For this study, we calculated the A-T Factor as the ratio of observed event-based sediment yields to the unadjusted sediment yield estimated from the LA Debris Method for several post-fire storm events (40, Appendix B, Technique 1). Our observed sediment yields are derived from DEMs produced from five (5) photogrammetric surveys of the Leach and McVicker debris basins conducted throughout the 2018-19 wet season following the Holy Fire (described in Chapter 3, Section 3.1.3). We calculated the difference in elevation between DEMs from successive surveys (a technique known as "DEM differencing") to estimate the volume change in the debris basin over time. The DEM differencing resulted in four (4) estimates of sediment change for each of the two debris basins throughout the wet season (n=8); excavation of the debris basins was occurring during this time, and excavation volumes obtained from excavation record kept by Riverside County were used in conjunction with the sediment volume change values to calculate the sediment flux into the debris basin by computing a mass balance.

Once sediment yields were estimated from debris basin surveys, the corresponding maximum 1-hour precipitation for the time period corresponding to each sediment yield estimate was calculated from rain gauge data for use in the LA Debris Method equations. Finally, the A-T Factor for each for each pair of observed and estimated sediment yields was calculated as:

$$\mathrm{A-T\ Factor} = \frac{\text{Sediment Yield Calculated from DEM Differencing}}{\text{Sediment Yield Calculated from LA Debris Method}} \tag{5.1}$$

and an overall A-T Factor for the Santa Ana Mountains was calculated as the median of the event-based A-T Factors. We note that each sediment yield estimate derived from DEM differencing does not correspond precisely to one storm event due to logistical limitations on the frequency of UAV surveys by Riverside County, contributing some uncertainty to the sediment yield estimates. However, these estimates represent the best available post-fire sediment yield data for the watersheds in this mountain range at this time.

Population Characteristics

Socioeconomic characteristics for populations downstream of the flood infrastructure systems at each study site were selected from the 2016-2020 American Community Survey (ACS) variables at the block group level (149). We chose population density in terms of people per square mile to determine whether risks were greater in more populated areas and median household income as a proxy for the ability of households to manage their flood risk based on the financial resources available to them. NDI is a composite index of 25 variables from the 2016-2020 ACS at the block group level that include measures of socioeconomic, housing, education, and employment status (130). Higher NDI values indicate greater disadvantage.

To define a single estimate of each socioeconomic variable for each study site to include in the correlation analysis, we first defined the block groups that comprised the population exposed to flood hazards downstream of each study watershed. This was done by intersecting the length of flood channels used in channel capacity estimation with the block group boundaries in ArcGIS; any block group with a boundary intersected by the flood channel was included as a “downstream community” of the channel with the potential to be affected by flooding if the channel overtopped. We note that while this definition may exclude block groups not immediately adjacent to the channel yet still subject to flooding if the magnitude of overbank flows is great enough, this method is designed to identify exposed populations in a systematic way and at the very least ensures those populations exposed directly to fluvial flooding are captured. The downstream community for watersheds with only debris basins present was defined by simulating overtopping just downstream of the debris basin with PRIMo and including those block groups within the flood extent.

Based on these methods, downstream communities varied between one and three block groups for each study site. It was possible to calculate a representative value for each downstream community for population density and median household income because the ACS includes variables for total population and aggregate household income at the block group level. We calculated population density as the total population in all the block groups of each downstream community and divided by the total area of these block groups in square miles. We calculated median household income as the sum of the aggregate household income of all block groups in the downstream community divided by the number of households in these block groups. NDI, however, could not be aggregated at the downstream community level, so we calculated an average NDI and an area-weighted NDI, to account for differences in the area covered by each block group, across block groups and used both metrics in our correlation analysis.

5.3 Results

5.3.1 Spatial Distribution of Sediment-laden Flood Hazards

The distributions of annual exceedance probability (AEP) of the flood infrastructure at the outlet of each study watershed based on a 100-year simulation and 3,000 simulation trials are presented in Figure 5.3. It is immediately clear that two study sites have far greater AEPs than the others: Greenwood Dr. and Indian. Both of these channels are unlined, and Greenwood Dr. has the smallest channel capacity of all the watersheds with flood channels, while Indian had the third lowest channel capacity (the same channel capacity as Rice). We note that the estimated median AEP of 0.98 for Greenwood Dr. means that the model predicts that the channel would overtop nearly once every year, which seems unrealistically high; that said, it is reasonable that the exceedance probability would be high compared to the other sites given the unlined flood channel in question is more of an informal drainage ditch <4 m wide with poorly defined channel banks based on inspection of the 0.46-m DEM used to estimate its capacity.

Turning attention now to the sites with the third and fourth greatest median AEPs, the Oak St. and Main St. watersheds both have debris basins and concrete-lined channels and yet are predicted to have among the highest AEP values. The median AEPs for Oak St. and Main St. are 0.20 and 0.16 which correspond to flood return periods of 5 and 6.25 years, respectively. It is an interesting finding that two watersheds with both types of flood infrastructure are predicted to have such high AEPs once the possibility of infrastructure clogging with sediment is taken into account. The fact that both of these watersheds have lined flood channels contradicts our hypothesis that lined channels are generally more protective than are unlined channels.

Figure 5.4 displays the predicted number of debris basin exceedances for the 100-year sim-

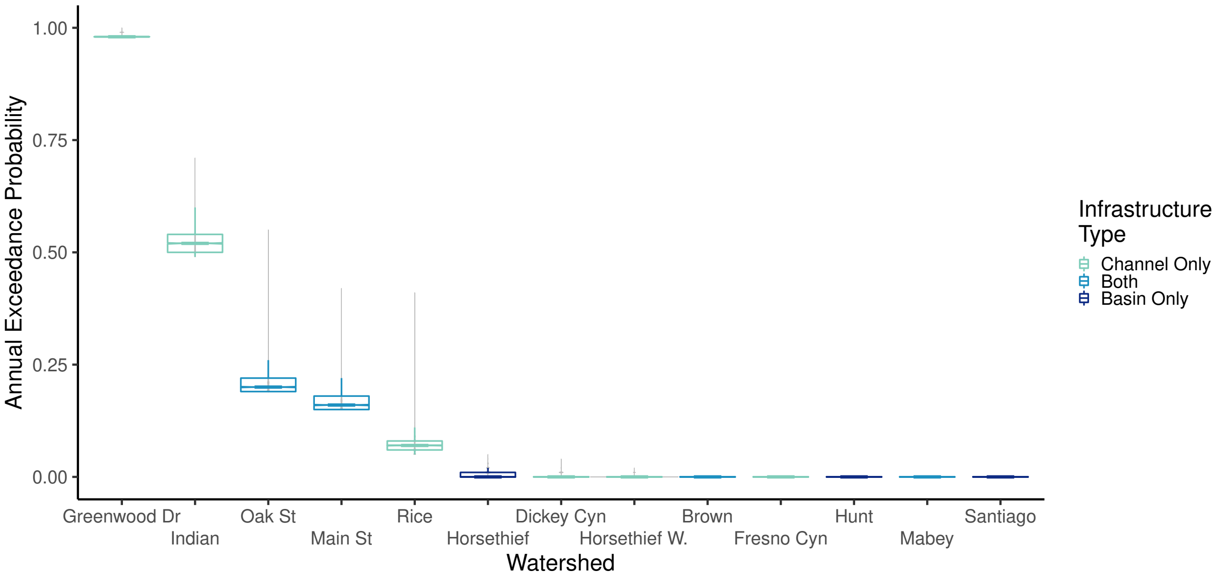

Figure 5.3: Distributions of annual exceedance probability of flood infrastructure.

.

ulation period across all watersheds with a debris basin. Main St. and Oak St. again rank highly in terms of infrastructure exeedances, and the distributions of the number of exceedances span two orders of magnitude. In contrast to the sites with high AEPs, Main St. and Oak St. have debris basin with high capacities: the second and third largest debris basins after Mabey debris basin. However, these two sites do have the largest watershed areas and among the highest mean bulking factors of all the study watersheds, and PF2HazMo was found to be highly sensitive to both parameters (Chapter 3, Section 3.2.1). The two sites with the lowest median number of basin exceedances and least variability within the distributions, Mabey and Horsethief, also have the lowest mean bulking factors of all the sites. The ranking of watersheds from greatest to least basin exceedances per century roughly tracks with the ranking of greatest to least mean bulking factor (with the exception of Oak St., which has a greater mean bulking factor than does Main St.).

The number of channel exceedances that occurred over the 100-year simulation for watersheds with a flood channel is shown in Figure 5.5. Greenwood Dr. is estimated to have ∼1,000 channel exceedances over the century and Indian is expected to have about 200, while the rest

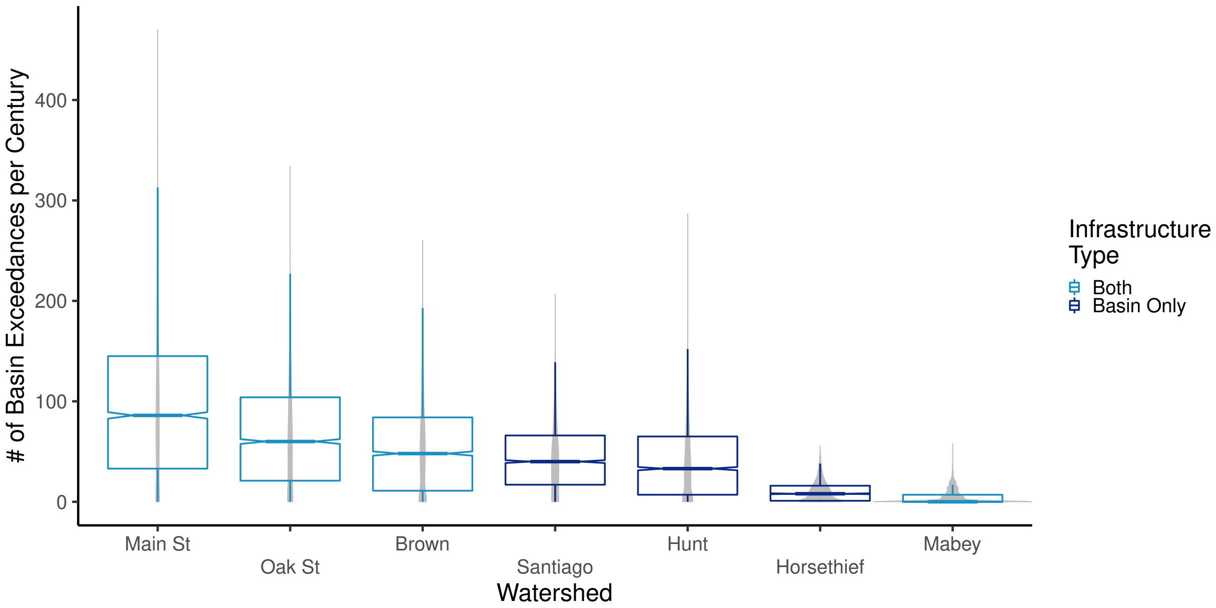

Figure 5.4: Distributions of the number of debris basin exceedances per century.

.

of the watersheds are predicted to have 33 or fewer (based on the median of the distributions). Oak St., Main St., and Rice have medians of 33, 28, and 15 channel exceedances per century, respectively.

5.3.2 Correlation Analysis and Significance Testing to Determine Flood Hazard Drivers

Scatterplots for correlations between model response variables and physical variables that were significant at the 95% confidence level, and socioeconomic variables that were significant at the 90% confidence level, are shown in Figure 5.6 (additional correlation results shown in Figure C.1). Figures 5.6a and 5.6b show the expected positive relationships between the post-fire bulking factor and the number of basin exceedances and watershed area and the number of basin exceedances. The negative correlation between channel capacity and the maximum number of channel exceedances across simulation trials illustrated by Figure 5.6c corroborates the result that channels with lower capacities tended to have greater AEPs

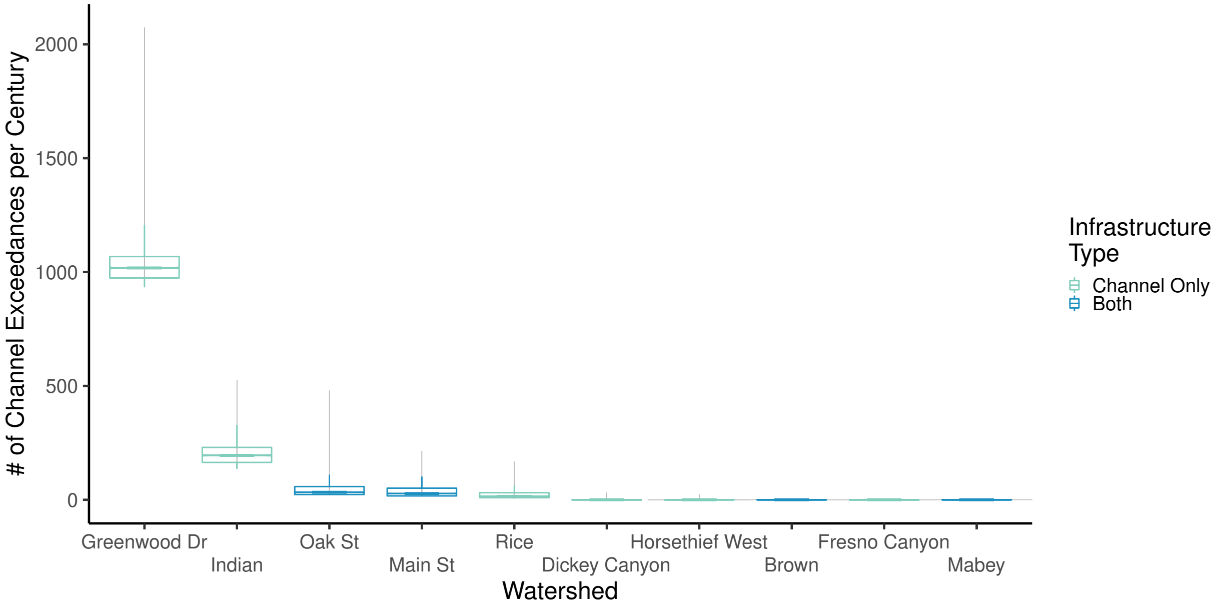

Figure 5.5: Distributions of the number of flood channel exceedances per century.

.

(Figure 5.7).

With respect to correlations between population characteristics and model response variables, an unexpected positive correlation between population density and the maximum number of basin exceedances is shown in Figure 5.6c. This result indicates that when considering the highest estimates of debris basin exceedances across simulation trials, areas with greater debris basin exceedances are also those with greater downstream population densities. Further, we found a negative correlation between average NDI and the median number of debris basin exceedances. This negative correlation suggests that downstream communities exposed to higher numbers of debris basin exceedances tend to exhibit less socioeconomic disadvantage (i.e., more advantage) on average. Since the *p*-values for these correlations are slightly greater than p=0.05, the threshold for the 95% significance level, more data would help establish confidence in these relationships; it will be interesting to see if the results for the Phase II watersheds support these findings for the Phase I watersheds of the Santa Ana Mountains.

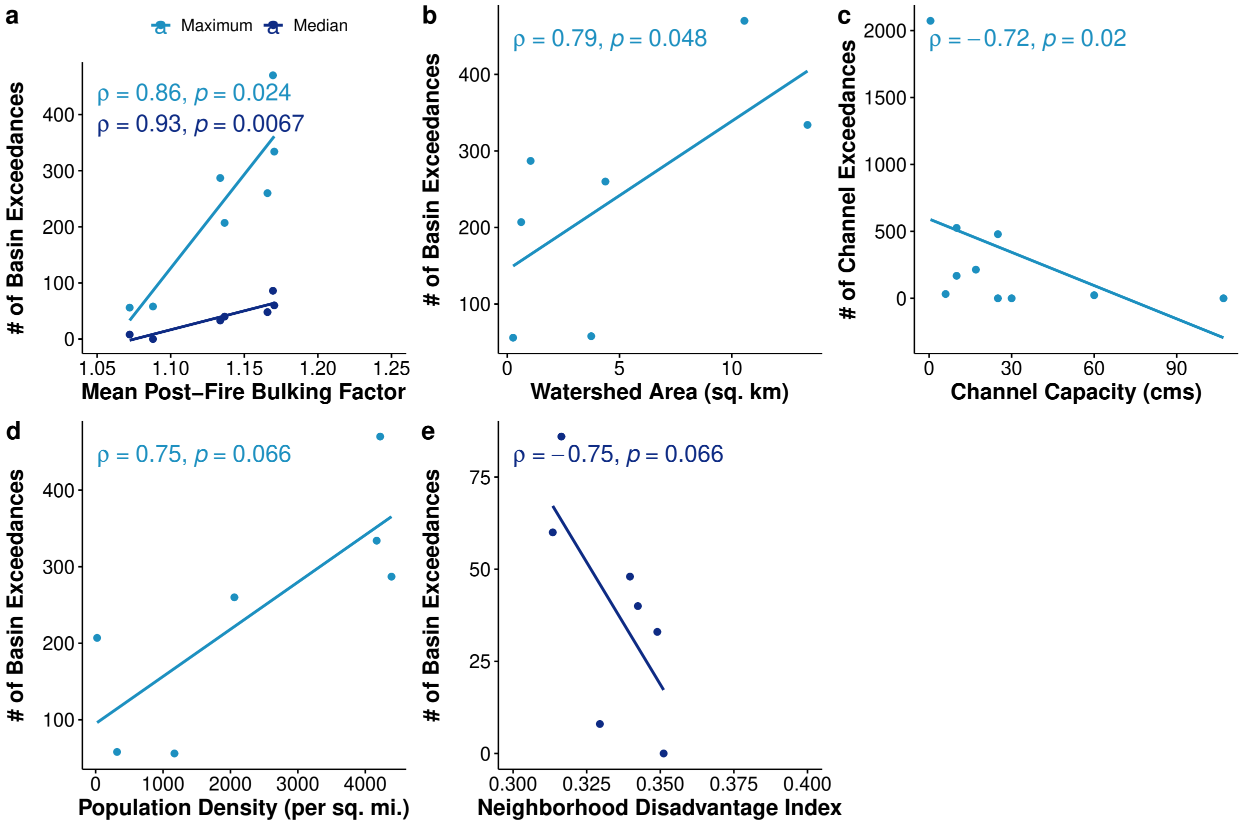

Figure 5.6: Correlations between explanatory variables and model response variables that were significant at the 90% confidence level. "Maximum" and "median" refer to the corresponding statistic used to summarize model outputs across simulation trials for each watershed (n=3,000).

.

Figure 5.7 compares the distributions of AEP based on the different types of infrastructure present at each study watershed. Interestingly, watersheds that have both types of infrastructure are not more protective against floods and actually have the highest median AEP compared to watersheds with only one type of infrastructure. This is almost certainly due to the influence of the Oak St. and Main St., which had the third and fourth highest AEPs across all the study sites. While there is great variability in the AEP distribution for watersheds with only flood channels, in general they tended to have a lower number of years with exceedances than did those with only debris basins. A Kruskal-Wallis Rank Sum Test and subsequent Pairwise Wilcoxon Rank Sum Test conducted using the R programming language finds that the medians of the distributions are significantly different from one another ($p < 0.001$). That said, it is important to keep in mind that the sample sizes for each infrastructure group are small for this set of Phase I watersheds; hazard estimates from additional Phase II watersheds will help determine whether these results hold true across the region.

The distributions of the number of channel exceedances per century for lined versus unlined channels are shown in Figure 5.8. As expected, the median number of channel exceedances is greater for unlined channels, likely owing to the much higher number of channel exceedances for the unlined channels of Greenwood Dr. and Indian. A Wilcoxon Rank Sum Test performed in R found that the medians of the distributions are significantly different ($p < 0.001$). There is no consistent trend in channel capacity with channel type other than that there is a large range of channel capacities among unlined channels (0.5 cms to 107 cms).

5.4 Discussion and Conclusions

The preceding results highlight multiple hotspots of sediment-laden flood risks among canyons in the Santa Ana Mountains. The Oak St. and Main St. watersheds represent large drainage areas ($\sim$10 km^2) with relatively high bulking factors upstream of densely populated areas

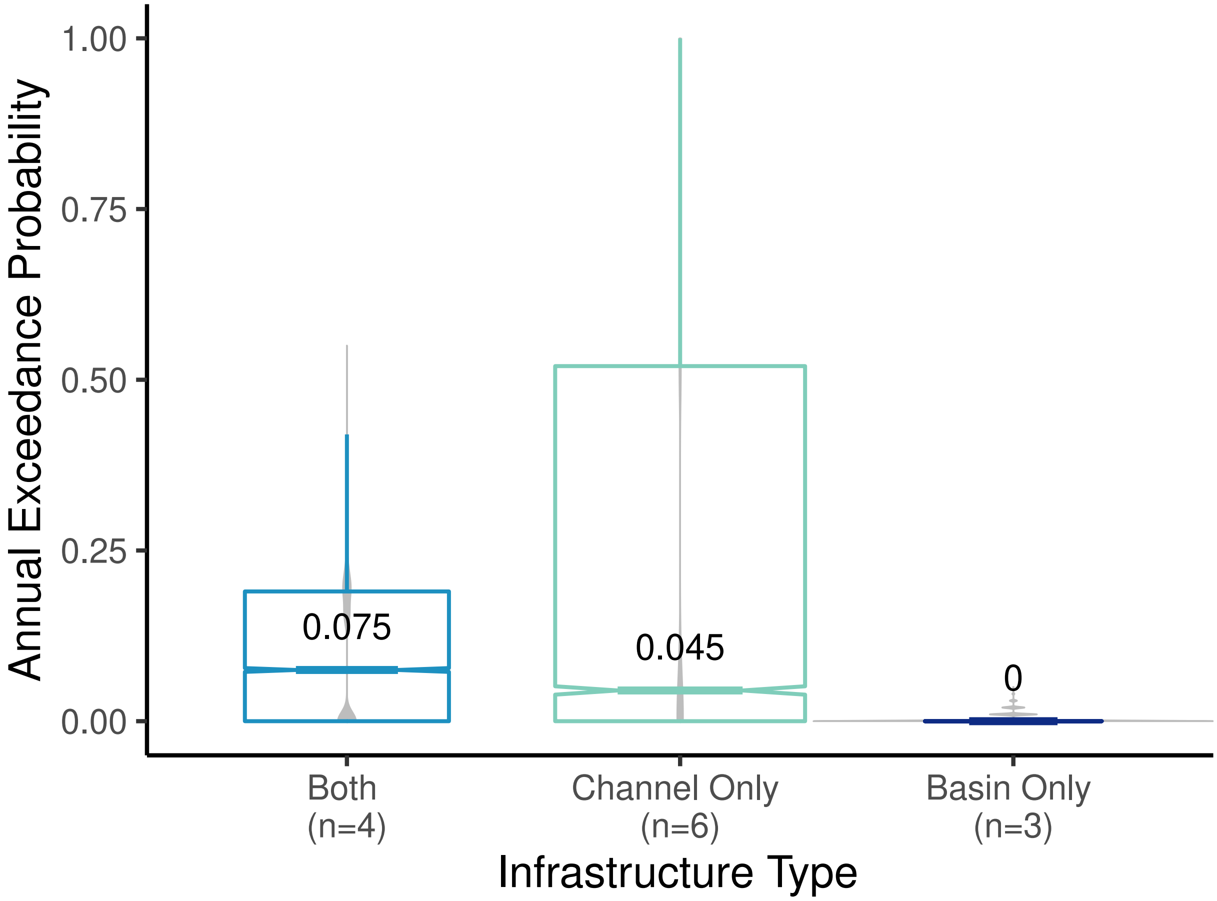

Figure 5.7: Distributions of annual exceedance probability for watersheds with both a flood channel and a debris basin (n=4), only a flood channel (n=6), and only a debris basin (n=3). Numbers represent medians.

.

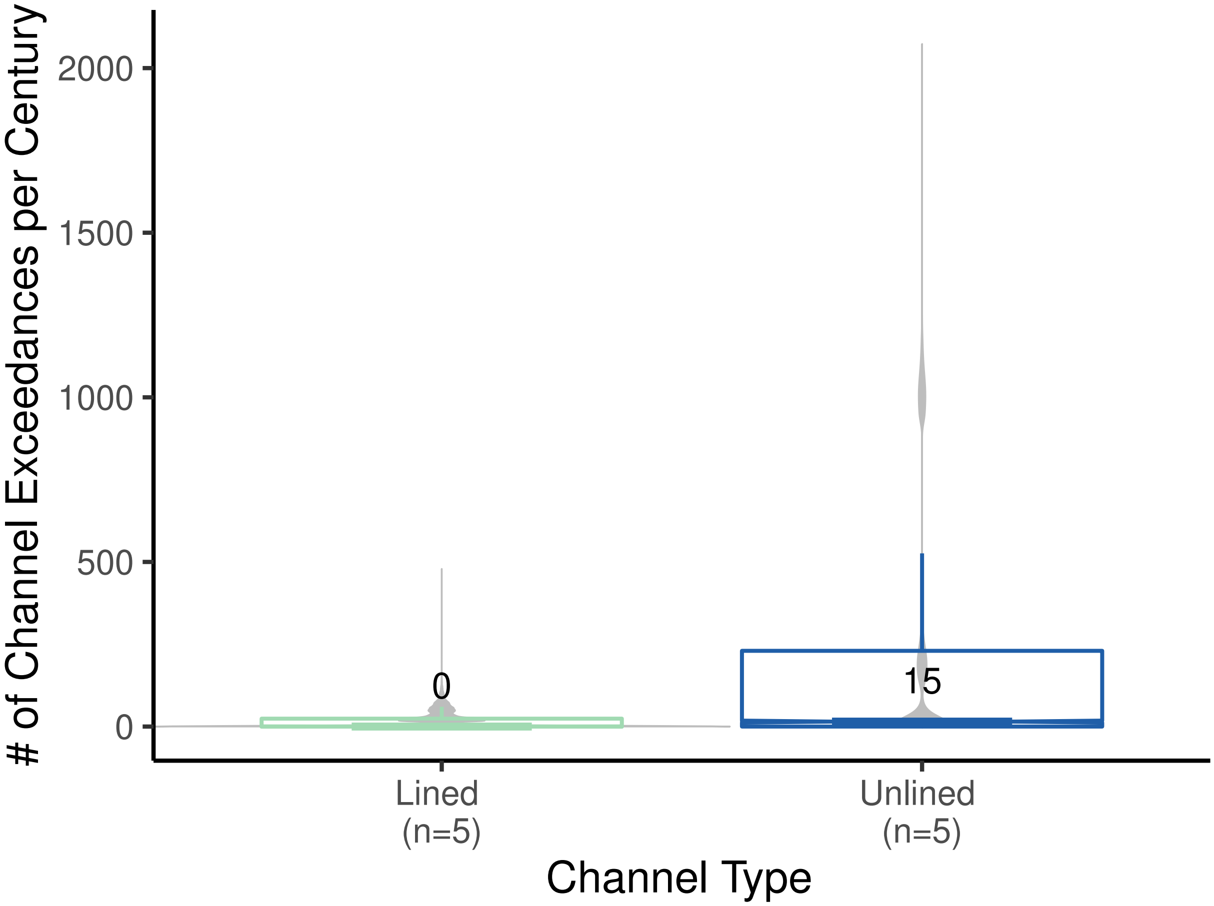

Figure 5.8: Distributions of number of channel exceedances per century for lined (n=5) and unlined (n=5) flood channels. Numbers represent medians.

.

that exhibit the greatest simulated number of debris basin exceedances as well as channel AEPs with return periods that correspond to approximately 5 years. According to historical fire perimeter data, these watersheds have not burned since 1977 and 1960, respectively, and this modeling study shows that the clogging of flood infrastructure during post-fire storms could result in severe flooding problems. Despite the fact that the populations downstream of Oak St. and Main St. watersheds are protected by both concrete-lined flood channels and debris basins, the estimated flood hazards for these areas are some of the highest along the Santa Ana Mountains.

AEPs predicted for Greenwood Dr. may appear unrealistically high (median of 0.98), however flooding issues have been documented for this channel in the past. The majority of the watershed area was burned by the Holy Fire, and during the first wet season following the fire, field teams from Riverside County observed hyperconcentrated flows in the channel and overtopping or imminent overtopping at least twice near the watershed outlet and once at a downstream culvert that impacted a major road (117). Flood complaint data provided by Riverside County shows there were approximately 25 flood complaints made within 0.5 km^2 of the channel since 1968. Dickey Canyon, which had the sixth highest estimated channel exceedances, also burned in the Holy Fire; sediment buildup in the flood channel and overtopping at a culvert was observed during the 2018-19 wet season. For comparison, only nine flood complaints have been made within 0.5 km^2 of Dickey Canyon Channel since 1986. Further, the Greenwood Dr. had a channel capacity of only 0.5 cms, which is two orders of magnitude lower than the median channel capacity of all watersheds with channels, 21 cms. We estimated the channel capacity for Greenwood Dr. using a fine-resolution DEM (0.46 m) and an upscale factor of 2, leading to an effective terrain resolution of 1 m; this should be sufficient to resolve a channel about 3 m in width. The correlation between channel capacity and the number of channel exceedances shown in Figure 5.6c leads to the conclusion that a small channel capacity is the main reason why the AEP of Greenwood Dr. was so high.

Lastly, Indian watershed, which had the second highest median AEP, likely has such a high potential for sediment-laden floods due to a combination of factors. It has the third lowest channel capacity, and also has a relatively large drainage area and bulking factor. For comparison, Rice had the fifth highest median AEP and has the same channel capacity as that of Indian (10 cms). However, the drainage area of Indian is almost twice that of Rice (8.36 vs. 4.98 km^2) and its mean bulking factor is higher (0.17 vs. 0.13, Table C.1). A greater drainage area translates to greater peak discharge, while a higher bulking factor translates to greater sediment fluxes from the watershed. Additionally, Indian has the second lowest fire return interval across study watersheds, which entails greater sediment fluxes due to a greater fire frequency. It is this confluence of drivers that leads to the relatively high flood risk downstream of Indian watershed.

This study highlighted the challenge of quantifying channel capacity for unlined flood channels, such as that of Rice Canyon, which could be categorized as more of an informal "flow path" than a flood channel. Since the natural channel was not deep in many reaches and since its banks were not well defined, the PRIMo modeling showed that flood flows left the main channel even at a relatively low flow rate. Thus, the characterization of flood channel capacity is more nuanced and involves more uncertainty than that for lined channels, and this uncertainty should be taken into account when interpreting simulation results for the number of channel exceedances and related variables. Future work could develop a method to quantify the uncertainty of channel capacity estimates of unlined channels, as well as consider the impact of heavy vegetation growing in channels, which often occurs when maintenance funding lapses or there are no major floods for several years. Moreover, development immediately downstream of Rice Canyon began in 2020, and the construction of a levee near the watershed outlet has been proposed to protect the new community (118). Modeling studies such as this one could be beneficial to inform the design of flood infrastructure such as levees considering the risk of sediment-laden flows after wildfires.

In conclusion, the present study demonstrates the regional application of PFHazMo across watersheds in the Santa Ana Mountains to produce a spatial distribution of post-fire, sediment-laden flood hazard estimates. The hazard modeling identifies hotspots of flood risk near narrow, unlined channels as expected, but also downstream of infrastructure systems with formal debris basins and concrete-lined flood channels. Correlation analysis reveals that flood channel exceedances are negatively correlated with channel capacity, debris basin exceedances are positively correlated with the mean post-fire bulking factor, and basin exceedances may be correlated with population density in communities downstream of infrastructure. Future work to apply PF2HazMo to 16 additional watersheds will shed more light on the key drivers and management implications of the spatial distribution of sediment-flood hazards across Riverside County.

Chapter 6

Conclusions and Future Work

The geographic distribution of near-mountain, sediment-laden flood hazards is not well understood compared to that of fluvial and coastal flood hazards. Increasingly, large segments of the population are becoming exposed to sediment-laden floods due to increases in wildfire frequency and severity, the frequency of extreme precipitation, and urban development at the wildland-urban interface. This dissertation develops an original modeling framework, PF2HazMo, that captures the interconnected influences of wildfire, storms, and flood infrastructure on post-fire, sediment-laden floods. For the first time, a spatial distribution of post-fire flood risk can be quantified for populations downstream of watersheds that span an entire mountain range. The stochastic treatment of variables such as precipitation and wildfires allows for the quantification of uncertainty and comparison of alternative climate and management scenarios, while the continuous simulation approach accounts for antecedent conditions and enables the calculation of hazard statistics over long planning horizons. Estimates of sediment-laden flooding can be used to create maps to raise awareness of compound post-fire flood risks and facilitate stakeholder engagement in flood risk management. Simulations from PF2HazMo can also inform the placement, design, and maintenance approaches for flood infrastructure by accounting for the hazard amplification caused by post-fire erosion.

The development of this new modeling framework and the lessons learned from its application to multiple watersheds have laid the foundation for future work. In Chapter 3, I discussed the fact that the impact of short-duration, high-intensity rainfall on peak bulked flows is not currently resolved well by the model due to the use of a daily timestep. Short-duration, high-intensity rainfall has been shown to be important for generating post-fire debris flows and hyperconcentrated flows as well as generating watershed-scale erosion (68; 69; 164; 139; 140). Future modeling studies could focus developing the capability to reduce the timestep only on days when precipitation is simulated to occur such that sub-hourly rainfall can be resolved while also keeping compute times relatively low, even for multidecadal simulation durations.

Moreover, Chapter 4 simulated the amplication of flood hazards under scenarios of increased wildfire frequency and severity. The next logical step is to examine the effect of the increased frequency of precipitation extremes based on regional climate projections. This can be accomplished by adjusting the mean and variance of the precipitation probability distribution used to calibrate the stochastic rainfall generator. Further, given the importance of atmospheric rivers to the total annual rainfall in California and the fact that these intense, multi-day storms are responsible for much of the flood damages in the state, future work could simulate the effect of atmospheric rivers on sediment-laden flood hazards.

Lastly, once the regional application of PF2HazMo across Riverside County has been completed, the estimates of peak bulked flows and channel exceedance probabilities can be used to force 2D simulations of street-level, sediment-laden flooding. This spatially distributed, fine-resolution quantification of downstream impacts does not currently exist and would not only support the needs of flood risk managers, but also provide a pathway for stakeholders to learn about their own post-fire flood risk and participate in flood risk management efforts. The spatially distributed, multi-decadal sediment-laden flood estimates produced with PF2HazMo will enable the forward-thinking emergency planning, sustainable land development, and stakeholder engagement needed to protect southern Californians from floods while ensuring resilient adaptation to the new hazards landscape.

Bibliography

[1] Adane, G. B., Hirpa, B. A., Lim, C.-H., and Lee, W.-K. (2020). Spatial and temporal analysis of dry and wet spells in upper awash river basin, ethiopia. *Water*, 12(11):3051.

[2] Anderson, M. G., Holcombe, E., Holm-Nielsen, N., and Della Monica, R. (2014). What are the emerging challenges for community-based landslide risk reduction in developing countries? *Natural Hazards Review*, 15(2):128–139.

[3] Andreadis, K. M., Wing, O. E., Colven, E., Gleason, C. J., Bates, P. D., and Brown, C. M. (2022). Urbanizing the floodplain: global changes of imperviousness in flood-prone areas. *Environmental Research Letters*, 17(10):104024.

[4] Armanini, A., Fraccarollo, L., and Rosatti, G. (2009). Two-dimensional simulation of debris flows in erodible channels. *Computers & Geosciences*, 35(5):993–1006.

[5] BAER (2021). Burned Area Reflectance Classification (BARC) products. Available online at `https://burnseverity.cr.usgs.gov/baer/baer-imagery-support-data-download`. [Data Set].

[6] Bates, P. D., Quinn, N., Sampson, C., Smith, A., Wing, O., Sosa, J., Savage, J., Olcese, G., Neal, J., Schumann, G., et al. (2021). Combined modeling of us fluvial, pluvial, and coastal flood hazard under current and future climates. *Water Resources Research*, 57(2):e2020WR028673.

[7] Beck, H. E., Zimmermann, N. E., McVicar, T. R., Vergopolan, N., Berg, A., and Wood, E. F. (2018). Present and future köppen-geiger climate classification maps at 1-km resolution. *Scientific data*, 5(1):1–12.

[8] Bedsworth, L., Cayan, D., Franco, G., Fisher, L., and Ziaja, S. (2018). California's fourth climate change assessment: Statewide summary report. *Publication number: SUM-CCCA4-2018-013.*

[9] Boughton, W. and Droop, O. (2003). Continuous simulation for design flood estimation—a review. *Environmental Modelling & Software*, 18(4):309–318.

[10] Brand, M. W., Gudiño-Elizondo, N., Allaire, M., Wright, S., Matson, W., Saksa, P., and Sanders, B. F. (2020). Stochastic hydro-financial watershed modeling for environmental impact bonds. *Water Resources Research*, 56(8):e2020WR027328.

[11] Brunner, M. I., Swain, D. L., Wood, R. R., Willkofer, F., Done, J. M., Gilleland, E., and Ludwig, R. (2021). An extremeness threshold determines the regional response of floods to changes in rainfall extremes. *Communications Earth & Environment*, 2(1):1–11.

[12] Byun, K. and Hamlet, A. F. (2020). A risk-based analytical framework for quantifying non-stationary flood risks and establishing infrastructure design standards in a changing environment. *Journal of Hydrology*, 584:124575.

[13] CAL FIRE (2021). Historic fire perimeter data. `https://www.fire.ca.gov/what-we-do/fire-resource-assessment-program/fire-perimeters`.

[14] California Geological Survey (2018). *Geology of California*. Retrieved from Retrieved from `https://www.conservation.ca.gov/cgs/Documents/Publications/Map-Sheets/MS_057-2018-Geology-of-California.pdf`.

[15] Cannon, S. H. and DeGraff, J. (2009). The increasing wildfire and post-fire debris-flow threat in western usa, and implications for consequences of climate change. In *Landslides–disaster risk reduction*, pages 177–190. Springer.

[16] Cannon, S. H., Gartner, J. E., Rupert, M. G., Michael, J. A., Rea, A. H., and Parrett, C. (2010). Predicting the probability and volume of postwildfire debris flows in the intermountain western united states. *Bulletin*, 122(1-2):127–144.

[17] Cannon, S. H., Gartner, J. E., Wilson, R. C., Bowers, J. C., and Laber, J. L. (2008). Storm rainfall conditions for floods and debris flows from recently burned areas in southwestern colorado and southern california. *Geomorphology*, 96(3-4):250–269.

[18] Carra, B. G., Bombino, G., Lucas-Borja, M. E., Denisi, P., Plaza-Álvarez, P. A., and Zema, D. A. (2021). Modelling the event-based hydrological response of mediterranean forests to prescribed fire and soil mulching with fern using the curve number, horton and usle-family (universal soil loss equation) models. *Land*, 10(11):1166.

[19] Castleman, T., Smith, H., and Toohey, G. (2023). Tracking the deaths from california's winter storms: At least 22 killed. *The Los Angeles Times*.

[20] Cerdà, A. and Doerr, S. H. (2005). Influence of vegetation recovery on soil hydrology and erodibility following fire: an 11-year investigation. *International Journal of Wildland Fire*, 14(4):423–437.

[21] Cerrelli, G. (2005). Fire hydro: A simplified method for predicting peak discharges to assist in the design of flood protection measures for western wildfires. In *Managing Watersheds for Human and Natural Impacts: Engineering, Ecological, and Economic Challenges*, pages 1–7.

[22] CGS (2023). Personal communication. California Geological Survey.

[23] Chen, L., Berli, M., and Chief, K. (2013). Examining modeling approaches for the rainfall-runoff process in wildfire-affected watersheds: Using san dimas experimental forest. *JAWRA Journal of the American Water Resources Association*, 49(4):851–866.

[24] Chen, X., Vogelmann, J. E., Rollins, M., Ohlen, D., Key, C. H., Yang, L., Huang, C., and Shi, H. (2011). Detecting post-fire burn severity and vegetation recovery using multitemporal remote sensing spectral indices and field-collected composite burn index data in a ponderosa pine forest. *International Journal of Remote Sensing*, 32(23):7905–7927.

[25] Chow, V. T. (1959). *Open-Channel Hydraulics*. McGraw-Hill, New York, NY.

[26] Christen, M., Kowalski, J., and Bartelt, P. (2010). Ramms: Numerical simulation of dense snow avalanches in three-dimensional terrain. *Cold Regions Science and Technology*, 63(1-2):1–14.

[27] Cutter, S. L., Emrich, C. T., Gall, M., and Reeves, R. (2018). Flash flood risk and the paradox of urban development. *Natural Hazards Review*, 19(1):05017005.

[28] Dennison, P. E., Brewer, S. C., Arnold, J. D., and Moritz, M. A. (2014). Large wildfire trends in the western united states, 1984–2011. *Geophysical Research Letters*, 41(8):2928–2933.

[29] Dewitz, J. (2021). National Land Cover Database (NLCD) 2019 Products. `https://doi.org/10.5066/P9KZCM54`. [Data Set].

[30] ESRI (2021). *ArcMap 10.8.2*. Environmental Systems Research Institute, Redlands, CA.

[31] FEMA (2008). Flood Insurance Study: Riverside County, California. Technical Report 06065CV001A, Federal Emergency Management Agency, Washington D.C.

[32] Finney, M. A. (2005). The challenge of quantitative risk analysis for wildland fire. *Forest Ecology and Management*, 211(1-2):97–108.

[33] Flanagan, D. and Nearing, M. (1995). Usda-water erosion prediction project: Hillslope profile and watershed model documentation. *Nserl Rep*, 10:1–123.

[34] Gallegos, H. A., Schubert, J. E., and Sanders, B. F. (2009). Two-dimensional, high-resolution modeling of urban dam-break flooding: A case study of baldwin hills, california. *Advances in water resources*, 32(8):1323–1335.

[35] Gao, P., Terando, A. J., Kupfer, J. A., Varner, J. M., Stambaugh, M. C., Lei, T. L., and Hiers, J. K. (2021). Robust projections of future fire probability for the conterminous united states. *Science of the total environment*, 789:147872.

[36] Gardner, R., O'neill, R., Mankin, J., and Carney, J. (1981). A comparison of sensitivity analysis and error analysis based on a stream ecosystem model. *Ecological Modelling*, 12(3):173–190.

[37] Garrison, J. D. and Huxman, T. E. (2020). A tale of two suburbias: Turning up the heat in southern california's flammable wildland-urban interface. *Cities*, 104:102725.

[38] Gartner, J. E., Cannon, S. H., Helsel, D. R., and Bandurraga, M. (2009). Multivariate statistical models for predicting sediment yields from southern california watersheds. Technical report, Citeseer.

[39] Gartner, J. E., Cannon, S. H., and Santi, P. M. (2014). Empirical models for predicting volumes of sediment deposited by debris flows and sediment-laden floods in the transverse ranges of southern california. *Engineering Geology*, 176:45–56.

[40] Gatwood, E., Pedersen, J., and Casey, K. (2000). Los Angeles District method for prediction of debris yield. Technical report, USACE.

[41] Gershunov, A., Shulgina, T., Clemesha, R. E., Guirguis, K., Pierce, D. W., Dettinger, M. D., Lavers, D. A., Cayan, D. R., Polade, S. D., Kalansky, J., et al. (2019). Precipitation regime change in western north america: the role of atmospheric rivers. *Scientific reports*, 9(1):1–11.

[42] Goodrich, D., Burns, I., Unkrich, C., Semmens, D. J., Guertin, D., Hernandez, M., Yatheendradas, S., Kennedy, J. R., and Levick, L. R. (2012). KINEROS2/AGWA: model use, calibration, and validation. *Transactions of the ASABE*, 55(4):1561–1574.

[43] Goodrich, D., Canfield, H. E., Burns, I. S., Semmens, D., Miller, S., Hernandez, M., Levick, L., Guertin, D., and Kepner, W. (2005). Rapid post-fire hydrologic watershed assessment using the agwa gis-based hydrologic modeling tool. In *Managing watersheds for human and natural impacts: engineering, ecological, and economic challenges*, pages 1–12.

[44] Gotvald, A. J., Barth, N. A., Veilleux, A. G., Parrett, C., et al. (2012). Methods for determining magnitude and frequency of floods in california, based on data through water year 2006. *US Geological Survey Scientific Investigations Report*, 5113:38.

[45] Gouveia, C., DaCamara, C., and Trigo, R. (2010). Post-fire vegetation recovery in portugal based on spot/vegetation data. *Natural Hazards and Earth System Sciences*, 10(4):673–684.

[46] Gudino-Elizondo, N., Brand, M. W., Biggs, T. W., Hinojosa-Corona, A., Gómez-Gutiérrez, Á., Langendoen, E., Bingner, R., Yuan, Y., and Sanders, B. F. (2022). Rapid assessment of abrupt urban mega-gully and landslide events with structure-from-motion photogrammetric techniques validates link to water resources infrastructure failures in an urban periphery. *Natural Hazards and Earth System Sciences*, 22(2):523–538.

[47] Guilinger, James (2023). Personal communication.

[48] Gusman, A. J. (2011). Sediment/Debris Bulking Factors and Post-fire Hydrology for Ventura County. Technical report, WEST Consultants, Inc.

[49] Gusman, A. J. and Viducich, J. (2022). San Diego County hydrology manual technical studies: Bulking factor study. Technical report, River Focus, Inc.

[50] Hamby, D. M. (1994). A review of techniques for parameter sensitivity analysis of environmental models. *Environmental monitoring and assessment*, 32:135–154.

[51] Harrell Jr, F. E. and Harrell Jr, M. F. E. (2019). Package 'hmisc'. *CRAN2018*, 2019:235–236.

[52] Hawkins, R. and Munoz, A. (2011). Wildcat 5 for windows (w5w): Documentation an d manual. *University of Arizona, School of Natural Resources and Environment, Tucson, AZ*.

[53] Hope, A., Tague, C., and Clark, R. (2007). Characterizing post-fire vegetation recovery of california chaparral using tm/etm+ time-series data. *International Journal of Remote Sensing*, 28(6):1339–1354.

[54] Houston, D., Cheung, W., Basolo, V., Feldman, D., Matthew, R., Sanders, B. F., Karlin, B., Schubert, J. E., Goodrich, K. A., Contreras, S., et al. (2019). The influence of hazard maps and trust of flood controls on coastal flood spatial awareness and risk perception. *Environment and Behavior*, 51(4):347–375.

[55] Huang, X., Swain, D. L., and Hall, A. D. (2020). Future precipitation increase from very high resolution ensemble downscaling of extreme atmospheric river storms in california. *Science advances*, 6(29):eaba1323.

[56] Hutton, N. S., Tobin, G. A., and Montz, B. E. (2019). The levee effect revisited: Processes and policies enabling development in yuba county, california. *Journal of Flood Risk Management*, 12(3):e12469.

[57] Hyde, K. D., Riley, K., and Stoof, C. (2017). Uncertainties in predicting debris flow hazards following wildfire. *Natural hazard uncertainty assessment: modeling and decision support. Geophysical monograph*, 223:287–299.

[58] Hydrologic Engineering Center (2023a). Creating a curve number grid and computing subbasin average curve number values. `https://www.hec.usace.army.mil/confluence/hmsdocs/hmsguides/gis-tutorials-and-guides/creating-a-curve-number-grid-and-computing-subbasin-average-curve-number-values`.

[59] Hydrologic Engineering Center (2023b). Pre post wildfire hydrology modeling with hec-hms procedure. `https://www.hec.usace.army.mil/confluence/hmsdocs/hmsguides/hydrologic-modeling-and-debris-flow-estimation-for-post-wildfire-conditions/pre-post-wildfire-hydrology-modeling-with-hec-hms-procedure`.

[60] Inman, D. L. and Jenkins, S. A. (1999). Climate change and the episodicity of sediment flux of small california rivers. *The Journal of geology*, 107(3):251–270.

[61] Jackson, E. K., Roberts, W., Nelsen, B., Williams, G. P., Nelson, E. J., and Ames, D. P. (2019). Introductory overview: Error metrics for hydrologic modelling–a review of common practices and an open source library to facilitate use and adoption. *Environmental Modelling & Software*, 119:32–48.

[62] Jakob, M., Hungr, O., and Jakob, D. M. (2005). *Debris-flow hazards and related phenomena*, volume 739. Springer.

[63] Jennings, P. C., Brooks, N. H., et al. (1982). Storms, floods, and debris flows in southern california and arizona, 1978 and 1980: Proceedings of a symposium, september 17-18, 1980.

[64] Johnson, P. A. and McCuen, R. H. (1992). Effect of debris flows on debris basin design. *Critical Reviews in Environmental Science and Technology*, 22(1-2):137–149.

[65] Johnson, P. A., McCuen, R. H., and Hromadka, T. V. (1991). Debris basin policy and design. *Journal of hydrology*, 123(1-2):83–95.

[66] Jong-Levinger, A., Banerjee, T., Houston, D., and Sanders, B. F. (2022). Compound post-fire flood hazards considering infrastructure sedimentation. *Earth's Future*, 10(8):e2022EF002670.

[67] Kahl, D. T., Schubert, J. E., Jong-Levinger, A., and Sanders, B. F. (2022). Grid edge classification method to enhance levee resolution in dual-grid flood inundation models. *Advances in Water Resources*, 168:104287.

[68] Kampf, S. K., Brogan, D. J., Schmeer, S., MacDonald, L. H., and Nelson, P. A. (2016). How do geomorphic effects of rainfall vary with storm type and spatial scale in a post-fire landscape? *Geomorphology*, 273:39–51.

[69] Kampf, S. K., Gannon, B. M., Wilson, C., Saavedra, F., Miller, M. E., Heldmyer, A., Livneh, B., Nelson, P., and MacDonald, L. (2020). Pemip: Post-fire erosion model inter-comparison project. *Journal of Environmental Management*, 268:110704.

[70] Kean, J. W. and Staley, D. M. (2021). Forecasting the frequency and magnitude of postfire debris flows across southern california. *Earth's Future*, 9(3):e2020EF001735.

[71] Kent, K. M., Woodward, D. E., Hoeft, C. C., Humpal, A., and Cerrelli, G. (2010). *Chapter 15: Time of Concentration*, pages 15–i–15B–3. U.S. Department of Agriculture.

[72] Kinoshita, A. M. and Hogue, T. S. (2011). Spatial and temporal controls on post-fire hydrologic recovery in southern california watersheds. *Catena*, 87(2):240–252.

[73] Kinoshita, A. M., Hogue, T. S., and Napper, C. (2014). Evaluating pre-and post-fire peak discharge predictions across western us watersheds. *JAWRA Journal of the American Water Resources Association*, 50(6):1540–1557.

[74] Kirkby, M., Irvine, B., Jones, R. J., Govers, G., and Team, P. (2008). The pesera coarse scale erosion model for europe. i.–model rationale and implementation. *European Journal of Soil Science*, 59(6):1293–1306.

[75] Kroese, D. P., Brereton, T., Taimre, T., and Botev, Z. I. (2014). Why the monte carlo method is so important today. *Wiley Interdisciplinary Reviews: Computational Statistics*, 6(6):386–392.

[76] LACDPW (2006a). Hydrology Manual. Technical report, Los Angeles County Department of Public Works, Alhambra, California.

[77] LACDPW (2006b). Sedimentation Manual. Technical report, Los Angeles County Department of Public Works, Alhambra, California.

[78] LANDFIRE (2014). *Mean Fire Return Interval, LANDFIRE 1.4.0*. Wildland Fire Science, Earth Resources Observation and Science Center, U.S. Geological Survey. Accessed 11 May 2023 at `https://landfire.gov/viewer/`.

[79] Lavé, J. and Burbank, D. (2004). Denudation processes and rates in the transverse ranges, southern california: Erosional response of a transitional landscape to external and anthropogenic forcing. *Journal of Geophysical Research: Earth Surface*, 109(F1).

[80] Li, J., Cao, Z., Hu, K., Pender, G., and Liu, Q. (2018). A depth-averaged two-phase model for debris flows over erodible beds. *Earth Surface Processes and Landforms*, 43(4):817–839.

[81] Li, S. and Banerjee, T. (2021). Spatial and temporal pattern of wildfires in california from 2000 to 2019. *Scientific reports*, 11(1):1–17.

[82] Littell, J. S., Peterson, D. L., Riley, K. L., Liu, Y., and Luce, C. H. (2016). A review of the relationships between drought and forest fire in the united states. *Global change biology*, 22(7):2353–2369.

[83] Liu, K.-F. and Huang, M. C. (2006). Numerical simulation of debris flow with application on hazard area mapping. *Computational Geosciences*, 10(2):221–240.

[84] Livingston, R. K., Earles, T. A., and Wright, K. R. (2005). Los alamos post-fire watershed recovery: a curve-number-based evaluation. In *Managing Watersheds for Human and Natural Impacts: Engineering, Ecological, and Economic Challenges*, pages 1–11.

[85] Luke, A., Sanders, B. F., Goodrich, K. A., Feldman, D. L., Boudreau, D., Eguiarte, A., Serrano, K., Reyes, A., Schubert, J. E., AghaKouchak, A., et al. (2018). Going beyond the flood insurance rate map: insights from flood hazard map co-production. *Natural Hazards and Earth System Sciences*, 18(4):1097–1120.

[86] Luke, A., Vrugt, J. A., AghaKouchak, A., Matthew, R., and Sanders, B. F. (2017). Predicting nonstationary flood frequencies: Evidence supports an updated stationarity thesis in the united states. *Water Resources Research*, 53(7):5469–5494.

[87] Mahmoud, S. H. and Alazba, A. (2015). Hydrological response to land cover changes and human activities in arid regions using a geographic information system and remote sensing. *Plos one*, 10(4):e0125805.

[88] Majd, M. S. and Sanders, B. F. (2014). The lhllc scheme for two-layer and two-phase transcritical flows over a mobile bed with avalanching, wetting and drying. *Advances in water resources*, 67:16–31.

[89] Mallapaty, S. (2022). Why are pakistan's floods so extreme this year? *Nature*.

[90] Martínez-Aranda, S., Murillo, J., and García-Navarro, P. (2022). A gpu-accelerated efficient simulation tool (est) for 2d variable-density mud/debris flows over non-uniform erodible beds. *Engineering Geology*, 296:106462.

[91] Mayor, Á. G., Bautista, S., and Bellot, J. (2011). Scale-dependent variation in runoff and sediment yield in a semiarid mediterranean catchment. *Journal of Hydrology*, 397(1-2):128–135.

[92] Meyer, G. A. and Wells, S. G. (1997). Fire-related sedimentation events on alluvial fans, yellowstone national park, usa. *Journal of Sedimentary Research*, 67(5):776–791.

[93] Meyer, G. A., Wells, S. G., and Timothy Jull, A. (1995). Fire and alluvial chronology in yellowstone national park: climatic and intrinsic controls on holocene geomorphic processes. *Geological Society of America Bulletin*, 107(10):1211–1230.

[94] Mockus, V., Hjelmfelt, A. T., and Moody, H. F. (2004). *Chapter 10: Estimation of Direct Runoff from Storm Rainfall*, pages 10–i–10A–51. U.S. Department of Agriculture.

[95] Montz, B. E. and Tobin, G. A. (2008). Livin'large with levees: Lessons learned and lost. *Natural Hazards Review*, 9(3):150–157.

[96] Moody, J. A., Shakesby, R. A., Robichaud, P. R., Cannon, S. H., and Martin, D. A. (2013). Current research issues related to post-wildfire runoff and erosion processes. *Earth-Science Reviews*, 122:10–37.

[97] Nadal-Romero, E., Martínez-Murillo, J. F., Vanmaercke, M., and Poesen, J. (2011). Scale-dependency of sediment yield from badland areas in mediterranean environments. *Progress in Physical Geography*, 35(3):297–332.

[98] National Research Council (1996). *Alluvial fan flooding*. National Academies Press.

[NOAA] NOAA. Climate data online search. `https://www.ncdc.noaa.gov/cdo-web/datasets/GHCND/stations/GHCND:USC00040798/detail`. Accessed: 2022-01-06.

[100] O'Brien, J. S., Julien, P. Y., and Fullerton, W. (1993). Two-dimensional water flood and mudflow simulation. *Journal of hydraulic engineering*, 119(2):244–261.

[101] Osanai, N., Mizuno, H., Mizuyama, T., et al. (2010). Design standard of control structures against debris flow in japan. *Journal of Disaster Research*, 5(3):307–314.

[102] Pak, J. H. and Lee, J.-J. (2008). A statistical sediment yield prediction model incorporating the effect of fires and subsequent storm events 1. *JAWRA Journal of the American Water Resources Association*, 44(3):689–699.

[103] Parks, S. and Abatzoglou, J. (2020). Warmer and drier fire seasons contribute to increases in area burned at high severity in western us forests from 1985 to 2017. *Geophysical Research Letters*, 47(22):e2020GL089858.

[104] Pathiraja, S., Westra, S., and Sharma, A. (2012). Why continuous simulation? the role of antecedent moisture in design flood estimation. *Water Resources Research*, 48(6).

[105] Pelletier, J. D. and Orem, C. A. (2014). How do sediment yields from post-wildfire debris-laden flows depend on terrain slope, soil burn severity class, and drainage basin area? insights from airborne-lidar change detection. *Earth Surface Processes and Landforms*, 39(13):1822–1832.

[106] Perica, S., Dietz, S., Heim, S., Hiner, L., Maitaria, K., Martin, D., Pavlovic, S., Roy, I., Trypaluk, C., Unruh, D., et al. (2011). Precipitation-frequency atlas of the united states. volume 6 version 2.3. california.

[107] Pierson, T. C. (2005). Hyperconcentrated flow—transitional process between water flow and debris flow. In *Debris-flow hazards and related phenomena*, pages 159–202. Springer.

[108] Piton, G. and Recking, A. (2016). Design of sediment traps with open check dams. ii: woody debris. *Journal of Hydraulic Engineering*, 142(2):04015046.

[109] PRISM Climate Group (2023). Oregon State University. Accessed 23 May 2023 at `https://prism.oregonstate.edu`.

[110] Prochaska, A. B., Santi, P. M., and Higgins, J. D. (2008). Debris basin and deflection berm design for fire-related debris-flow mitigation. *Environmental & Engineering Geoscience*, 14(4):297–313.

[111] R Core Team (2021). *R: A Language and Environment for Statistical Computing.* R Foundation for Statistical Computing, Vienna, Austria.

[112] Radeloff, V. C., Helmers, D. P., Kramer, H. A., Mockrin, M. H., Alexandre, P. M., Bar-Massada, A., Butsic, V., Hawbaker, T. J., Martinuzzi, S., Syphard, A. D., et al. (2018). Rapid growth of the us wildland-urban interface raises wildfire risk. *Proceedings of the National Academy of Sciences*, 115(13):3314–3319.

[113] RCEPD (2003). *Santa Ana Mountains Bioregion: Volume 2 - Section 2.4.* Riverside County Environmental Programs Division.

[114] RCFCWCD (1978). Hydrology Manual. Technical report, Riverside County Flood Control and Water Conservation District.

[115] RCFCWCD (2019). Personal communication. Riverside County Flood Control and Water Conservation District.

[116] RCFCWCD (2021). Personal communication. Riverside County Flood Control and Water Conservation District.

[117] RCFCWCD (2022). Personal communication. Riverside County Flood Control and Water Conservation District.

[118] RCFCWCD (2023). Personal communication. Riverside County Flood Control and Water Conservation District.

[119] Renard, K. G. (1997). *Predicting soil erosion by water: a guide to conservation planning with the Revised Universal Soil Loss Equation (RUSLE)*. United States Government Printing.

[120] Rengers, F. K., McGuire, L. A., Kean, J. W., Staley, D. M., Dobre, M., Robichaud, P. R., and Swetnam, T. (2021). Movement of sediment through a burned landscape: Sediment volume observations and model comparisons in the san gabriel mountains, california, usa. *Journal of Geophysical Research: Earth Surface*, 126(7):e2020JF006053.

[121] Richardson, C. W. (1981). Stochastic simulation of daily precipitation, temperature, and solar radiation. *Water resources research*, 17(1):182–190.

[122] Rickenmann, D., Laigle, D., McArdell, B., and Hübl, J. (2006). Comparison of 2d debris-flow simulation models with field events. *Computational Geosciences*, 10(2):241–264.

[123] Rollins, M. G. (2009). Landfire: a nationally consistent vegetation, wildland fire, and fuel assessment. *International Journal of Wildland Fire*, 18(3):235–249.

[124] Rosatti, G. and Begnudelli, L. (2013). Two-dimensional simulation of debris flows over mobile bed: Enhancing the trent2d model by using a well-balanced generalized roe-type solver. *Computers & fluids*, 71:179–195.

[125] Rowe, P. B., Countryman, O., and Storey, H. (1949). *Probable peak discharges and erosion rates from southern California watersheds as influenced by fire*. US Department of Agriculture, Forest Service.

[126] Sadegh, M., Moftakhari, H., Gupta, H. V., Ragno, E., Mazdiyasni, O., Sanders, B., Matthew, R., and AghaKouchak, A. (2018). Multihazard scenarios for analysis of compound extreme events. *Geophysical Research Letters*, 45(11):5470–5480.

[127] Sanders, B. F. and Grant, S. B. (2020). Re-envisioning stormwater infrastructure for ultrahazardous flooding. *Wiley Interdisciplinary Reviews: Water*, 7(2):e1414.

[128] Sanders, B. F. and Schubert, J. E. (2019). Primo: Parallel raster inundation model. *Advances in Water Resources*, 126:79–95.

[129] Sanders, B. F., Schubert, J. E., Goodrich, K. A., Houston, D., Feldman, D. L., Basolo, V., Luke, A., Boudreau, D., Karlin, B., Cheung, W., et al. (2020). Collaborative modeling with fine-resolution data enhances flood awareness, minimizes differences in flood perception, and produces actionable flood maps. *Earth's Future*, 8(1):e2019EF001391.

[130] Sanders, B. F., Schubert, J. E., Kahl, D. T., Mach, K. J., Brady, D., AghaKouchak, A., Forman, F., Matthew, R. A., Ulibarri, N., and Davis, S. J. (2023). Large and inequitable flood risks in los angeles, california. *Nature sustainability*, 6(1):47–57.

[131] Saxe, S., Hogue, T. S., and Hay, L. (2018). Characterization and evaluation of controls on post-fire streamflow response across western us watersheds. *Hydrology and Earth System Sciences*, 22(2):1221–1237.

[132] Scott, K. M., Williams, R. P., et al. (1978). *Erosion and sediment yields in the Transverse Ranges, southern California*, volume 1030. US Government Printing Office.

[133] Shahraki, N., Bakhtiari, B., and Ahmadi, M. (2013). Markov chain model for probability of dry, wet days and statistical analysis of daily rainfall in some climatic zone of iran. *Aerul si Apa: Compon. ale Mediului*, 4:399–416.

[134] Shakesby, R. (2011). Post-wildfire soil erosion in the mediterranean: review and future research directions. *Earth-Science Reviews*, 105(3-4):71–100.

[135] Sharma, M. A. and Singh, J. B. (2010). Use of probability distribution in rainfall analysis. *New York Science Journal*, 3(9):40–49.

[136] Snider, D., Woodward, D. E., Hoeft, C. C., Merkel, W. H., Chaison, K. E., and Moody, H. F. (2007). *Chapter 16: Hydrographs*, pages 116–i–16B–13. U.S. Department of Agriculture.

[137] Soil Survey Staff (2023). Web soil survey. Available online at `https://websoilsurvey.nrcs.usda.gov/`. [Data Set].

[138] Soulis, K. X. (2018). Estimation of scs curve number variation following forest fires. *Hydrological Sciences Journal*, 63(9):1332–1346.

[139] Staley, D. M., Kean, J. W., Cannon, S. H., Schmidt, K. M., and Laber, J. L. (2013). Objective definition of rainfall intensity–duration thresholds for the initiation of post-fire debris flows in southern california. *Landslides*, 10(5):547–562.

[140] Staley, D. M., Negri, J. A., Kean, J. W., Laber, J. L., Tillery, A. C., and Youberg, A. M. (2017). Prediction of spatially explicit rainfall intensity–duration thresholds for post-fire debris-flow generation in the western united states. *Geomorphology*, 278:149–162.

[141] Stern, R. and Coe, R. (1984). A model fitting analysis of daily rainfall data. *Journal of the Royal Statistical Society: Series A (General)*, 147(1):1–18.

[142] Storey, E. A., Stow, D. A., O'Leary, J. F., Davis, F. W., and Roberts, D. A. (2021). Does short-interval fire inhibit postfire recovery of chaparral across southern california? *Science of the Total Environment*, 751:142271.

[143] Sumeet, M., Yatnesh, B., Shri, K., Gaurav, S., Nema, A., et al. (2013). Markov chain model probability of dry wet weeks and statistical analysis of weekly rainfall for agricultural planning at jabalpur. *Environment and Ecology*, 31(3):1250–1254.

[144] Swain, D. L., Langenbrunner, B., Neelin, J. D., and Hall, A. (2018). Increasing precipitation volatility in twenty-first-century california. *Nature Climate Change*, 8(5):427–433.

[145] Tate, E., Rahman, M. A., Emrich, C. T., and Sampson, C. C. (2021). Flood exposure and social vulnerability in the united states. *Natural Hazards*, 106(1):435–457.

[146] Thornton, P. E., Shrestha, R., Thornton, M., Kao, S.-C., Wei, Y., and Wilson, B. E. (2021). Gridded daily weather data for north america with comprehensive uncertainty quantification. *Scientific Data*, 8(1):190.

[147] Touma, D., Stevenson, S., Swain, D. L., Singh, D., Kalashnikov, D. A., and Huang, X. (2022). Climate change increases risk of extreme rainfall following wildfire in the western united states. *Science advances*, 8(13):eabm0320.

[148] U.S. Army Corps of Engineers (2022). *Hydrologic Modeling System HEC-HMS User's Manual version 4.10*. Institute for Water Resources Hydrologic Engineering Center, Davis, California.

[149] U.S. Census Bureau (2022). American Community Survey 2016-2020 5-year data. `https://www2.census.gov/programs-surveys/acs/summary_file/2020/`. Accessed: 2023-06-16.

[150] USDA (2009). Small watershed hydrology: Wintr-55 user guide.

[151] USDA Forest Service (2012). Fire return interval in CA, 1908-2012. `https://www.sciencebase.gov/catalog/item/563be0fbe4b0d6133fe76016`. Accessed: 2021-10-12.

[152] USGS (2019a). 3D elevation program 10-meter resolution digital elevation model. `https://www.usgs.gov/the-national-map-data-delivery`. Accessed: 2023-05-20.

[153] USGS (2019b). The StreamStats program. `https://streamstats.usgs.gov/ss/`. Accessed: 2023-04-26.

[154] USGS (2020). USGS one meter SoCal Wildfires B1 2018. `https://www.usgs.gov/the-national-map-data-delivery`. Accessed: 2022-09-23.

[155] Vahedifard, F., AghaKouchak, A., Ragno, E., Shahrokhabadi, S., and Mallakpour, I. (2017). Lessons from the oroville dam. *Science*, 355(6330):1139–1140.

[156] Van Eck, C. M., Nunes, J. P., Vieira, D. C., Keesstra, S., and Keizer, J. J. (2016). Physically-based modelling of the post-fire runoff response of a forest catchment in central portugal: using field versus remote sensing based estimates of vegetation recovery. *Land degradation & development*, 27(5):1535–1544.

[157] Van Leeuwen, W. J. (2008). Monitoring the effects of forest restoration treatments on post-fire vegetation recovery with modis multitemporal data. *Sensors*, 8(3):2017–2042.

[158] VCWPD (2005). Debris and Detention Basins. Technical report, Ventura County Watershed Protection District.

[159] VCWPD (2017). Design Hydrology Manual. Technical report, Ventura County Watershed Protection District.

[160] Vieira, D., Fernández, C., Vega, J., and Keizer, J. (2015). Does soil burn severity affect the post-fire runoff and interrill erosion response? a review based on meta-analysis of field rainfall simulation data. *Journal of Hydrology*, 523:452–464.

[161] Vieira, F. M. C., Machado, J. M. C., de Souza Vismara, E., and Possenti, J. C. (2018). Probability distributions of frequency analysis of rainfall at the southwest region of paraná state, brazil. *Revista de Ciências Agroveterinárias*, 17(2):260–266.

[162] Vogel, R. M. (2017). Stochastic watershed models for hydrologic risk management. *Water Security*, 1:28–35.

[163] Wagenbrenner, J. W., Ebel, B. A., Bladon, K. D., and Kinoshita, A. M. (2021). Post-wildfire hydrologic recovery in mediterranean climates: A systematic review and case study to identify current knowledge and opportunities. *Journal of Hydrology*, 602:126772.

[164] Wagenbrenner, J. W. and Robichaud, P. R. (2014). Post-fire bedload sediment delivery across spatial scales in the interior western united states. *Earth Surface Processes and Landforms*, 39(7):865–876.

[165] Wahl, T., Haigh, I. D., Nicholls, R. J., Arns, A., Dangendorf, S., Hinkel, J., and Slangen, A. B. (2017). Understanding extreme sea levels for broad-scale coastal impact and adaptation analysis. *Nature communications*, 8(1):1–12.

[166] Wallerstein, N., Thorne, C. R., and Abt, S. R. (1997). Debris control at hydraulic structures in selected areas of the united states and europe.

[167] Wang, J., Stern, M. A., King, V. M., Alpers, C. N., Quinn, N. W., Flint, A. L., and Flint, L. E. (2020). Pfhydro: a new watershed-scale model for post-fire runoff simulation. *Environmental Modelling & Software*, 123:104555.

[168] Westerling, A. L., Hidalgo, H. G., Cayan, D. R., and Swetnam, T. W. (2006). Warming and earlier spring increase western us forest wildfire activity. *science*, 313(5789):940–943.

[169] White, G. F. (1942). *Human adjustment to floods: a geographical approach to the flood problem in the United States.* PhD thesis, The University of Chicago.

[170] Wilder, B. A. and Kinoshita, A. M. (2022). Incorporating ecostress evapotranspiration in a paired catchment water balance analysis after the 2018 holy fire in california. *Catena*, 215:106300.

[171] Wilder, B. A., Lancaster, J. T., Cafferata, P. H., Coe, D. B., Swanson, B. J., Lindsay, D. N., Short, W. R., and Kinoshita, A. M. (2021). An analytical solution for rapidly predicting post-fire peak streamflow for small watersheds in southern california. *Hydrological Processes*, 35(1):e13976.

[172] Wilks, D. (1998). Multisite generalization of a daily stochastic precipitation generation model. *journal of Hydrology*, 210(1-4):178–191.

[173] Willardson, B. (2020). Sustainable debris basins for post-fire protection. In *2020 Intermountain Engineering, Technology and Computing (IETC)*, pages 1–6. IEEE.

[174] Williams, C. J., Pierson, F. B., Robichaud, P. R., and Boll, J. (2014). Hydrologic and erosion responses to wildfire along the rangeland–xeric forest continuum in the western us: a review and model of hydrologic vulnerability. *International Journal of Wildland Fire*, 23(2):155–172.

[175] Winter, B., Schneeberger, K., Dung, N., Huttenlau, M., Achleitner, S., Stötter, J., Merz, B., and Vorogushyn, S. (2019). A continuous modelling approach for design flood estimation on sub-daily time scale. *Hydrological Sciences Journal*, 64(5):539–554.

[176] Wischmeier, W. H., Smith, D. D., et al. (1965). Predicting rainfall-erosion losses from cropland east of the rocky mountains.

[177] Wittenberg, L., Malkinson, D., Beeri, O., Halutzy, A., and Tesler, N. (2007). Spatial and temporal patterns of vegetation recovery following sequences of forest fires in a mediterranean landscape, mt. carmel israel. *Catena*, 71(1):76–83.

[178] Ye, L., Hanson, L. S., Ding, P., Wang, D., and Vogel, R. M. (2018). The probability distribution of daily precipitation at the point and catchment scales in the united states. *Hydrology and Earth System Sciences*, 22(12):6519–6531.

Appendix A

Supporting Information for Chapter 2

This supporting information contains figures that were used to develop the Monte Carlo Markov Chain (MCMC) rainfall simulator (Figures A.1-A.3), determine return levels of precipitation used to size infrastructure (Figure A.4), and analyze model sensitivity to watershed area (Figure A.5). It also contains a table (Table A.1) that compares the summary statistics of the precipitation record used to calibrate the MCMC rainfall simulator and those of 100 rainfall simulations to ensure the statistical properties of the observed and synthetic time series were similar.

Table A.1: Comparison of summary statistics between observed and synthetic daily precipitation time series[a]

Statistic	Observed (mm)	Synthetic (mm)	Observed: Non-zero (mm)	Synthetic: Non-zero (mm)
Sample Size	28,806	3,102,500	3,065	322,154
Mean	1.84	1.72	17.3	16.6
Standard Deviation	10.6	9.47	28.1	24.9
Skewness	11.7	11.2	4.09	3.98

[a] Observed time series consisted of 85 years of daily data with approximately 7% missing values. Summary statistics for synthetic precipitation represent 100 realizations of an 85-year time series (1 year = 365 days). Skewness was not bias-corrected.

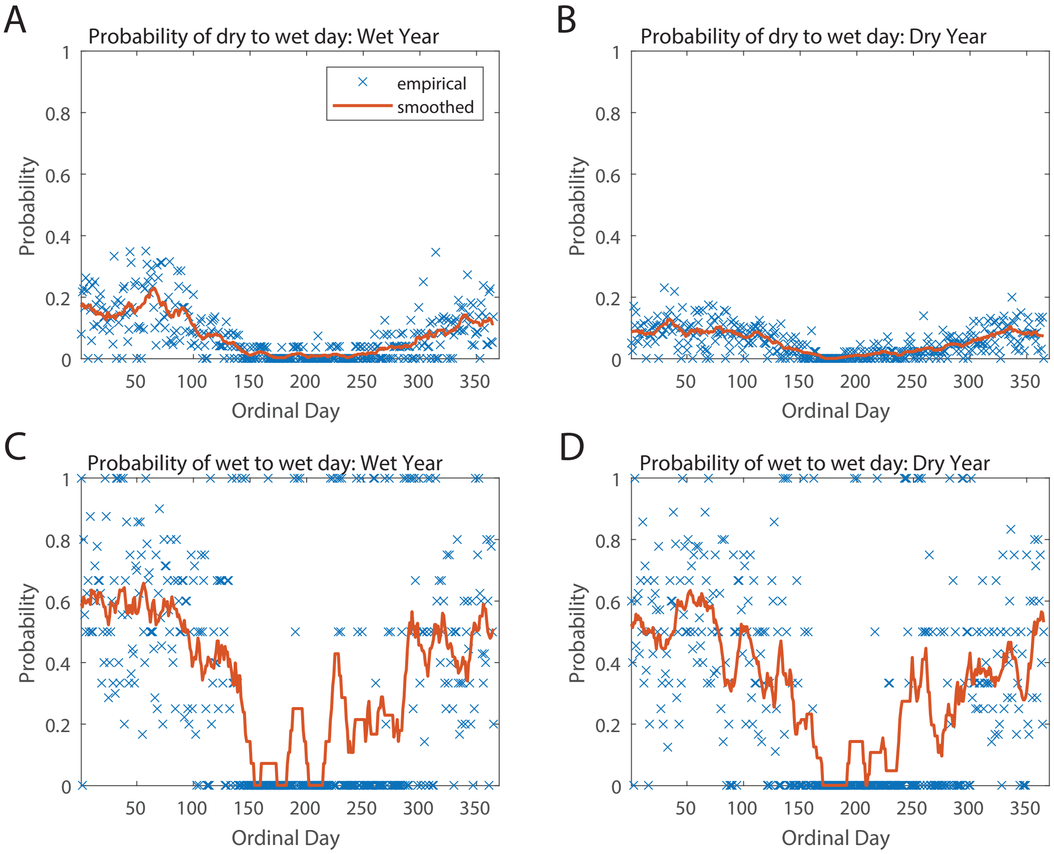

Figure A.1: Daily transition probabilities from (A) dry to wet within a wet year, (B) dry to wet within a dry year, (C) wet to wet within a wet year, and (D) wet to wet within a dry year. Empirical probabilities are represented by blue X's while the smoothed probabilities used in the MCMC rainfall simulator to determine daily precipitation occurrence are represented by orange lines. Smoothed probabilities were calculated as a 14-day moving mean of the empirical daily probabilities.

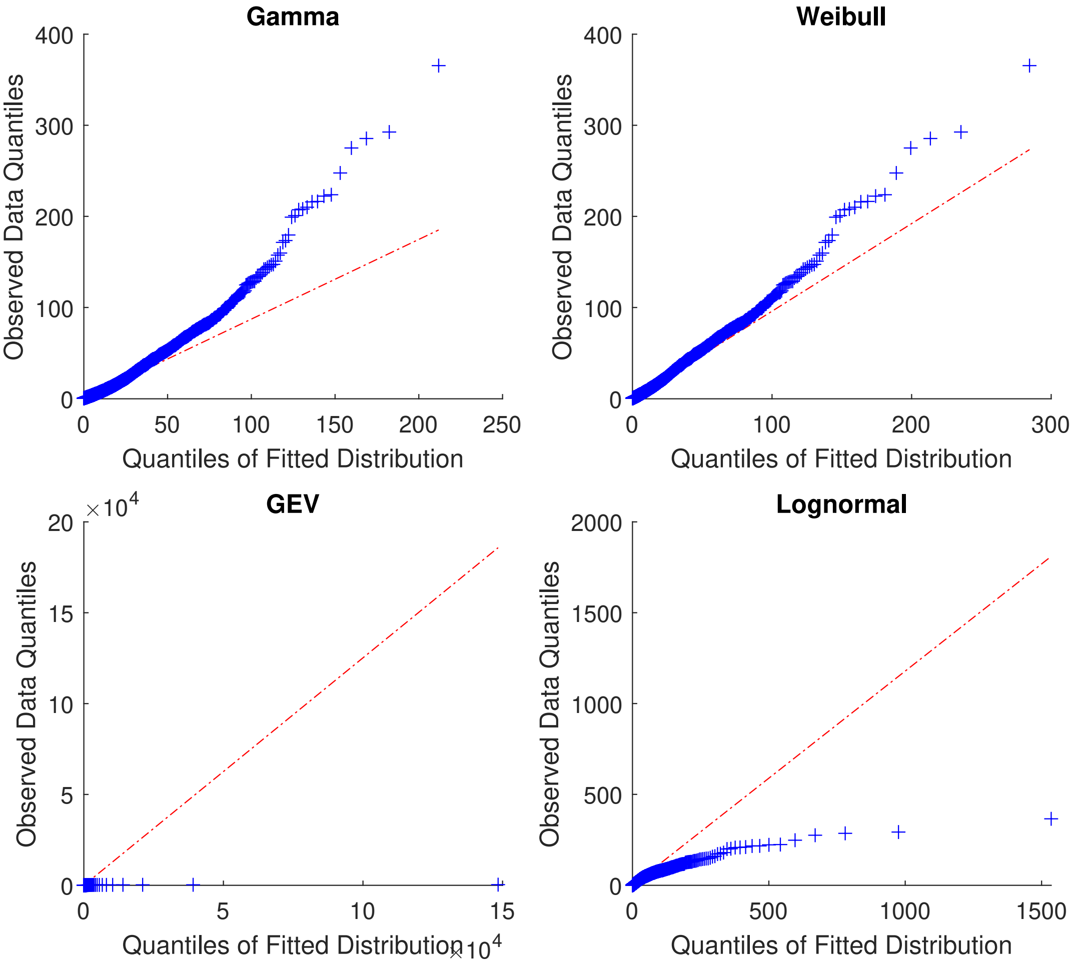

Figure A.2: Comparison of quantile-quantile plots for observed vs. fitted non-zero daily precipitation between four probability distributions commonly used in the literature for fitting to non-zero daily precipitation amounts. Observed values include all non-zero precipitation amounts on record.

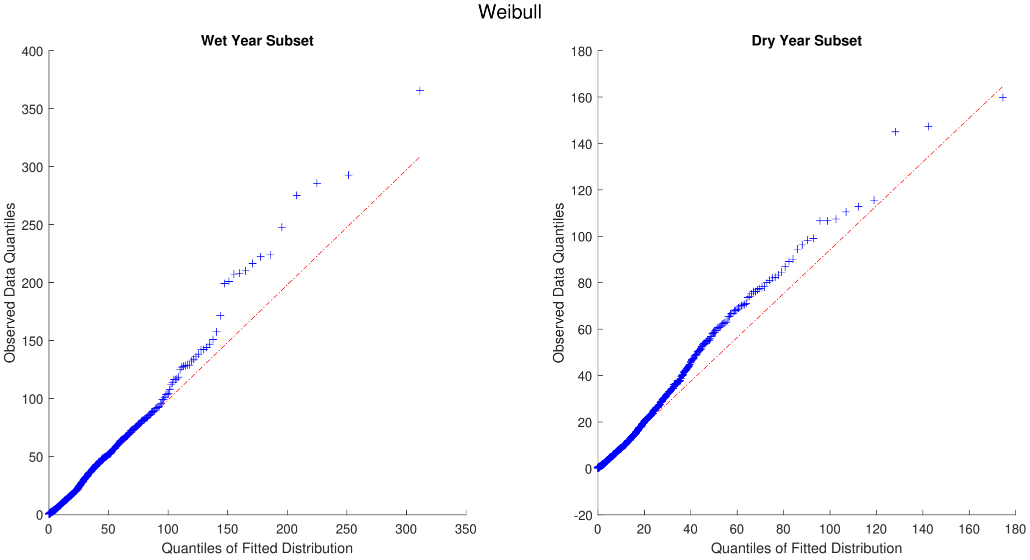

Figure A.3: Quantile-quantile plots of observed vs. fitted non-zero daily precipitation separated into wet-year and dry-year subsets. Fitted probability distribution is Weibull.

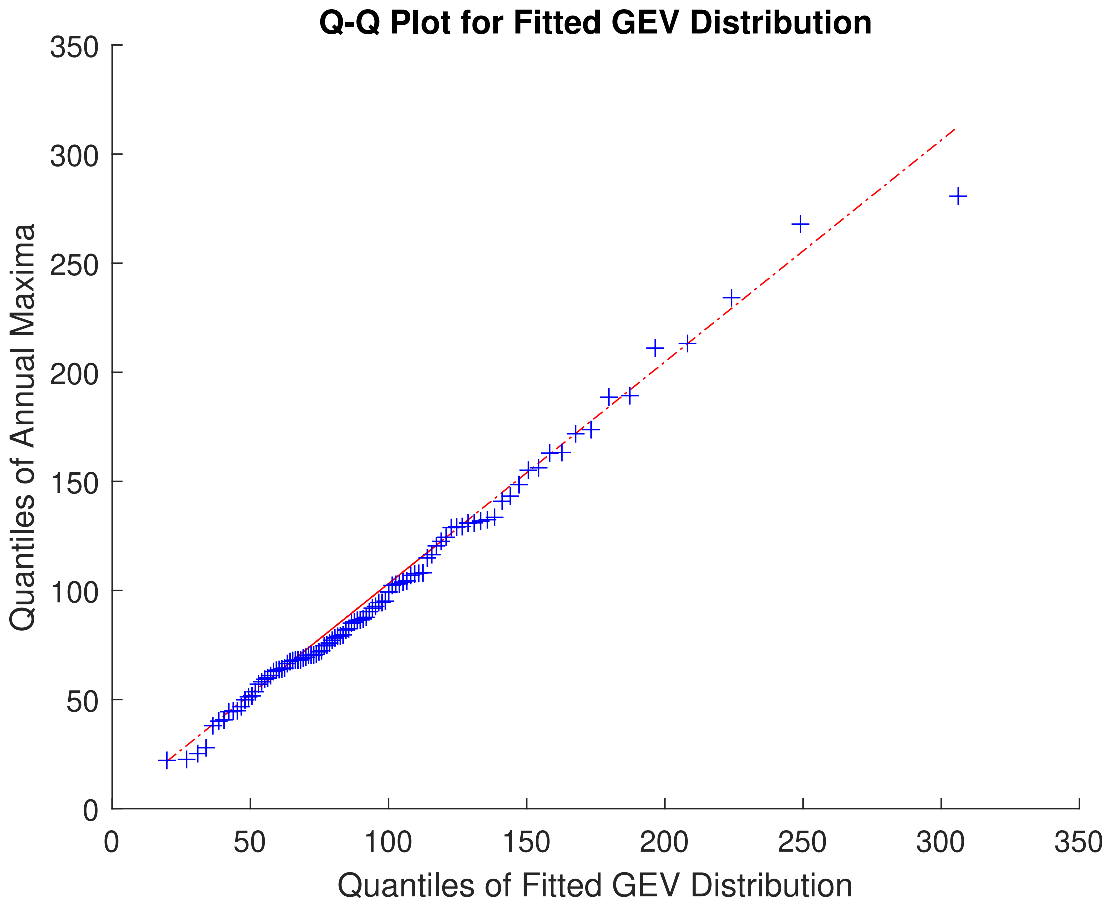

Figure A.4: Quantiles of annual maximum daily precipitation derived from a 100-year realization of the MCMC rainfall simulator vs. quantiles of the fitted General Extreme Value (GEV) distribution. The fitted GEV distribution was used to calculate the return levels that correspond to 50-year and 100-year return period storm events used in the model to determine the capacity of the flood channel and debris basin.

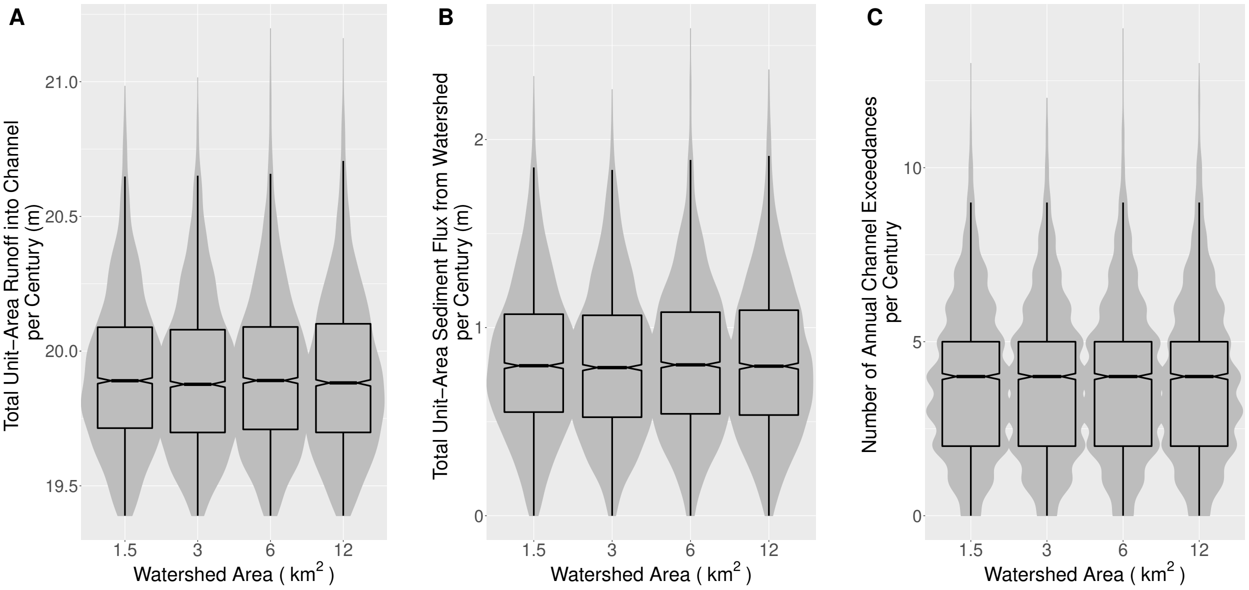

Figure A.5: (A) Total runoff entering flood channel per century normalized by watershed area, (B) total sediment flux from watershed per century normalized by watershed area, and (C) number of years per century with at least one channel overtopping event. The model scenario for this simulation used a 50B infrastructure design standard, S maintenance infrastructure approach, 20-year fire interval, and post-fire bulking factor range of $1.25 < k < 2.86$.

Appendix B

Supporting Information for Chapter 3

This supporting information contains figures that were used to define peak flow rates from observed stream gage records (Figure B.1), assess the fit of exponential curves to vegetation indices to estimate the recovery timescale parameter (Figure B.2), calibrate the curve number used in HEC-HMS modeling of post-fire hydrology (Figure B.3), and compare simulated fluxes of sediment to debris basin storage to ensure the mass/volume of sediment was conserved (Figure B.4). It also contains a table (Table B.1) that compares model error metrics between the calibration methods developed to calibrate PF2HazMo.

Table B.1: Error metrics for calibration of PF2HazMo by calibration method. MAE, NSE, RMSE, and % Error comprise the Gage Data Approach, while Frequency represents the Frequency Curve Approach.

Calibration Method	c_t (1/s)	MAE (cms)	NSE	RMSE (cms)	% Error
MAE	1.47×10^{-5}	4.88	0.568	6.20	190
NSE	1.24×10^{-5}	5.29	0.642	5.65	160
RMSE	1.24×10^{-5}	5.29	0.642	5.65	160
% Error	2.38×10^{-5}	7.94	-0.499	11.6	58.9
Frequency	3.36×10^{-5}	19.9	-4.83	22.8	519

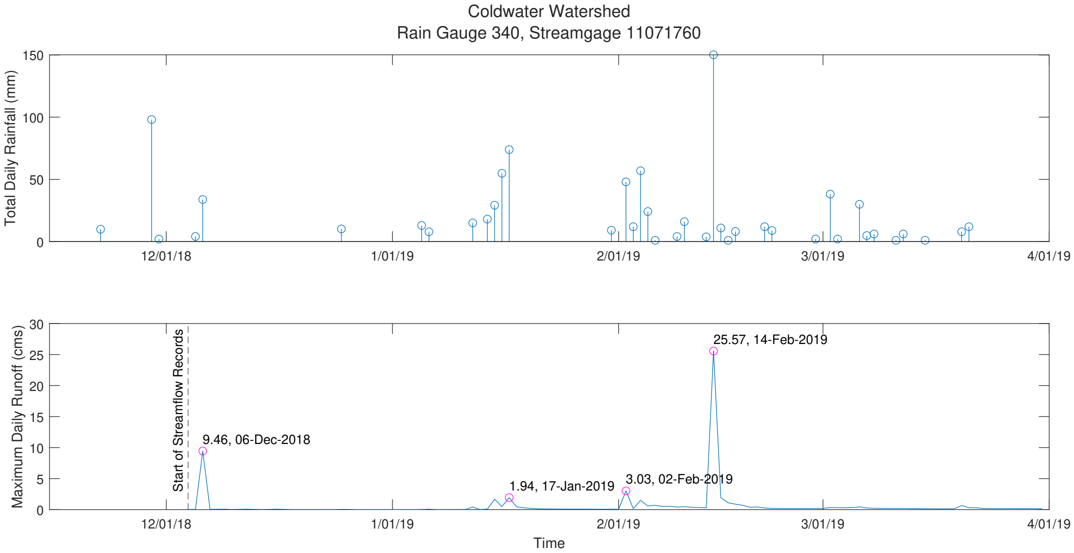

Figure B.1: Total daily precipitation and maximum daily flow rate time series (top panel), and observed peak flow rates (bottom panel) for Coldwater watershed. Fire occurred before start of time series on 6 August 2018.

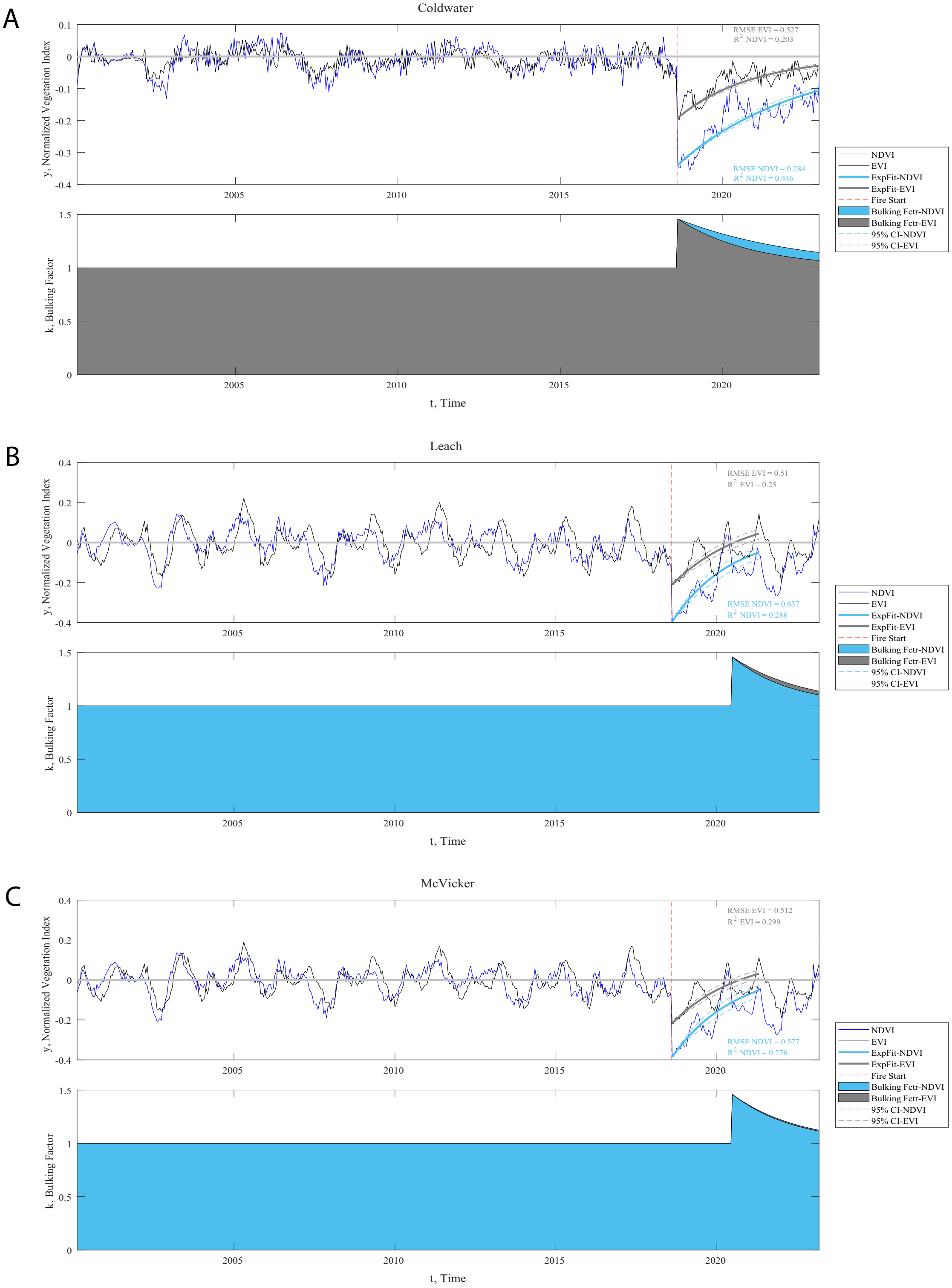

Figure B.2: Normalized NDVI and EVI time series and exponential curves fit to post-fire data (top panels) and bulking factor time series corresponding to recovery timescale estimates (bottom panels) for (A) Coldwater, (B) Leach, and (C) McVicker watersheds.

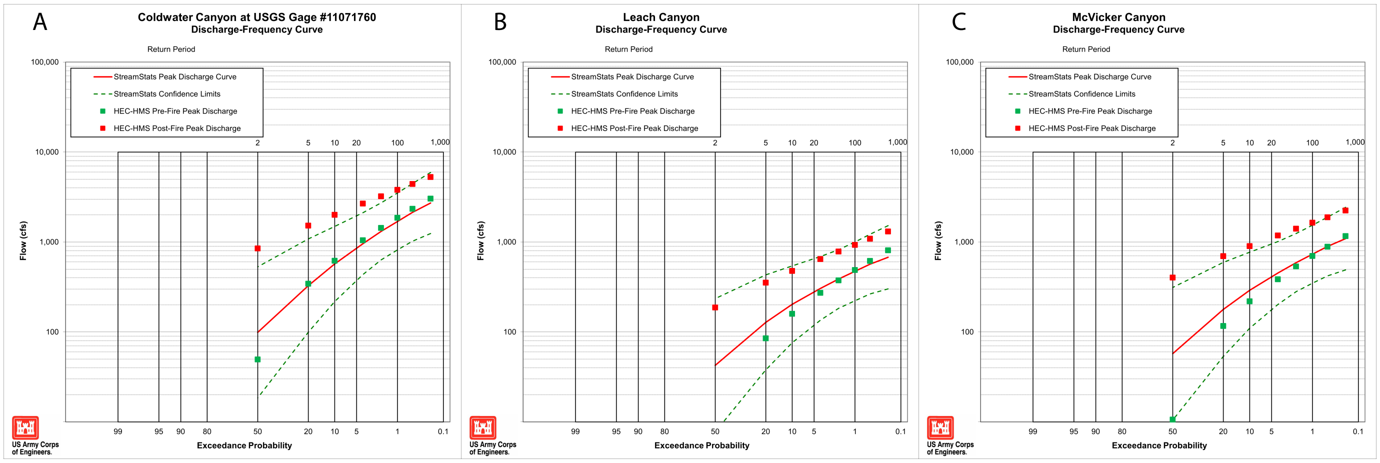

Figure B.3: Peak discharge-frequency curve from StreamStats (solid red line) with 90% confidence intervals (dotted green lines), estimated pre-fire discharge from HEC-HMS before adjusting curve number (green points), and estimated post-fire discharge (red points) from HEC-HMS for (A) Coldwater, (B) Leach, and (C) McVicker watersheds. Plot template modified from U.S. Army Corps of Engineers.

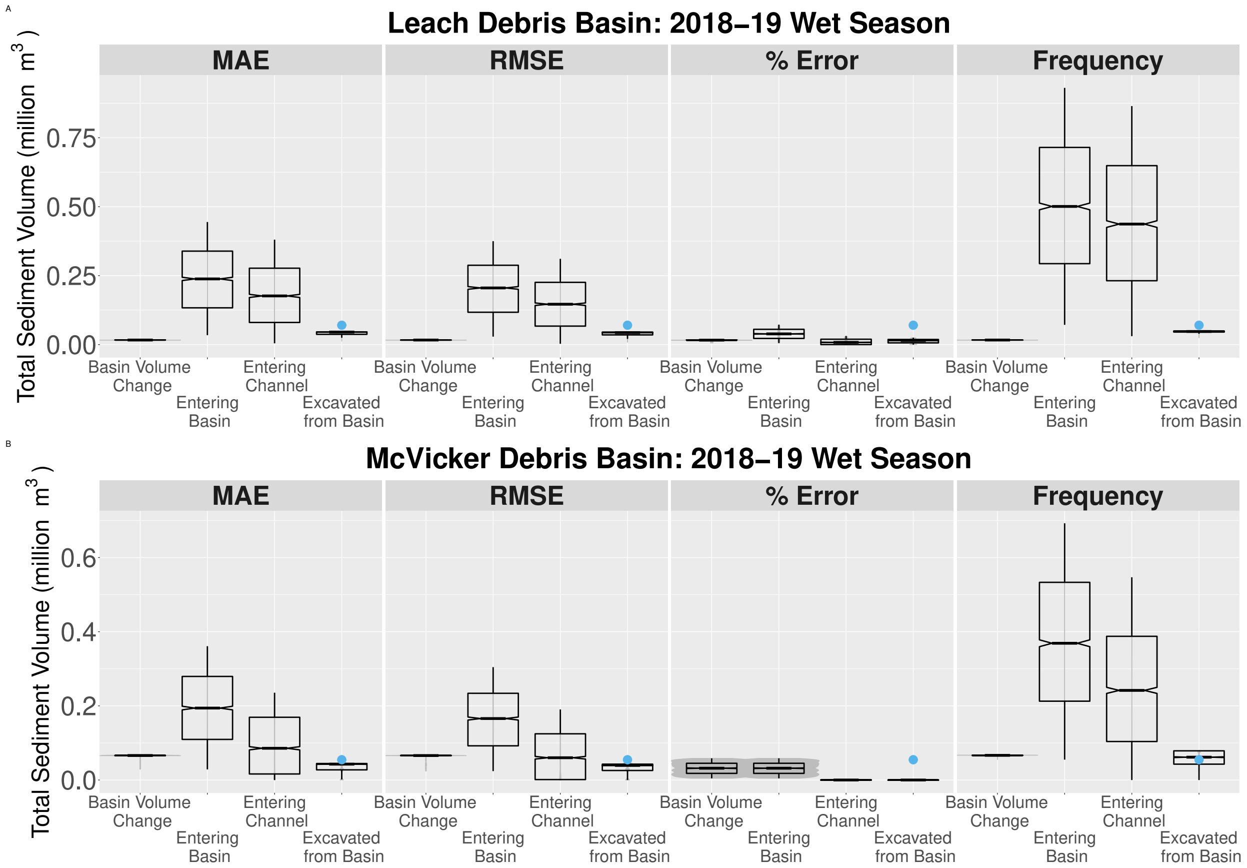

Figure B.4: Sediment volume change, influx, and outflux for (A) Leach debris basin and (B) McVicker debris basin for the 2018-19 wet season comparing simulation results across calibration methods. Blue points represent the total volume of sediment excavated by the end of the wet season for each debris basin recorded by Riverside County Flood Control and Water Conservation District.

Appendix C

Supporting Information for Chapter 5

This supporting information contains a figure of correlation results between model response variables and physical/socioeconomic variables from the regional application of PF2HazMo to 13 watersheds located in the Santa Ana Mountains (Figure C.1). It also contains a table that compares the values of physical and socioeconomic characteristics across sites (Table C.1).

Variable definitions for Table C.1:

- Area = drainage area
- c_t = runoff response parameter
- Slope = average watershed slope
- k_1 = post-fire bulking factor
- mFRI = mean fire return interval
- PrecipInt = 15-minute, 100-year precipitation intensity
- DBCap = debris basin capacity

- FCCap = flood channel capacity
- PopDens = population density
- MedInc = median household income
- NDI = average neighborhood disadvantage index
- $\mathrm{NDI}_{\mathrm{AW}}$ = area-weighted average neighborhood disadvantage index
- nBGs = number of block groups in downstream population
- DPA = total area of block groups that comprise downstream population

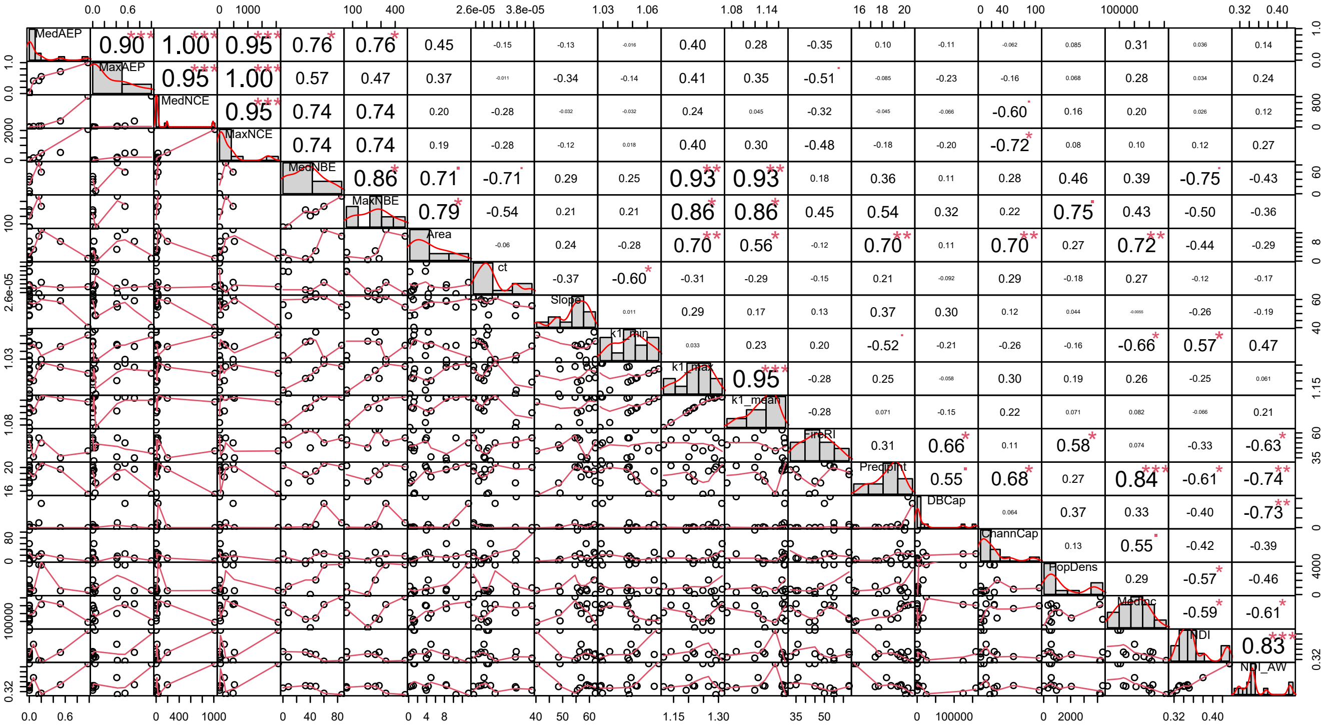

Figure C.1: Correlation matrix of all model output variables and physical/socioeconomic variables included in correlation analysis. Lower left diagonal shows scatterplots for each combination of variables by column and row. Upper right diagonal reports Spearman's rank correlation coefficients, with three asterisks (***) indicating significance at the 99.9% confidence level, two asterisks (**) at the 99% level, one asterisk (*) at the 95% level, and a dot (·) at the 90% level.

Table C.1: Comparison of site characteristics for Phase I study watersheds (n=13).

Site	Area (km^2)	$c_t\times 10^{-5}$	Slope (%)	k_1 mean	mFRI (yrs)	PrecipInt (mm/r)	DBCap (m^3)	FCCap (cms)	PopDens (/mi^2)	MedInc ($)	NDI	NDI$_{\text{AW}}$	nBGs	DPA (mi^2)
Brown	4.37	2.54	61.8	1.17	63	19.4	15,859	30	2,058	108,639	0.340	0.341	2	3.5
Dickey Canyon	1.33	2.91	49.0	1.17	45	15.7	-	6	427	101,348	0.435	0.433	2	11.5
Fresno Canyon	3.95	3.96	55.5	1.12	55	20	-	107	953	139,769	0.325	0.325	1	1.0
Greenwood Dr	1.16	2.87	40.3	1.15	42	15.5	-	0.5	577	97,962	0.435	0.433	3	11.7
Horsethief	0.26	3.56	48.5	1.07	48	17.4	2,003	0	1,169	122,175	0.329	0.340	3	6.4
Horsethief West	8.43	2.96	58.8	1.17	32	19.6	-	60	756	132,876	0.332	0.344	2	8.2
Hunt	1.04	2.73	59.9	1.13	63	18.8	4,161	0	4,389	105,366	0.349	0.344	2	1.3
Indian	8.36	2.82	59.1	1.17	35	19.7	-	10	540	144,750	0.348	0.348	1	7.3
Mabey	3.74	3.58	56.3	1.09	53	20.3	158,910	25	317	141,202	0.351	0.335	3	25.3
Main St	10.56	2.55	54.6	1.17	55	20.1	24,751	17	4,221	162,465	0.316	0.308	2	1.3
Oak St	13.37	3.07	62.2	1.17	50	20.7	124,334	25	4,169	143,045	0.313	0.313	1	0.6
Rice	4.98	2.80	56.9	1.13	36	18.4	-	10	559	120,193	0.380	0.377	2	11.1
Santiago	0.62	2.67	62.2	1.14	45	17.7	1,160	0	21	83,941	0.342	0.342	1	14.8